UNIVERSITY OF TURKU

Insights from a comparative analysis of *Rangifer tarandus* tibia and antler

Biomedical Imaging/Faculty of Medicine

Master's thesis

Hanna Saari

17.4.2026

Turku

Master's thesis

Subject: Biomedical Imaging

Author: Hanna Saari

Title: Insights from a comparative analysis of *Rangifer tarandus* tibia and antler

Supervisors:

1. Docent Miho Nakamura, Department of Clinical Medicine, University of Turku
2. Docent Pere Puigbò, Department of Biology, University of Turku

Number of pages: 140 pages

Date: 17.4.2026

Rangifer tarandus, commonly known as reindeer, inhabits circumpolar areas and is widely distributed in the Finnish Lapland. Because of its unique ability to regenerate antlers annually, this species offers an exceptional model for studying bone regeneration. The aim of this thesis was to characterize the material properties of temporary reindeer antler in comparison to permanent tibia across a cohort of reindeer individuals (n=9) to understand differences in bone growth dynamics and how they appear in material properties. X-Ray diffraction (XRD), attenuated total reflectance Fourier transform infrared (ATR-FTIR) spectroscopy, and micro-computed tomography (Micro-CT) were employed to evaluate crystallinity, composition, and microarchitecture between these two biologically and functionally distinct tissues. XRD and Micro-CT results showed that tibia samples had significantly greater crystallite size (ANOVA $p = 0.006$), higher bone mineral density ($p = <0.001$), and lower open and total porosity (ANOVA $p = < 0.001$) compared to antler. Porosity and trabecular-specific parameters showed variance across antler sample location (base, tip) and regions (central, intermediate, peripheral), the central part of the tip possessing the highest porosity, while the intermediate region of the antler base exhibited the greatest proportion of mineralized tissue (BV/TV) and trabecular thickness. ATR-FTIR results further demonstrated differences in chemical composition between the tissues. Mineral to matrix ratio was significantly higher (ANOVA $p = <0.001$) in tibia and lowest in antler tip, whereas amide parameters exhibited the opposite pattern. Both the carbonate-to-mineral ratio (ANOVA $p = <0.029$) and the carbonate content of bioapatite to phosphate (ANOVA $p = <0.001$) showed the highest carbonate content in antler tips. In contrast, carbonate accumulation exhibited a different pattern, with tibia having the highest presence of carbonate, and tip the lowest (ANOVA $p = <0.001$). These results highlight how differences in maturation time are reflected in the structures and compositional properties of bone.

Keywords: Bone regeneration, Reindeer antler, Bone material properties, X-ray diffraction, Fourier transform infrared spectroscopy, Micro-computed tomography.

List of Abbreviations

ABPC	Antler blastema progenitor cell
AP	Antlerogenic periosteum
ASBMR	American Society for Bone and Mineral Research
ATR-FTIR	Attenuated Total Reflectance Fourier Transform Infrared Spectroscopy
BMD	Bone mineral density
BMU	Basic multicellular unit
BSE	Backscattered scanning electron
BV/TV	Bone volume fraction
CaHA	Calcium hydroxylapatite
CI	Crystallinity index
CT	Computed tomography
Cu	Copper
DCB	Decellularized antler bone
ECM	Extracellular matrix
EDS	Energy dispersive spectroscopy
FWHM	Full width at half maximum
HAp	Hydroxyapatite (or hydroxylapatite by International Mineralogical Association)
HU	Hounsfield units
IRSF	Infrared Splitting Factor
M-CSF	Macrophage colony-stimulating factor

MMC	Mineral maturity/ crystallinity
NCP	Non-collagenous protein
PIGE	Particle-Induced Gamma Emission
PIXE	Particle-Induced X-ray Emission
Po(Cl)	Closed porosity
Po(Op)	Open porosity
Po(Tot)	Total porosity
pQCT	Peripheral quantity computed tomography
RANKL	Receptor activator of nuclear factor-κB ligand
ROI	Region of Interest
SEM	Scanning electron microscopy
Tb.N	Trabecular number
Tb.Sp	Trabecular separation
Tb.Th	Trabecular thickness
TCBC	Turku Clinical Biomaterials Centre
TMDU	Tokyo Medical and Dental University
VOI	Volume of Interest
XPM	Accelerated Property Mapping
XRD	X-ray Diffraction
XRF	X-Ray Fluorescence

Table of contents

1 Literature overview

1.1 Preface

The skeleton is a structure that enables body movement, protects organs, and regulates mineral metabolism in the body. Bone health, therefore, has a key impact on a person's overall well-being. Bone disease such as osteoporosis is a significant public health issue whose treatment requires a more profound understanding of bone structure and regeneration capacity. Bone health assessment is still initially based on the assessment of macroscopic mineral density, which, however, only contributes a fraction to the mechanical integrity of the bone (Nobakhti and Shefelbine, 2018). The structure and function of bone are based on a close interaction between organic and inorganic components, so it is essential to characterize these components in detail for a comprehensive understanding of bone. In particular, the inorganic mineral material consisting of hydroxyapatite requires more attention, as it plays a key role in bone strength and thus in diseases associated with fracture risk.

Unlike human studies, which have ethical and practical limitations, animal models allow the observation of disease development and processes, and regenerative mechanisms under controlled conditions (Kan, 2013). Ideally, an animal model used in bone research should closely reflect human skeletal development and regulation (McGee-Lawrence et al., 2013). Deer bone has been proposed to be a promising animal model for human bone research. A results from a comparative study focusing on the femurs of deer, pig, and sheep suggest that from these studied animal models, deer bone has the closest likeness to human bone in terms of density, ultimate strength in bending, and Young's modulus (Kieser et al., 2014). However, the research interest towards the *Cervidae* family has not only been due to their long bones but also to their headgear. For its fastest bone growth rate known among animals, antlers undergo an annual cycle of growth, mineralization, and shedding. From mammal organs, only antlers have the ability for complete regeneration, making them an excellent model for regenerative medicine (Li et al., 2025). In addition to the rapid growth rate, a structure supporting vascular access and biopsy extraction, an independent regulatory mechanisms of the antler pair, susceptibility to neuronal and hormonal manipulation,

freedom from flesh-based tension, and the possibility of monitoring the effects of maturation and aging processes for a long time, have been perceived as features in favour of using antlers as a model organism (Bubenik, 1990).

A notable amount of antler-related research has focused on *Cervus elaphus*, the red deer (Landete-Castillejos et al., 2019). Deer species share physiological similarities in antler development, which means that the findings from previous studies on red deer and other deer can serve as foundation for understanding reindeer antler biology. However, what sets reindeer apart from other deer is that both sexes grow antlers, which is rare among cervids. Additionally, reindeer have adapted to arctic and subarctic climates. The antler development, structure, and shedding have been noted to be influenced by a mix of hormonal and environmental factors. Because of these ecological and reproductive differences, more species-specific research is needed.

This thesis was carried out under the Phylobone research project, which aims to facilitate the exploration of bone regeneration and osteoporosis from an evolutionary perspective. This resource hosts an extensive dataset covering extracellular matrix (ECM) proteins associated with bone across human and animal systems (Figure 1). The integration of sequence data, phylogenetic relationships, and functional annotations offered by this platform strives to support in uncovering non-collagenous proteins partaking in bone development, repair, and disease progression.

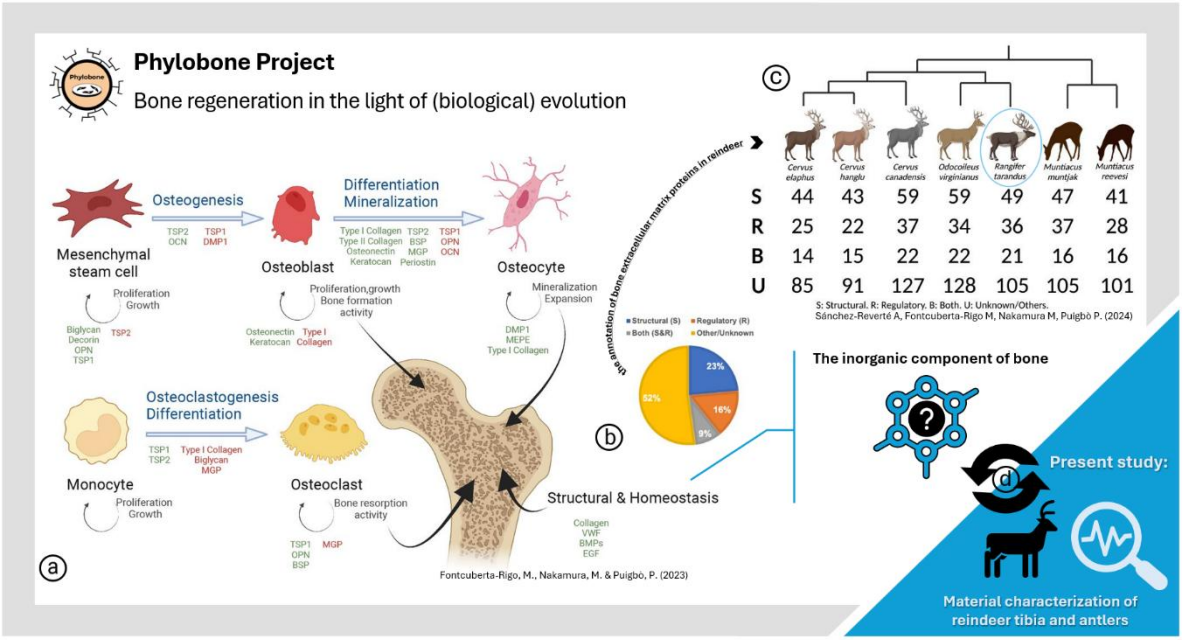

Figure 1. Current understanding of the extracellular matrix (ECM) protein-facilitated bone formation and remodelling. Section a of the figure shows the role and actions of osteocytes, osteoblasts, and osteoclast as part of the bone formation, mediated by ECM proteins (Fontcuberta-Rigo et al., 2023). Section b presents an estimation (pie chart) of the structural and regulatory roles of proteins in the bone ECM using the UniProt database (UniProt Consortium, 2021). Section c illustrates the putative bone extracellular matrix proteins identified in *Rangifer tarandus* (Sánchez-Reverté et al., 2024). The figure uses and adapts illustrations from the original publications with the authors' permission (The articles are licensed under a Creative Commons Attribution 4.0 International License). An illustration acting as a logo for inorganic material and a question mark together with the agenda of this present study have been added to the figure as a section d to represent the open questions about the role of inorganic material in ECM.

1.2 Bone: architecture, composition, growth and remodelling

The skeleton, a structure consisting of bone tissue in the body, is a supporting framework which role is to enable body movement and posture, protect organs, act as the body's mineral and fat reservoir, and maintain endocrine regulation and haematopoiesis (Prasanna et al., 2025; Raisz, 2005). There are two mechanisms involved in bone formation: more constrained intramembranous ossification concentrated in flat bones, clavicle, and scapula, and endochondral ossification responsible for the development of the greater part of the human skeleton i.e. axial and appendicular bone structures (López, 2024). In endochondral ossification, cartilage is replaced by mineralized cartilage. The differentiation of proliferating chondrocytes into a hypertrophic state triggers a chain of events in which cells invade and resorb the hypertrophic cartilage, while osteoprogenitor cells mature into osteoblast generating trabecular bone, and hematopoietic and endothelial cells form a primary ossification

centre, where secondary ossification centres form over time (Berendsen and Olsen, 2015). The resulting epiphyseal growth plate cartilage forming between the epiphysis and the metaphysis acts as a platform for longitudinal growth where the cycle involving of cell proliferation and hypertrophy, extracellular matrix synthesis and mineralization, vascular invasion, and apoptosis occur until the cartilage growth ceases in early adulthood (Haraguchi et al., 2019).

Bone is a complex, hierarchically organized tissue operating across multiple length scales (Tadano and Giri, 2011). In terms of macrostructure, there are two types of tissue in bone: a harder outer layer known as cortical (compact) bone, and inner, sponge-like layer, trabecular (cancellous) bone. Approximately 80% of the overall skeletal mass is compact and 20% trabecular, these tissues being distributed regionally with differing ratios to fulfil specific functional requirements (Clarke, 2008; Hart et al., 2020). Cortical bone consists of concentric lamellae formed by densely organised collagen fibrils and fibrils running in a perpendicular plane (Marks and Odgren, 2002). It is the superficial layer of bones serving as mechanical support and protection due to its mineralized structural rigidity and strategically aligned network of collagen fibres, which are able to resist mechanical loads more efficiently (Burr, 2002; Pearson and Lieberman, 2004). Porous, loosely organized trabecular bone, on the other hand, is responsible for metabolic functions (Marks and Odgren, 2002). It consists of a network of 50–400 μm-thick plates and rods and semilunar osteons (packets) contributing to its greater trabecular surface area and more active metabolism (Clarke, 2008).

At the mesostructured level (0.5–10 mm), bone marrow, fat, and bone cells act as filling material for the porous network of trabecular bone, whereas in cortical bone, this hierarchical level is expressed as resorption cavities and irregularly arranged osteons encapsulated in the lamellae layers, interstitial lamellae (Hamed et al., 2012; Tadano and Giri, 2011). The following level happens to be known as the interstitial lamella level corresponding to the microscale (10–500 μm); on this scale, the cylindrical secondary osteons with their incorporated diverging concentric lamellae surrounding the Haversian canals serve as the basic structural units of cortical bone together with highly mineralized cement lines and interstitial lamellae formed at the junctions of the osteons (Hamed et al., 2012; Obata et al., 2020; Tadano and Giri, 2011). At submicrostructure

level, the bone tissue is viewed from the perspective of a single lamella, formed from favourably organized collagen fibrils. Along these 3–7 μm thick, mineralized fibrillar matrices lie lacunae, ellipsoidal cavities containing osteocytes, while the spaces between the fibrils are occupied with sporadically positioned minerals (Fratzl and Weinkamer, 2007; Hamed et al., 2012).

On the nanoscale, bone consists of inorganic, organic, and aqueous phases; by weight, bone tissue is 60% inorganic, 30% organic, and 10% water, whereas by volume, this distribution is 40%, 35% and 25% (Feng, 2009; Mohamed, 2008). Collagen accounts for 90% of the total organic bone matrix, while the rest of the protein content consists of non-collagenous proteins (NCPs) (Mohamed, 2008; Palmer et al., 2008), which regulate cell signalling and attachment, mineral nucleation, and mineralization (Al-Qtaitat and Aldalaen, 2014). Over 90% of the collagen in bone tissues is type I, accompanied by a small amount of collagen type V (Amirrah et al., 2022). The inorganic matter, on the other hand, embodies primarily crystalline calcium phosphate, or hydroxyapatite [Ca10(PO4)6(OH)2], the other bone minerals being carbonate, fluorine, magnesium, potassium, and sodium (Hong et al., 2022; Mohamed, 2008).

Structural maintenance of mature bone occurs through continuous remodelling which involves bone-lining cells, osteoblasts, osteoclasts and osteocytes (Feng and McDonald, 2011). Osteoclasts, the multinucleated giant cells, resorb old bone and substitute it with bone newly formed by osteoblasts in a coordinated manner within a Basic Multicellular Unit (BMU) (Kenkre and Bassett, 2018). Osteoclastogenesis is regulated by receptor activator of nuclear factor-κB ligand (RANKL) and macrophage colony-stimulating factor (M-CSF), while matrix-derived growth factors released during resorption stimulate osteoblast differentiation (Salhotra et al., 2020; Xiao et al., 2016). The remodelling occurring in response to mechanical loading and microdamage is regulated by bone matrix-embedded osteocytes which have taken the role of mechanosensors (Šromová et al., 2023). Bone mass and microarchitecture are preserved in homeostatic state. With aging, hormonal changes, and some pathological conditions, the remodelling becomes imbalanced, leading to loss of net bone and rigidity (Feng and McDonald, 2011).

The bone extracellular matrix (ECM) serves as an important factor in bone regeneration by regulating cell growth, differentiation, and bone remodelling (Lin et al., 2020). The quality and integrity of bone depend on its structural organization and chemical composition. It has been established that mineralization and collagen orientation contribute to the anisotropic tissue hardness (Zysset, 2009). Due to the varying fibril organization at the tissue level, the characterization of mineral density is not sufficient on its own when assessing the elastic modulus of the bone (Nobakhti and Shefelbine, 2018). Therefore, the bone matrix quality and the mechanical properties of bone have been studied at different structural levels, from compact and trabecular tissue to individual lamella, in order to investigate the characteristics of fracture risk and fatigue damage in conditions such as osteoporosis (Kourkoumelis et al., 2019; Zysset, 2009).

The hierarchical organization of bone discussed above is a conserved feature in mammalian bones. However, certain skeletal structures have exceptional regenerative and adaptive properties. This brings us closer to the subject of this thesis - Cervids and their antlers.

1.3 Cervid antlers

Cranial appendages, commonly expressed as headgear, are a defining feature of most ruminants. Antlers, pronghorns, ossicones, and horns are different types of headgear with varying form, growth pattern, and histology, present in four existing ruminant families: *Cervidae*, *Antilocapridae*, *Giraffidae*, and *Bovidae* (Davis et al., 2011). These paired, symmetrical bone structures covered by skin and associated connective tissue are attached on the frontal bones of the skull or in the frontoparietal region (DeMIGUEL et al., 2014).

1.3.1 Structural and histological formation

Among ruminant cranial appendages, antlers are unique in their deciduous nature and annual regeneration cycle. Unlike other ruminants, the headgear of *Cervidae* consists of permanent proximal base, the pedicle, and a seasonally regenerated distal shaft, the antler (Landete-Castillejos et al., 2019). The very first pair of antlers grow as an extension to the pedicle; the regeneration cycle begins when the antlers have been shed

for the first time, mandated by dropping testosterone levels (Kierdorf et al., 2007). This primary developmental process of the pedicle and first antlers is controlled by a specialized tissue called antlerogenic periosteum (AP), whose removal prohibits antler growth, while its transplantation has been observed to instigate growth of ectopic antlers (Kierdorf and Kierdorf, 2000). Specific subregions of the antlerogenic periosteum have also been suggested to hold localized morphogenetic information defining antler branching. Based on their experimental deletion and grafting studies in sika deer, Gao and colleagues (2012) have proposed that the anterior subregion is at the heart of the orchestration of the first antler tine formation, whereas the medial subregion is essential in the development of all subsequent tines.

What distinguishes antler bone from the internal skeleton structurally is its primary, non-remodelled bone tissue with minimal secondary osteons; it has been established that antlers grow by apposition without the presence of growth plates and secondary ossification centres, the formation occurring through both endochondral and perichondral ossification pathways (Kierdorf et al., 2003; Landete-Castillejos et al., 2019). Formed from longitudinally tubular mineralized cartilage, antlers eventually develop into a mature cortical layer composed mainly of isolated primary osteons with longitudinally oriented collagen fibrils and co-aligned mineral particles (Krauss et al., 2011). Hard antlers consist of a regionally more mineralized outer cortical layer and a significantly more porous (>60%) central spongiosa (Landete-Castillejos et al., 2019). Cortical bone has further been divided into an outer cortex, main or central cortex, and a thin transitional zone between main cortex and spongiosa (Figure 2a) (Kierdorf et al., 2022; Landete-Castillejos et al., 2019). Proximo-distal variation along the antler axis has been demonstrated, where cortical thickness and mineral density have typically been higher at the antler base compared to the tip (Kierdorf et al., 2022; Landete-Castillejos et al., 2010). The growth centre at the antler tip exhibits longitudinally arranged differentiation zones, dermis, reserve mesenchyme, precartilage, transition zone, and cartilage (Figure 2b) (Li et al., 2002).

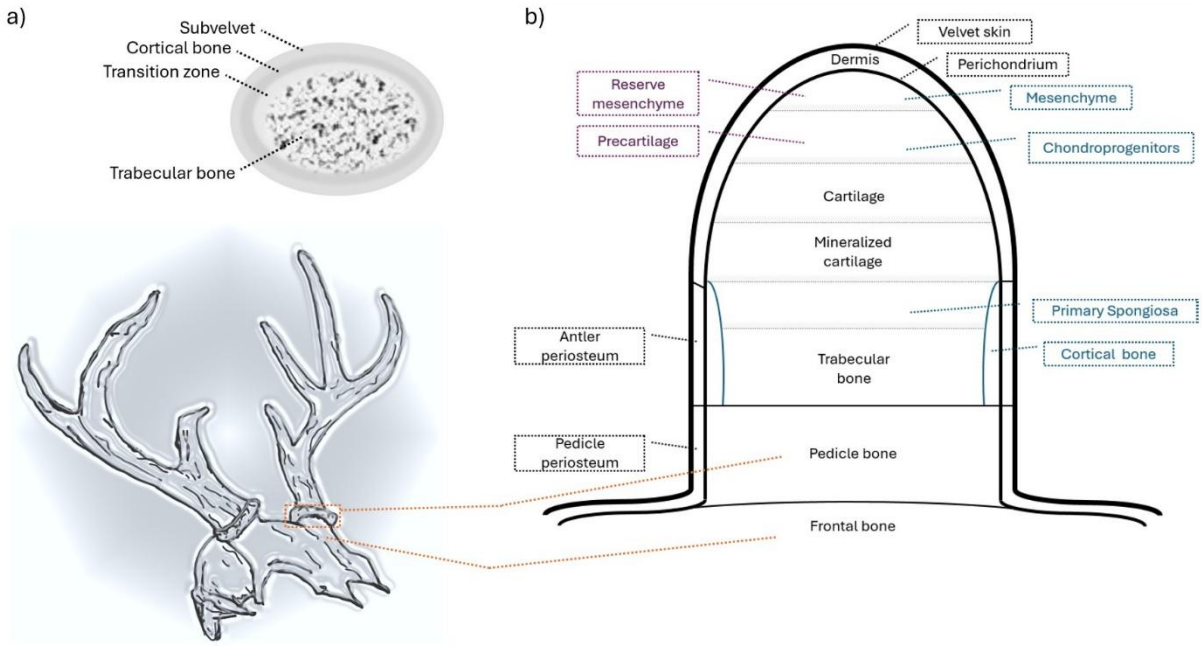

Figure 2. Structure of Cervidae antler. a) Illustration of histological zones adapted from the cross-sectional image by Picavet and Balligand (2016). b) The anatomical regions of a growing antler tip (longitudinal view). Purple and blue terms indicate varying naming systems used in publications regarding the tissue layers. The longitudinal antler illustration is based on publications by Price et al. (2005) and Kierdorf et al. (2007).

The evolutionary origins of ruminant cranial appendages have been and still is under debate. According to Landete-Castillejos and colleagues (2019), the concept of evolution has shifted from the idea of independent evolution of cranial appendages in different pecoran lineages towards a common neural crest origin. Based on their genetic studies, Wang and colleagues (2019) have proposed that all ruminant headgear derives from a single, neural crest stem cells-based evolutionary origin, where headgear development occurs through differentiation into cartilaginous and neural lineages. Likewise, study implementing pairwise alignments for putative ECM proteins reported a strong sequence conservation between R. *tarandus* and other deer (C. *cana densis* and O. *virginianus*), suggesting common evolutionary mechanisms which could be associated with the growth cycle of antlers (Sánchez-Reverté et al., 2024). It has been suggested that the antlers regenerate for defence purposes during the rutting season, as they become dead structures due to ischemia after the velvet is shed and can no longer be repaired.

Proto-oncogenes FOS, FAM83A, and REL have been reported to undergo positive selection in the cervid lineage together with tumour promoter HCE and antler-specific

growth factor and receptor genes FGF19, FGF21, FGFBP3, PDGFD, and PDGFRL which may imply a cancer cell-like growth process (Wang et al., 2019). In the same study context, Wang and colleagues noted that positively selected tumour suppressor genes such as PML and ADAMTS18 are highly expressed in the cervids' antlers, suggesting their involvement as regulators both in the rapid regeneration and cancer prevention.

Osteogenic differentiation and bone-forming capacities of the deer antler have been recently demonstrated. Decellularized antler bone (DCB) inspired bone graft material developed by Li and colleagues (2025) was found capable of reprogramming bone marrow stromal cells into antler blastema progenitor cells (ABPCs) carrying the rapid antler regenerative cycle and launching rapid bone formation in vitro and in vivo.

1.3.2 Mineral composition and its modulation by nutritional and environmental factors

The composition of antlers resembles other bones but with less mineral content which is also reflected in mineral density (Landete-Castillejos et al., 2010). Achieving a full secondary mineralization is a long process, which cannot be achieved in the rapid development cycle of antlers (Landete-Castillejos et al., 2019). Studies observing the content of minerals in deer antlers have recognised the existence of variation in mineral composition along the antler shaft, between proximal and distal tines, and across age classes, with major elements including calcium (Ca), phosphorus (P), magnesium (Mg), sodium (Na), and potassium (K), as well as trace elements such as zinc (Zn), copper (Cu), and manganese (Mn) being involved (Cappelli et al., 2015; Gambín et al., 2017; Gomez et al., 2016; Landete-Castillejos et al., 2012, 2007a, 2007c, 2007b; Nowicka et al., 2006; Tajchman et al., 2022).

The dietary intake and physical strain on the individual have been concluded to influence the mineral composition. Studies comparing farmed and free-ranging red deer have reported greater cortical thickness and a more balanced mineral contribution in individuals receiving a more nutritious diet, whereas Na, Mg, K, and Zn have been shown to be decreased with increased porosity and indications of physiological exhaustion in free-ranging population having more constrained nutrition intake (Estevez et al., 2009; Landete-Castillejos et al., 2012, 2007a, 2007b). Supplementation studies have uncovered aspects that further support these findings. Copper injections as a

supplementation strategy (Grace et al., 2003) have been demonstrated to have beneficial effect on serum Cu and cortical thickness in antler bone of adult stags (Gambín et al., 2017), while the additional manganese to the diet has improved impact energy and composition of minerals (Cappelli et al., 2015). While adult deer are seemingly responsive to micronutrient supplementation, the chemical composition of the first antlers is notably influenced by the lactation period early in life (Gómez et al., 2008; Landete-Castillejos et al., 2007c). However, research has found that the improvement of Ca and P intake in farmed fallow deer fawns has produced impacts on the mineral composition of their whole antlers as well, seemingly supporting antler development (Tajchman et al., 2020a).

The difference between age groups has been claimed to be visible in mineral patterns as well. Reportedly young fallow deer had greater Ca, P, Mg and Na levels in the proximal part of antler in comparison to older individuals, whose macroelements and antler mass were declined; additionally, higher trace element concentrations were noted in distal antler region together with increased lithium (Li) in the older specimen (Tajchman et al., 2022). Particle-induced analytical techniques such as x-ray (PIXE) and gamma-ray emission (PIGE) have been utilized to distinguish the effects of consolidation methods (Chadefaux et al., 2008) and to map differences in the mineralization of different antler beam locations, giving insights into the time-dependent biomineralization process (Gomez et al., 2016). Results from comparative studies across different deer species have indicated that the mineral profiles between the studied species are similar, whereas inter-specific differences occur in regards of the internal structure and mechanical properties (Ceacero et al., 2015; Pathak et al., 2001). Severe nutrient deficiencies, such as the low selenium levels found in Patagonian huemul, have been concluded to be associated with osteopathologies and worse chance of survival (Flueck and Smith-Flueck, 2008).

In addition to food intake and weather conditions, antlers as bioindicators are also sensitive to contaminants such as barium, fluoride, lead, and strontium (Jabłońska et al., 2016; Kierdorf and Kierdorf, 2005; Skuterud et al., 2005). Accumulation of toxic elements have been observed to vary between wild and farmed populations (Tajchman et al., 2020b) and being connected to the age of specimen and seasons of the year

(Tajchman et al., 2023). The accumulation of toxic elements has been reported to be notably high in the first antlers of young specimen even when calcium intake has been sufficient, which could suggest that during the rapid antler formation, both essential and non-essential elements are incorporated in the resorption of minerals (Steiner-Bogdaszewska et al., 2022). It has been suggested that heavy metal accumulations observed in deer antlers originate from soil ingested as part of the diet of *Cervidae* species (Buddhachat et al., 2016), as the antlers act as a storage for excess metal intake (Purdey, 2004).

1.3.3 Mechanical properties

Antler bone is viewed to be optimised for its part in combat due to its composition and microstructure. Bone stiffness, the load and energy required to fracture, and the energy absorbed during impact are measured with Young's modulus of elasticity E, bending strength BS, work of fracture W, and impact energy absorption U, respectively (Landete-Castillejos et al., 2019). The relative proportions of minerals and collagen, the hydration state and the microarchitecture are believed to be factors determining the stiffness, strength and toughness of antlers. Dry antlers have lower stiffness than wet antlers; the energy absorption on the other hand has been established to be significantly higher, which is beneficial when absorbing impact loads (Chen et al., 2009; J D Currey et al., 2009; John D. Currey et al., 2009). Mechanical properties have been found to vary along the antler beam and be related to antler mass and mineral content. The deterioration of mechanical properties towards distal regions of the antlers has been linked to reduced calcium concentration and mineralization due to unmet mineral requirements of demanding antler growth (Cappelli et al., 2017; Tajchman et al., 2025, 2022). The impact of both integral and trace elements on antler structure and performance has been studied through supplementation, which has been shown to alter mineral profiles and, in some cases, improve cortical thickness or mechanical performance in adult specimens (Gambín et al., 2017; Steiner-Bogdaszewska et al., 2022). When observing the structural level, anisotropic osteonal structure, heterogeneous collagen fibre orientation, cortical porosity, and complex mineralization patterns have been suggested as underlying factors for the toughness of antlers (Currey, 1988; Davison et al., 2006; Landete-Castillejos et al., 2012; Skedros et al., 2014).

1.4 Reindeer - a unique case among Cervids

Rangifer tarandus, commonly known as Reindeer, is a species of deer that inhabits circumpolar areas and is widely distributed in the Finnish Lapland (Lin et al., 2019). The antlers of this species stand out from the others because their growth rate is exceptionally fast among deer species and unlike any other species of *Cervidae* family, female reindeer also bear them (Bubenik et al., 1997).

The antler cycle of the reindeer is determined by sex and reproductive status (Figure 3). The annual cycle begins early in the spring after a long shedding period with the appearance of antler buds (Meschaks and Nordkvist, 1962; Nagy et al., 2021). The pre-rut period and rutting season in males, beginning in late summer, involves pronounced neck muscle development, velvet shedding, increased irritability, and reduced feeding activity, which culminates in confrontations demonstrating dominance (Espmark, 1964a). The male antler development, such as synchronization of velvet shedding and mineralization, has been considered to be driven by testosterone, although it has been noted as non-essential for the initiation of antler growth (Lincoln and Tyler, 1994). In addition to testosterone, fluctuations in LH and FSH are thought to be parallel to the antler cycle of stags (Bubenik et al., 1997). The older stags typically shed their antlers during winter's arrival (Espmark, 1964b). Castration has not been found to be detrimental to the antler formation and development in males, but it has been reported to shift the timing of the cycle stages (Lincoln and Tyler, 1994; Nasoori, 2020). Female reindeer (does) have a longer antler retention period. Infertile individuals and yearlings shed their antlers later in the winter, while pregnant does retain their antlers the longest, until early spring when the calving takes place (Espmark, 1964b). This maintenance of hard antlers throughout the fall and winter has been suggested to be due to an elevation in the sex steroids secretion in the ovaries (Lincoln and Tyler, 1994). In females, 17β-oestradiol has been suggested to contribute to the seasonal regulation of the oestrous cycle, although fluctuations in oestradiol, prolactin, and progesterone have not been found to clearly correspond to mineralization or antler casting (Bubenik et al., 1997). Lincoln and Tyler (1994) found that the removal of the ovaries led to premature casting of hard antlers together with skewed timing of red velvet shedding and antler regrowth, mirroring the observed effects of castration on males. Finally, tissue-level markers of

type I collagen formation and degradation from serum have been observed to increase in the circulation of females during antler growth, and these responses have been considered to have potential to predict subsequent growth rate (Vierimaa et al., 1999).

This antler retention alongside the presence and size of the antlers has been noted to be closely connected to the social hierarchy observed in the species during rutting time and winter. Body and antler size play a key role in maintaining stags' social status and mating groups (Nagy et al., 2021). After male-dominant rutting season and these stags shedding their antlers, the status of pregnant does gets elevated which is thought to be a survival strategy ensuring protection and sufficient nutrition for the mother and her offspring when the winter forage is limited (Espmark, 1964b).

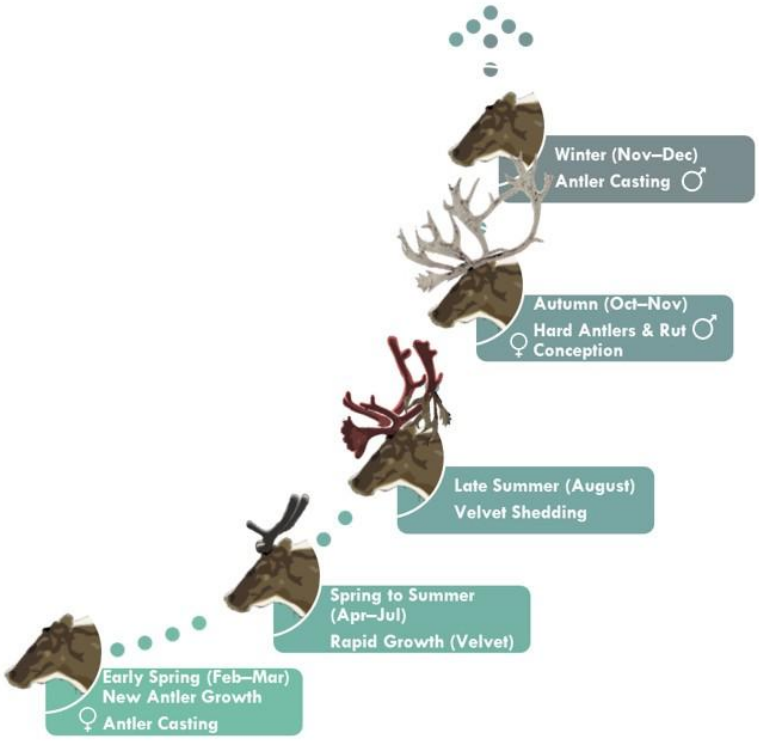

Figure 3. Growth process of reindeer antlers. A diagram of the growth and shedding cycle of reindeer antlers including the stages from antler growth and velvet formation to the shedding process. Males shed their antlers after rutting season whereas females carry them for a longer period of time, shedding them after calving in the early spring.

Studies investigating the effects of activity patterns, age, environment, human management, and sex on skeletal morphology of reindeer have made use of osteometric analyses, the primary focus being mostly on the postcranial skeleton. Bone robusticity, cross-sectional characteristics, and long bone dimensions have been demonstrated to reflect differences in mobility and load-bearing activities. Comparison

between wild, captive, and working reindeer composed by Niinimäki and colleagues (2021) reported that a more robust structure was observed under greater load-bearing conditions, while the cortical area and external dimensions were altered in individuals with reduced mobility. Similarly, a three-dimensional geometric examination has noted how forelimb morphology is more delicate in captive reindeer in comparison to free-ranging and working individuals, associating this phenomenon to altered mobility and feeding habits (Pelletier et al., 2020). Differentiation of skeletal activity patterns in different activity groups has also proven to be successful through entheseal (i.e. muscle and ligament attachment site) analysis acknowledging variations in studied individuals (Siali et al., 2024). In addition, entheseal variations have been suggested to provide information about supplementary feeding practices in the context of early Sámi reindeer herding (Salmi and Niinimäki, 2021). Findings like this make the reindeer skeleton appear adaptable and receptive to habitual and external influences. The impact of climate change on the environment has been documented to effect on reindeer herding systems and population management (Pekkarinen et al., 2023), illustrating how deeper knowledge of reindeer biology also contributes to the research field of ecology and sustainable management.

Osteometric studies have found differences in bone width and depth between groups with differing hormonal regulation. van den Berg and colleagues (2023) initially found differences in measurements of the ulna, humerus and femur of castrated males, intact males and females of domesticated reindeer from which they later extended the study to also include wild mountain and forest reindeer, demonstrating that in addition to sex and castration status, ecotype is also recognizable with osteometric approach (van den Berg and Wallen, 2025). Sex-specific growth trends are also reflected in the allocation of resources between body mass and antler development, as males have been observed to invest increasingly in antler growth as they age, while females have shown a levelling off in antler size earlier on (Melnycky et al., 2013). Conversely to postcranium, osteometric studies of reindeer antlers have primarily focused on the relationship between age, sexual dimorphism, and external morphology such as antler length, mass, volume, number of tines, and bilateral symmetry. Markusson and Folstad (1997) have suggested that symmetry in visually distinctive features of free-ranging male reindeer

antlers is subject to directional selection, the asymmetry embodying impaired developmental stability under environmental and parasitic stress. The diagnostic power of antler dimensions in distinguishing age and sex is, however, more questionable, as considerable overlap in antler size between studied groups has been previously reported by Høymork and Reimer (2002), although differing opinions have been expressed as well (Miller et al., 2013).

Similarly to previously discussed studies on other deer species, habitat quality and nutritional status have been noted to influence antler development in reindeer. In the comparison of isolated Svalbard reindeer (*Rangifer tarandus platyrhynchus*) populations under contrasting climatic and vegetational conditions, milder conditions and longer growing seasons were found to be associated with greater antler size and number of tines (Kavan and Anděrová, 2019). Earlier study on Svalbard reindeer females noted how between two regions, the other had a higher frequency of antlerless females (Jacobsen et al., 1998). Back then, Jacobsen and colleagues presented a hypothesis according to which the phenomenon could be caused by either differing range properties or genetic differences between subpopulations, possibly caused by a population bottleneck.

The adaptation of reindeer to their environment has quite recently been studied through gene expression. A comparative genomic analysis of reindeer (R. *tarandus*) by Lin and colleagues (2019) identified several genetic adaptations endorsing traits associated with Arctic survival and domestication. Reindeer were found to possess positively selected mutations in the vitamin D metabolism genes CYP27B1 and POR with extended androgen receptor binding abilities compared to other ruminants (Lin et al., 2019). Lin and colleagues believe that this enhances CCND1 gene expression when androgen levels are low, which in turn not only allows the growing antlers to receive sufficient calcium in conditions where solar exposure is limited, but potentially also enables the female antler development. Later research has reported the presence of the gene TRPV5 and TRPV6, which are also involved in vitamin D metabolism, while gene SILT2 was observed with relation to antler development (Weldenegodguad et al., 2020). The discovered mutations specific for reindeer in circadian-related genes such as PER2, NOCT, GRIA1, and ITPR3 have been suggested to explain the species' adaptation to the

light conditions of the Arctic region (Lin et al., 2019). PRDM1 and melanopsin gene OPN4B linked to retinal development have also been suggested to support survival in an environment undergoing light change at opposite poles (Weldenegodguad et al., 2020). Additionally, observed mutations in fat metabolism genes (APOB, FASN) have been interpreted to indicate that the fat-metabolism in warm-blooded animals living in polar regions has evolved, altering certain fat-related genes within each species for energy storage. Other discovered genes highlighted as relevant by Weldenegodguad and colleagues (2020) have been associated with immunity (CXCR1, CXCR2, CXCR4, IFNW1), pain tolerance against cold (SCN11A), as well as recombination promotion (PRDM9).

While osteometric and morphometric approaches have been taken rather extensively in reindeer research, the obtainable information is mostly limited to external characteristics of the antlers. Some studies have aimed to acknowledge the insufficiency of data on the internal structure by applying imaging-based methods. Micro-CT, X-Ray Fluorescence (XRF), scanning electron microscopy (SEM), energy dispersive spectroscopy (EDS), and nanoindentation together with Accelerated Property Mapping (XPM) have been previously utilized during a same study to assess whether sex or reproductive status (calving) influences the composition and mechanical characteristics of reindeer antlers. Using these methods, Board and colleagues (2024) identified calcium phosphate as the prevalent mineral phase in reindeer antlers, noting that calcium content was similar across the studied specimens whereas with phosphorus content, there was a 16% decrease in calving females. Other observations from their study suggested that the nanomechanical characteristics such as hardness and modulus remain the same despite sex- and reproduction-related variation in antler growth (Board et al., 2024). The antler stiffness (Young's modulus of elasticity) has also been reported to be similar between sexes (Shah et al., 2008). Micro-CT has been previously used to examine the internal alveolar structure of reindeer and red deer antlers, demonstrating that reindeer alveoli are composed of tighter mesh compared to red deer alveoli (Lefebvre et al., 2016). A Finnish study examined the activity patterns in reindeer long bones and metapodials by comparing cross-sectional samples from three modern groups (working reindeer, zoo dwellers, and wild reindeer) with a peripheral

quantity computed tomography (pQCT) scanner (Niinimäki et al., 2021). In addition to tomographic approaches, a small number of studies focusing on the characterization of reindeer headgear properties have utilized alternative imaging techniques, such as scanning acoustic microscopy, to examine the directional mechanical properties and orthotropic nature of antlers at the microscale (Sharma et al., 2025). Despite the valuable insights provided by these studies, the understanding of the interconnection between internal structure, mineral composition, and hierarchical organisation in reindeer antlers still seems to appear insufficient. Therefore, there remains a need for an analytical framework incorporating three-dimensional imaging with diffraction-based and spectroscopic methods.

1.5 Material characterization of bone

Studies incorporating FTIR microspectroscopy and imaging, XRD, and chemical analysis have provided identification of bone mineral content and composition across morphologically distinct sites in various species, with some of these findings being comparable to results obtained using mechanical, histomorphometric, densitometric, and micro-CT methods (Boskey, 2003).

1.5.1 X-Ray diffraction

Minerals, the crystalline inorganic solids produced by nature, can be distinguished by their physical features such as hardness, crystallinity, and density. The atom arrangement in crystalline structures is recurrent and regular, which is influenced by external conditions such as pressure and thermal profile (Ali et al., 2022). X-ray diffraction (XRD) is a common non-invasive method for the assessment of structural attributes, including characteristics such as crystalline phases, texture, orientation patterns, crystal dimensions, degree of crystallinity, and structural integrity (Tadano and Giri, 2011). The principle of the method is based on the interference of uniform X-rays reflected from the periodic crystal structure. Crystallites consist of high electron density planes, which have the ability to scatter a monochromatic beam of x-rays, generating diffraction maxima. This phenomenon can be used to determine precise spatial relationships between atoms, which is particularly evident in crystalline substances with periodic repetition (Tadano and Giri, 2011). The scattered waves reflected from

successive atomic planes have a reinforcing effect on each other (constructive interference) if they are in phase, and on the contrary, will nullify one another (destructive interference) if they are out of phase (González, 2012). Due to the regularity of the crystalline atomic structures (Figure 4), the interference of the scattered waves is constructive by nature, which can be interpreted in the resulting diffraction pattern (Ali et al., 2022). The condition for the event of reinforcing interference is that the difference in distance between the interfering rays must be a multiple of the wavelength λ (Pynn, 2009):

$$n\lambda = 2d \sin\theta$$

This is known as Bragg's law, where:

n is an integer

λ is the wavelength of incident X-ray

d is the spacing of crystal planes

θ is the angle of incidence

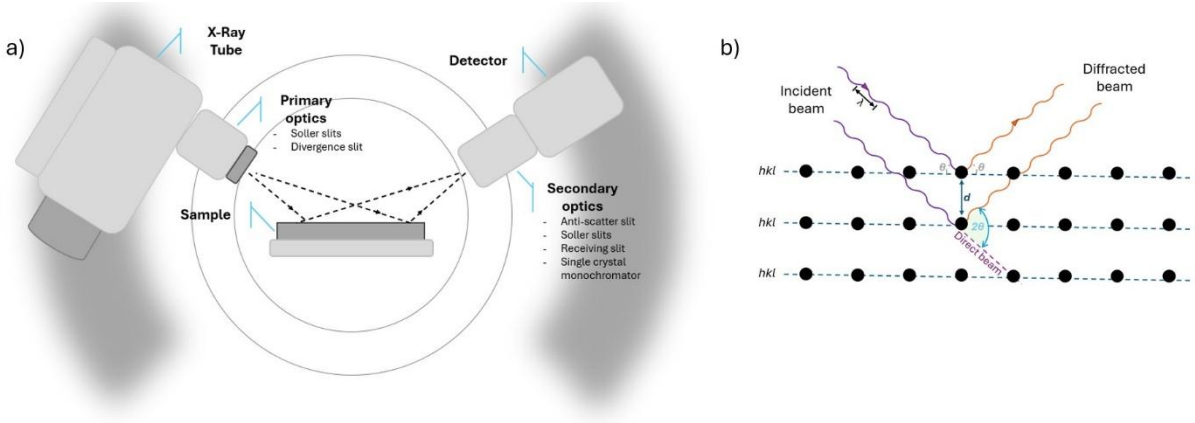

Figure 4. The working principle of the X-ray diffraction operation. a) X-ray beams are directed at the sample placed in the centre of the instrument, during which the radiation source and the detector move simultaneously along the diffractometer circle. b) Atoms with repetitive positioning form defined structures, planes, which disperse the radiation directed at them.

In bone research, properties studied using X-ray diffraction have included, among others, the mineral phase of bone tissue, the structure of collagens, in-situ strain, deformation, residual stress-strain, and the orientation of the mineral crystals (Tadano and Giri, 2011).

1.5.2 Fourier transform infrared spectroscopy

Fourier transform infrared spectroscopy (FTIR) is a vibrational spectroscopic method utilized to detect the characteristics and relative content of functional groups and chemical bonds from infrared radiation absorbance measurements (Figueiredo et al., 2012). FTIR generates an IR radiation beam from black-body source which passes into an interferometer splitting it in two (Mohamed et al., 2020). The divided beams get combined after being reflected from mirrors; from this recombination, a constructive and destructive interference, an interferogram, emerges (Fadlelmoula et al., 2022; Mohamed et al., 2017). The beam proceeds to a sample compartment where a distinctive energy frequency absorption occurs, leading to signal attenuation dependent on wavelength (Mohamed et al., 2017). The special interferogram signal is determined by the detector for all the frequencies concurrently, after which the superimposed beam is converted into an infrared absorption spectrum with the use of Fourier Transformation Function (Fadlelmoula et al., 2022).

Attenuated Total Reflectance (ATR) is one of the FT-IR sampling techniques that utilizes a high refractive index internal reflection element in the analysis, and which is particularly suitable for thick or strongly absorbing materials (Larkin, 2011). In ATR, an infrared spectrum is produced when total internal reflection occurs at the interface between a high-refractive-index crystal and the sample; when the majority of the infrared radiation is reflected, an evanescent wave penetrating a short distance beyond the crystal surface is formed (Figure 5), which gets attenuated by the absorption of the sample (Subramanian and Rodriguez-Saona, 2009). The occurrence of total internal reflection requires angles of incidence greater than the critical angle (Wang and Chu, 2013). Single- or multiple-reflection crystal configurations may be utilized depending on the intended use (Larkin, 2011).

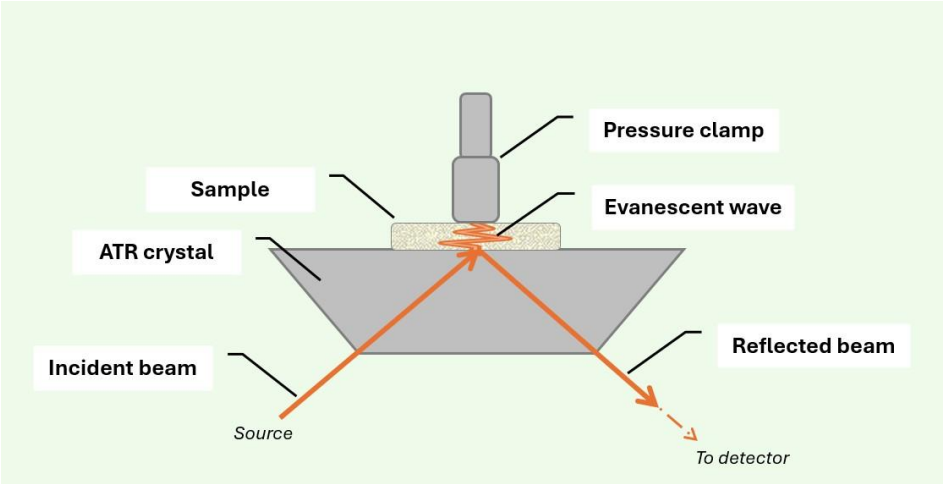

Figure 5. A schematic depiction of the Attenuated Total Reflection method. When measuring solid samples, the sample is pressed against a prism using a clamp. The interaction between infrared (IR) light and the sample occurs only at the point of reflection of the infrared light, resulting in an evanescent wave passing through the sample.

In FTIR, the identification of the chemical components is based on the correct interpretation of the IR absorption bands in the spectrum (Mohamed et al., 2017). The spectrums obtained from the FTIR spectrometer are presented either as absorption as wavelengths or in the form of transmittance (Nandiyanto et al., 2019). The infrared region is considered to consist of three subregions: far-IR-spectrum (<400 cm^{-1}), mid-IR-spectrum (400-4000 cm^{-1}), and near-IR-spectrum (4000-13000 cm^{-1}). The molecular absorbance of radiation in the mid-IR spectrum alters the vibrational energy state of various functional groups which is why this spectrum is commonly used in the sample analysis (Mohamed et al., 2017). The Mid-IR-spectrum comprises four distinguishable regions which are the single bond region (2500-4000 cm^{-1}), the triple bond region (2000-2500 cm^{-1}), the double bond region (1500-2000 cm^{-1}), and the fingerprint region (600-1500 cm^{-1}) (Nandiyanto et al., 2019). As the name suggests, the functional group region, or diagnostic region, contains peaks that provide information about the functional groups present in studied material.

Vibrational spectroscopic tools are well-suited for bone quality assessment as they offer both qualitative and quantitative insights into the main constituents of bone at spatial resolution (Paschalis et al., 2017). Raman and infrared spectroscopy have been utilized to study age and disease-related structural alterations on bone, the effects of mechanical stress on the molecular level, and secondary structures of protein (Morris and Finney, 2004; Yang et al., 2025).

1.5.3 Micro-computed tomography

Computed tomography, a three-dimensional diagnostic imaging modality is used to obtain information of health conditions as the technique provides image superimposition of internal structures and illustrates differences in tissue contrast (Mikla and Mikla, 2014). The image acquisition happens as an X-ray tube attached to a circular gantry of the CT scanner together with a detector on the diametrically opposite side rotates 360° around the patient, one rotation taking approximately 0.3 seconds (Nieminen, 2017). X-ray beams formed from emitted photons pass through the volume of the patient during the rotations, after which the beam interacts with width-defined detectors that register the radiation intensity while also enabling the evaluation of the attenuation coefficient of tissues (Goldman, 2007). Based on these gathered and stored measurements, cross-sectional images known as slices are reconstructed as a three-dimensional image of the patient's body (Reilly, 2019). In a CT image, the amount of tissue is determined by a three-dimensional unit called a voxel, which corresponds to a 2D pixel in a digital image. Image data obtained with CT imaging is presented in Hounsfield units (HU), which provide information about the linear attenuation of an X-ray beam in tissue compared to the attenuation in water (Reilly, 2019).

Micro-CT operates on the principles of conventional computed tomography but at a microscopic scale (Figure 6); this technique utilizes an X-ray source with microfocus, a CCD camera, and a step-by-step platform, which enable the reconstruction of high-resolution 3D images from generated 2D projections through back-projection (Boerckel et al., 2014; Chappard, 2022).

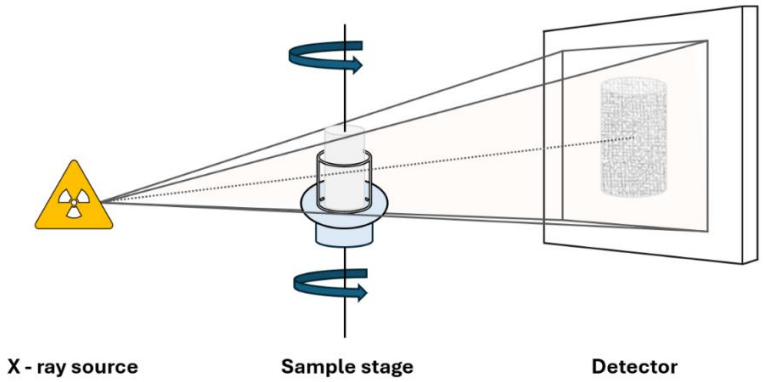

Figure 6. A schematic diagram of the micro-CT imaging principle. The sample is irradiated as it rotates on a platform between the X-ray tube and the detector. The detector captures the attenuated radiation passed through the sample, a measure which represents the density of the specimen. Projections corresponding to each degree position are reconstructed using a computer cluster.

Bones as a research topic extend beyond fields such as regenerative medicine tissue engineering. XRD, FTIR, and micro-CT techniques have also been employed in archaeological contexts to investigate bone preservation, and the effects of various treatments such as consolidation and cremation (Chadefaux et al., 2008; Dal Sasso et al., 2018).

2 Aims and hypotheses

This thesis treats reindeer antler as a natural model for rapid bone formation, with the aim of characterizing its composition, mineralization, and structure using X-ray diffraction (XRD), attenuated total reflectance - Fourier transform infrared spectroscopy (ATR-FTIR), and a micro-computed tomography (micro-CT) system. Tibias of the studied individuals were included as a reference for load-bearing bone, presenting an opportunity to compare the structural and mineral properties of these functionally different bones. Through this comparison between annually regenerating tissue and permanent bone, this work seeks to gain a deeper understanding of how growth rate, remodelling, and regeneration processes are reflected in the properties of bone material, and to examine whether the identifiable bone material properties can be extrapolated to factors affecting bone quality and fragility in human skeletal health and disorders such as osteoporosis.

3 Materials and methods

3.1 Sample preparation

Reindeer samples were obtained from local reindeer farmers and processed at Kevo Subarctic Research Institute, Biodiversity Unit, Faculty of Science, University of Turku (69°45'N, 27°01'E). Antler and tibia samples were collected from twenty reindeers immediately after slaughter. The samples were stored in sterile plastic tubes or bags and immediately transferred to Turku for experimentation. No animals were killed for the sake of this study; therefore, no approval of the ethics committee or additional permits were required regarding this research phase.

The bone samples were stored in sterile plastic tubes or bags and frozen at −20 °C until use. Nine individuals were chosen for the preliminary study. Bone samples of antler tip, antler base, and tibia were cut with a diamond saw (Buehler, IL) into slices 1–2 mm in thickness for material characterisation (Figure 7). The sliced samples were cleaned by ultrasonication in distilled water. The samples were defrosted and cleaned in deionized water for 3 hours at room temperature. The water was exchanged three times, once every hour. After the cleaning step, the samples were allowed to dry thoroughly at room temperature in a fume cupboard.

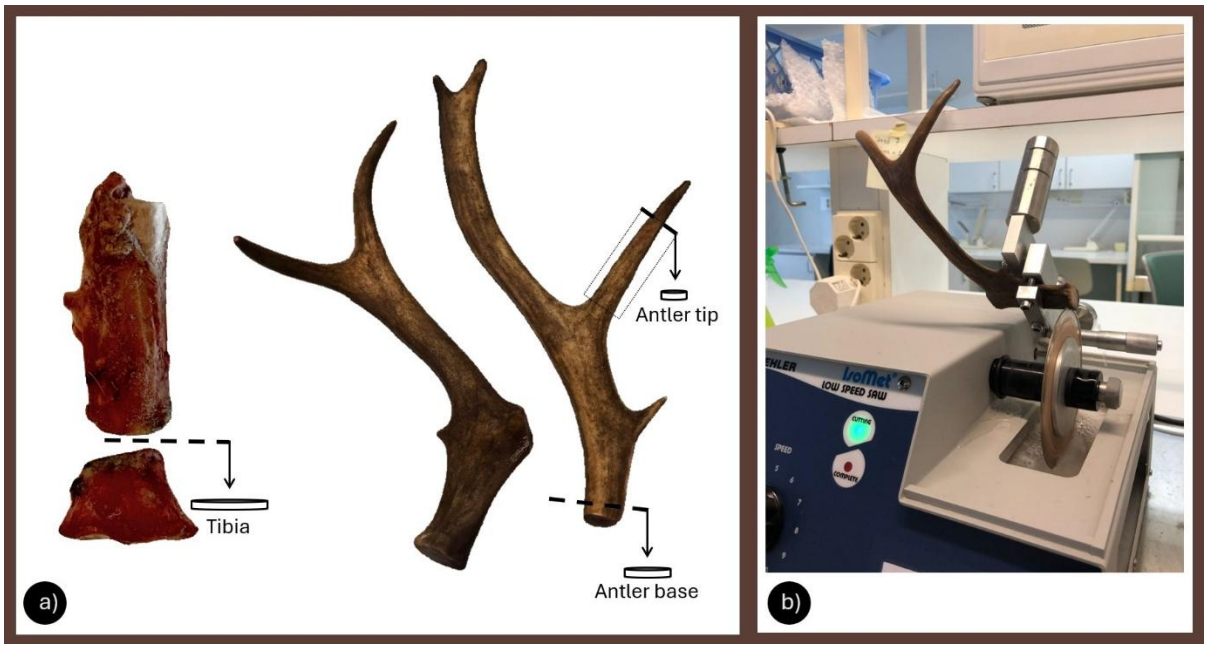

Figure 7. Preparation of bone slices. a) Slices of 1–2 mms were obtained from tibias, and tips and bases of antlers. Antlers were cut into smaller parts (dotted box area) so that they could fit and be processed evenly with the saw. The transverse sample sections of the antler were cut parallel to the vertical axis (dotted lines) while ensuring that the sample surfaces were flat. b) Obtainment of antler slices with a low-speed saw.

3.2 Benchmarking

This master thesis is based on three methods of material characterization: XRD, FTIR, and Micro-CT. These methods are well established for human and model organisms (Alebrahim et al., 2023; Fadlelmoula et al., 2022; Lindtner et al., 2025; Mata-Miranda et al., 2019; Paschalis et al., 2011; Prasanna et al., 2025; Shim et al., 2022; Tadano and Giri, 2011). However, since reindeer is not a model organism, a benchmark testing was applied to one reindeer individual in the internship prior to this thesis. Briefly, this benchmark study examined whether the measurement methods were compatible with the reindeer bone material and if possible, differences between antler and tibia were detectable. Measurement conditions for each method were as will be described later in this work for each analysis method. Data handling for XRD and FTIR was performed with Origin software. Process steps for XRD data included smoothing (Signal processing) and baseline correction (Peak Analyzer) of the raw data and assessing the peak location and full width half maximum (FWHM) with Peak Analyzer and Quick Fit tools. The results of this testing indicated that the produced XRD measurements had peak appearance comparable with the published hydroxyapatite standard. Crystallite size calculated with

the Full Width at Half Maximum (FWHM) values and the Scherrer formula were noted to be largest in tibia and smallest in antler base. Crystallinity, mineral to matrix ratio, and mineral maturity values were derived from FTIR data, from which the mineral to matrix ratio yielded a notable difference between the bones with tibia having the highest mineral content and antler tip the lowest. Variation of the bone mineral density and closed porosity (2D) between tibia and antler were also detectable in micro-CT results, indicating a denser tibial structure.

3.3 X-Ray diffraction (XRD) analysis

The determination of crystallinity and lattice parameters were done with the PANalytical EMPYREAN series 2 instrument (Figure 8) as a collaboration with Prof. Petriina Paturi (Wihuri Physical Laboratory, Department of Physics and Astronomy, University of Turku). The instrument in question uses a Cu x-ray tube which emits Cu Kα radiation with the wavelengths of λKα1 = 1.5406 Å and λKα2 = 1.5444 Å. The scanning was performed at 45kV and 40mA in the 2θ range of 20° to 90°, with a step size of 0.020 degree on a diffraction spectrometer, Bragg-Brentano HD monochromator, and a PIXcel 3D detector, with temperature control provided by the Anton Paar TCU 110 Temperature Control Unit.

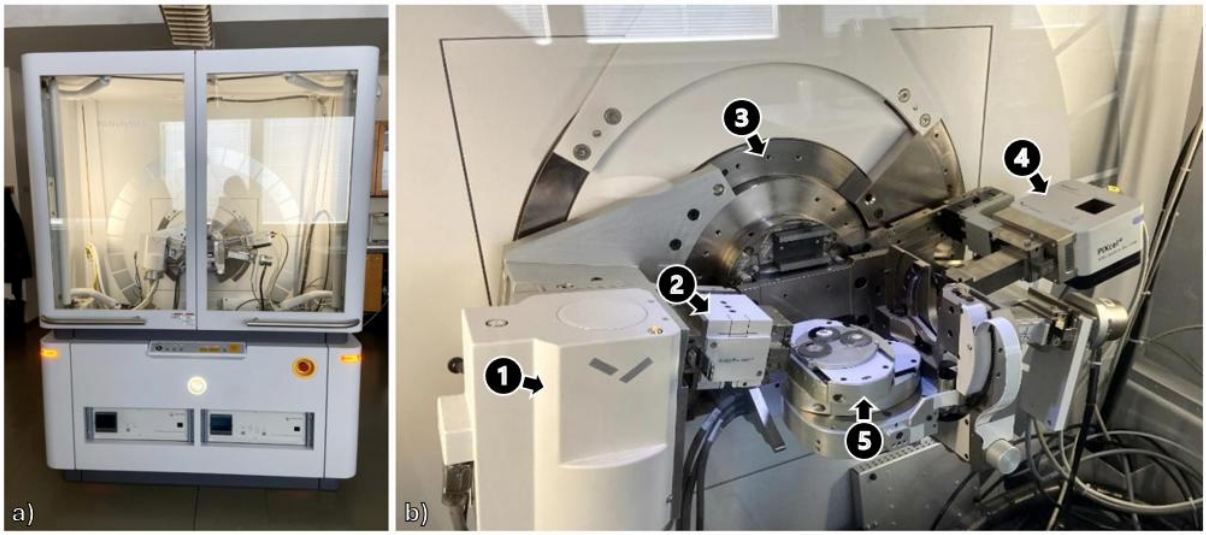

Figure 8. PANalytical EMPYREAN series 2 diffractometer. a) The lead glass windows in the front doors possess X-ray absorption corresponding to 1 mm of lead. b) The steel enclosure of the diffractometer with its components: 1. Tube housing with X-ray tube, 2. Incident beam optical module, 3. Goniometer, 4. Detector, 5. Sample stage.

For data analysis, the PANalytical DataViewer software was utilized with manual coordinate settings and an angular range from 20-90°. The measurement conditions are listed in Table 1. The resulting bands were analysed in relation to the material data set recognised by the International Centre for Diffraction Data (ICDD) database.

Table 1. Measurement conditions of XRD analysis.

Instrument Parameter	Acquisition Setting
Anode material	Cu
K-Alpha1 wavelength	1.5405980
K-Alpha2 wavelength	1.5444260
Ratio K-Alpha2/K-Alpha1	0.500
Divergence slit	Fixed, 0.38 mm
Monochromator used	NO
Generator voltage	45 kV
Tube current	40 mA
Scan mode	Step
Scan axis	2Theta-Omega
Scan range	20.0 - 90.0 deg.
Scan step size	0.0065651
Time per step	18.870 s

3.4 Fourier-transform infrared spectroscopy (FTIR) analysis

The bone slices were subjected to attenuated total reflectance Fourier transform infrared spectroscopy (ATR-FTIR) with a PerkinElmer Frontier IR (Figure 9) with an attached ATR unit located at the Turku Clinical Biomaterials Centre (TCBC). Some of the properties of this analyser have been mentioned in Table 2. Initially the intention was to obtain the IR spectrum from the whole MID-infrared region (4000–400 cm^{-1}), however, due to a poor response of the bands at the lowest wavenumber in the fingerprint region, the region of interest was narrowed down to 4000-800 cm^{-1}. The baseline correction function of PerkinElmer Spectrum software was applied for each spectrum.

Table 2. Measurement conditions of ATR-FTIR analysis.

Instrument Parameter	Acquisition Setting
Scan range	4000 - 800 cm^{-1} (Frontier IR)
	4000 - 400 cm^{-1} (Spectrum 100)

Instrument Parameter	Acquisition Setting
Resolution	4 cm^{-1}
Data interval	1 cm^{-1}
Accumulation	10 scans

The data analysis of FTIR spectra was done by examining all the peak numbers and values from the original data and comparing them to quantified frequencies (wavenumbers) and their assignments from publications that have compiled correlation tables from research literature. The observed peak positions with the functional groups characteristic for bone are presented in the Results section.

In order to include the initially planned region between 800-400 cm^{-1} for these analyses, more measurements were taken with the PerkinElmer Spectrum 100 instrument at the Institute of Biomaterials and Bioengineering Tokyo Medical and Dental University (TMDU).

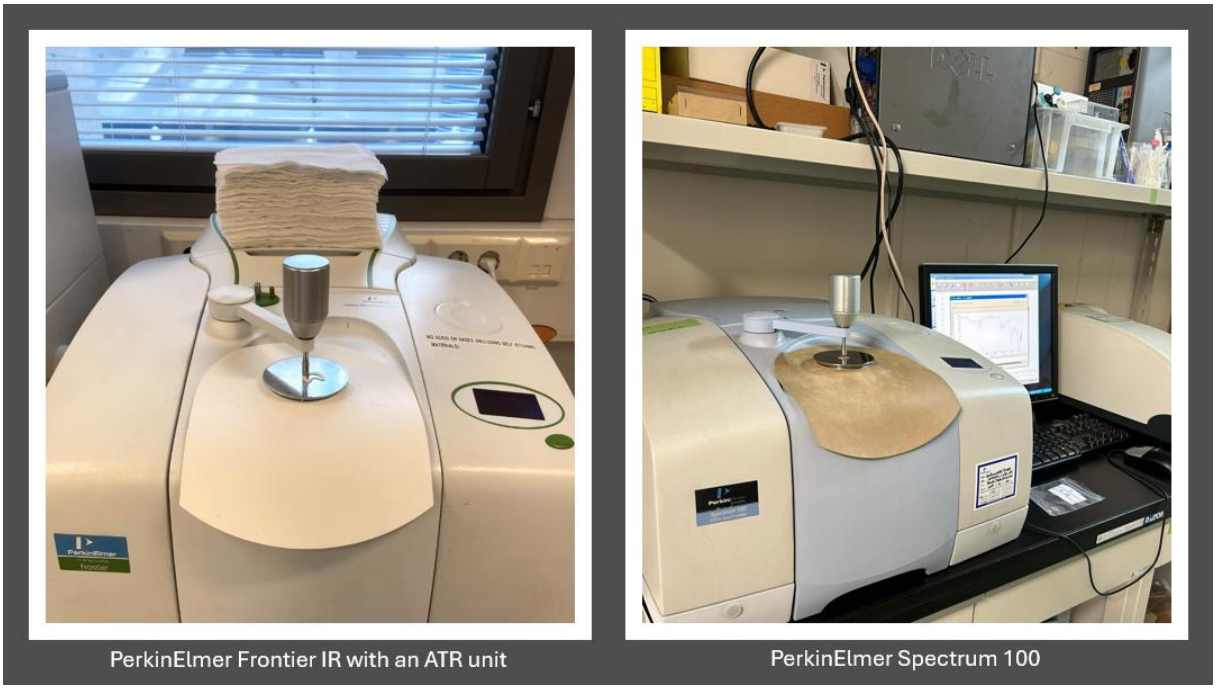

Figure 9. PerkinElmer Frontier IR (Turku Clinical Biomaterials Centre) and PerkinElmer Spectrum 100 instrument (Institute of Biomaterials and Bioengineering Tokyo Medical and Dental University).

3.5 Micro-computed tomography (micro-CT) analysis

Micro CT imaging was conducted with SkyScan1272 BRUKER (Figure 10) at the Medisiina Imaging Centre service unit of the Department of Biomedicine, University of

Turku. The SkyScan1272 control software was used to switch the system and X-Ray source on, to insert the selected samples and to obtain an on-screen projection image. Samples were scanned one sample at a time with an X-ray tube voltage of 70 kV and a current of 142 uA. Before each scan, the image format was set to 2452 x 1640 pixels, while the elevation (in millimetres) was customized for each sample due to the variety in sample size. Averaging remained unadjusted. Scanning parameters were adjusted with the “Scanning Options” dialog, where it was decided that the rotation step (degree) will be 0.5 and the pixel size 7.5 um for each sample. With these parameters, the scanning process took approximately 22 minutes per sample. To mitigate beam hardening, a 0.5 mm thick aluminium filter was incorporated during the scan. Furthermore, the scanning was carried out over a full 360-degree rotation to achieve a subsequent reconstruction process.

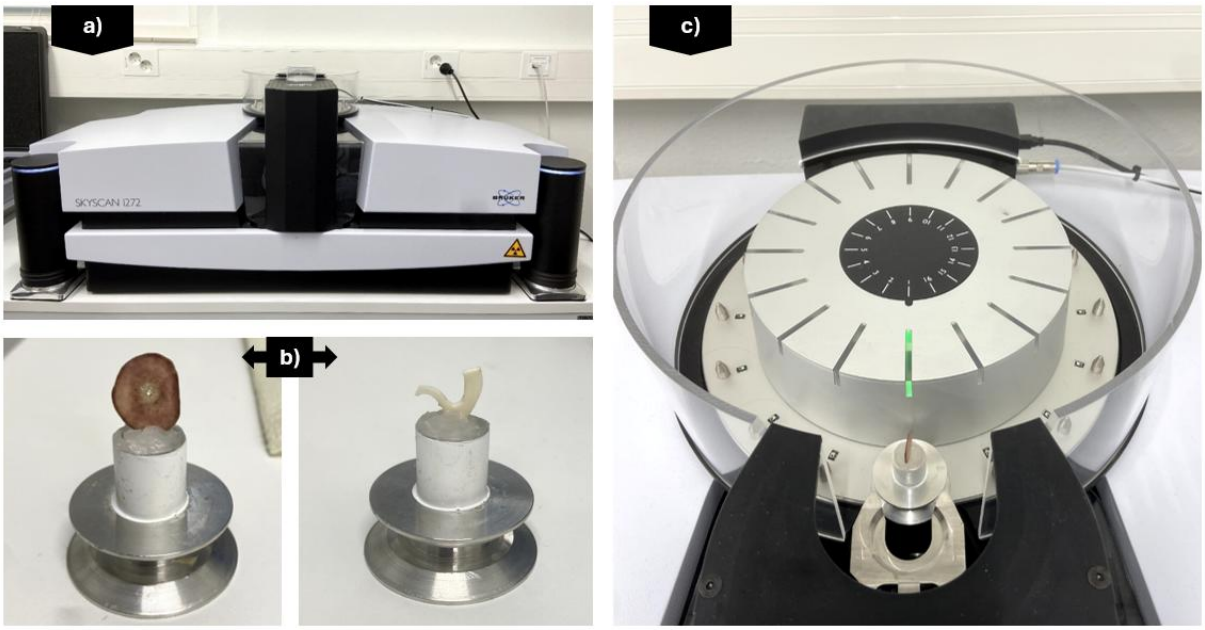

Figure 10. Micro-CT instrument components. a) The SkyScan 1272 desk-top micro-CT system. b) Sample mounts with antler (left) and tibia (right) samples. c) A close-up image of the sample changer.

Scanned images were reconstructed with NRecon software, where parameters such as the beam hardening correction, misalignment compensation, ring artifact reduction, and the attenuation boundaries were adjusted. The reconstructed results were viewed with DataViewer software as three orthogonal sections.

CTAn was used to determine the region of interest (ROI) in each sample. The antler base and tip samples were divided into three different measurement regions: centre,

intermediate, and peripheral (Figure 11). ROIs, circular in shape, were defined in relation to sample and area size. The size of the ROI was standardized as much as possible, however, the sample size varied between the same and different bone material. The ROI was kept the same size within each individual sample for all analysed regions. In the tibia samples, the ROI was identical in all measurements. However, in both antler tip and antler base samples, the size of the ROI varied between individuals due to differences in sample size and structure size. To enhance the statistical reliability, four ROIs were selected from each region of the antler base and tip samples whereas a total of four ROIs were chosen for each tibia sample. Relatively uniform structures free from large voids or structural irregularities were chosen as ROI sites to minimize variability and improve reproducibility. Additionally, the aspiration was to ensure that the chosen regions were entirely within the bone material, although in some cases it could not be avoided that the ROI was on the edge of the sample. The applied ROI sizes (area in μm^2 and corresponding pixels) are reported in Appendix 1.

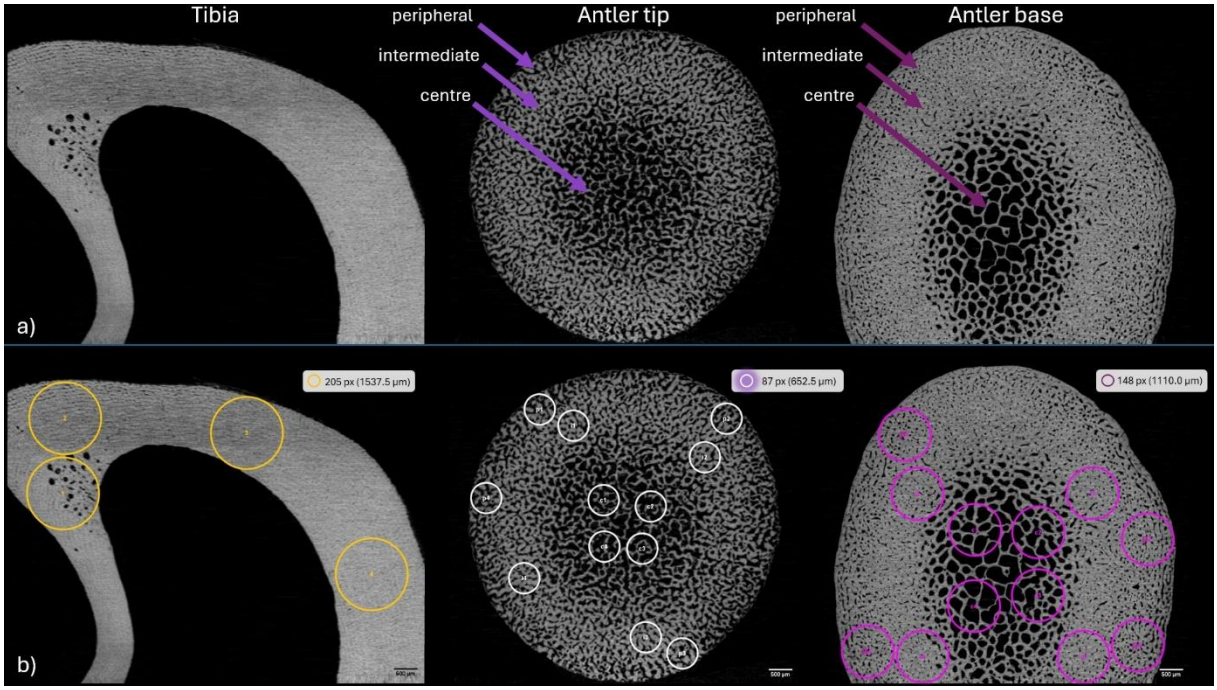

Figure 11. Tibia, antler tip, and antler base of one individual (ID 2). a) Regions determined for micro-CT measurements. b) ROI placement for each sample type displayed here. p = peripheral, i = intermediate, c = centre. For the tibia samples and each antler region, four ROIs were determined manually to fit tightly within the region of interest to secure a representative sample area. ROI sizes therefore varied between individuals depending on the anatomical boundaries of each sample.

The reconstructed data and ROIs were automatically processed as a batch with CTAn Batman (Batch Manager) software according to a task list defining plug-ins applied to

the dataset. For these analyses, five preset plug-ins were listed: *Thresholding* which determines lower and upper thresholds used in binarization, *3D and 2D analysis* for 2D line-by-line analysis and 3D analysis of the ROIs of the determined datasets, *Reload* which reloads the image data into the processing pipeline without removing the current ROI, and *Histogram* calculating the voxel density distribution within the dataset—either slice-by-slice (2D) or across the entire volume (3D). To gain bone mineral density (BMD) values from the histogram output, BMD calibrations were performed by using Bruker-Micro-CT BMD calibration phantoms 4mm in diameter, which had calcium hydroxylapatite (CaHA) concentrations of 0.25 and 0.75 $g.cm^{-3}$. These calibration rods were scanned with the same settings as the bone scans. Bruker-Micro-CT CT-Analyser (CTAn) software contains the opportunity to calibrate BMD either in units of attenuation coefficient or Hounsfield units. In this study, the calibration was done against attenuation coefficient with 0.250 and 0.750.

The morphometric parameters observed in this work and their descriptions are described in Table 3.

Table 3. The morphometric parameters analysed using micro-CT imaging technique.

Category	Abbreviation	Parameter	Definition	Unit
General parameters	BMD	Bone mineral density	*The volumetric density of calcium hydroxyapatite*	g/cm^3 CaHA
Porosity parameters	Po(cl)	Closed porosity	*The volume of non-interconnected pores*	%
	Po(op)	Open porosity	*The volume of interconnected pores*	%
	Po(tot)	Total porosity	*The total volume of all pores*	%
Trabecular parameters	BV/TV	Percent bone volume	*Ratio of the segmented bone volume to the total volume of the region of interest*	%
	Tb.N	Trabecular number	*The average number of trabeculae per unit length*	1/mm
	Tb.Th	Trabecular thickness	*Mean thickness of trabeculae*	mm
	Tb.Sp	Trabecular separation	*Mean distance between trabeculae*	mm

3.6 Data analysis

3.6.1 Data transfer and preprocessing

Here, data analysis is understood as the processes done with a separate program instead of the instruments' own programs. Each XRD sample file was processed one at a time with Origin software (version 16, 2023b, and 2025), the data analysis and graphing software developed by OriginLab Corporation. The data files were transferred to Origin by dragging and dropping them into a new workbook. The appropriate columns for the X-axis and Y-axis were selected, and the line tool was used to generate preliminary plots of the raw data. The noisy raw data required smoothing which was done by applying Adjacent-Averaging method with the window size of 15 points. This smoothing method applies the simplest averaging option available. A new column with smoothed data was generated after executing this action.

This step was followed by the correction of the baseline with Peak Analyzer tool employing BSpline interpolation. A Cubic B-Spline uses third-degree (cubic) polynomials for connecting groups of points. With this method, the input data is processed in segments which are fitted with a polynomial curve called Bezier splines. The auto-determined anchor points were adjusted, and new anchor points added manually as needed. An example of data smoothing and baseline correction is shown in the Figure 12. The subtraction was confirmed, after which a new workbook column was generated. Graph axes were modified by adjusting scale, labels, grids, and ticks as necessary. The finalized graphs were saved to avoid reprocessing during future analysis sessions.

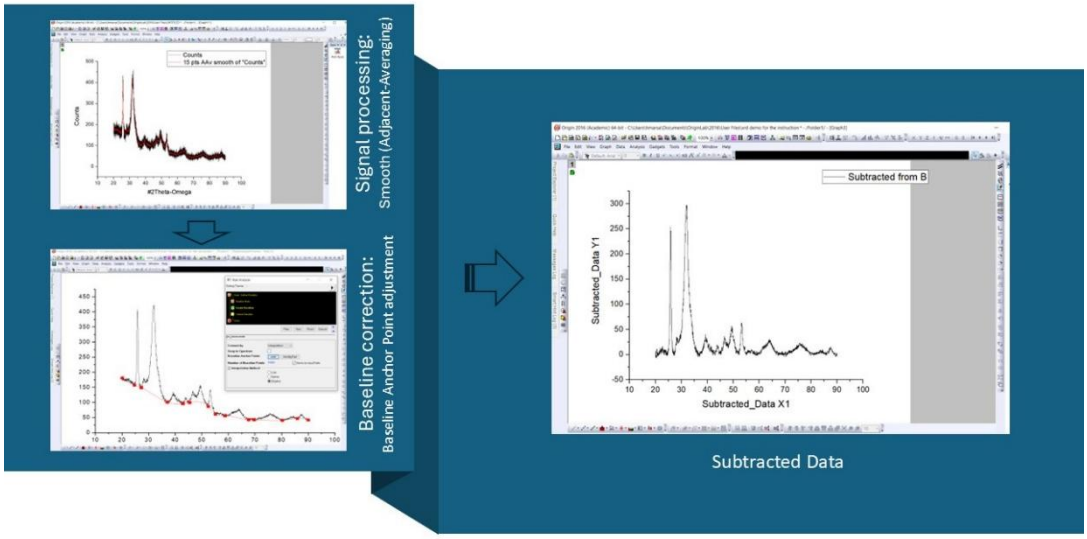

Figure 12. Example images of data smoothing (top left), baseline correction (lower left) and processed data (right). In the signal processing (smoothing), the black thicker spectrum is the original raw data, and the thin red line is the smoothed data.

For FTIR analyses performed using PerkinElmer Frontier IR, the baseline correction was done with the instrument's PerkinElmer Spectrum software. For the data obtained from the PerkinElmer Spectrum 100 instrument, transmittance spectra were first converted to absorbance with the equation Absorbance = 2 - log(%T) and then baseline corrected following the procedure described previously.

3.6.2 Peak identification

The Peak Analyzer tool was utilized to find peaks for each sample (Figure 13). The 'Find Peaks' feature allowed for both automated peak detection and manual peak adjustment. The 2nd Derivate plot was turned on to confirm whether any hidden peaks were present. The Threshold Height (%) function under the Peak Filtering setting of automatic peak finding is meant to limit the amount of data points, however, during the benchmarking phase, this was considered somewhat poorly suited for working with the dataset and the peaks were mostly manually labelled according to the characteristics of each sample. For this thesis, Quadratic Savitzky-Golay method for derivative smoothing was chosen since it seemed to lessen the detection of the background noise. The peak filtering group was determined by peak height. Threshold Height (%) determining the minimum height of the found peaks was set to either 2 or 3 while the Points of window - setting defining the intensity of the degree of derivative smoothing was 70-80 depending how strong the background noise was. While the majority of the peaks were derived

from the automated detection, some of them were manually adjusted and removed after considering the existence of the background noise in the data.

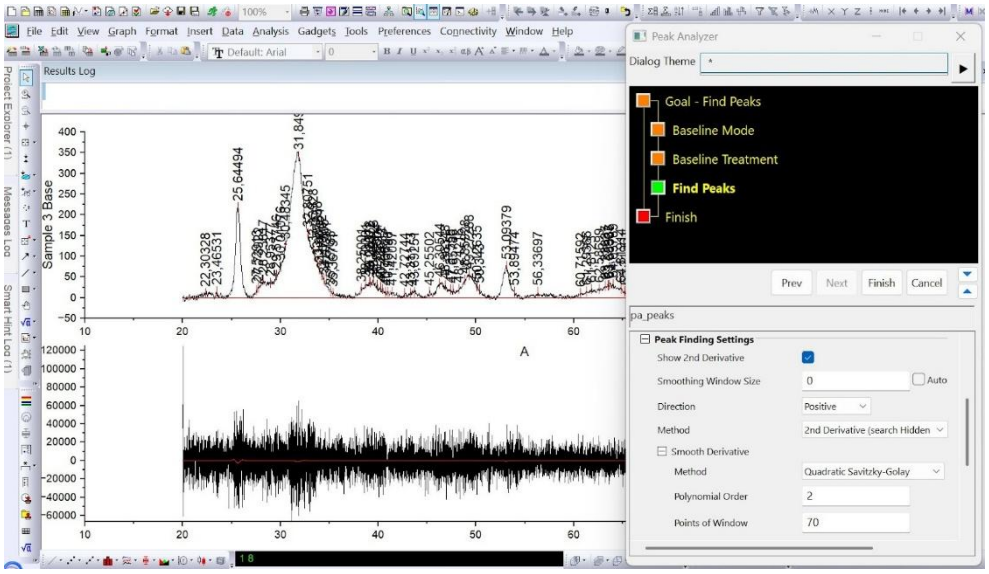

Figure 13. The layout of the Peak Analyzer tool. The analysed data is displayed on the top left. The 2nd Derivative method display is positioned below the data, assisting with the detection of possible hidden peaks in the data. The settings of the Peak Analyzer tool are adjusted in the dialog window, which is presented on the right.

FTIR spectra obtained with PerkinElmer Frontier IR instrument were initially processed with the instrument's PerkinElmer Spectrum software, which provided information about the wavenumbers where the peaks were at their highest (peak centres on the x-axis) and their absorbance (y-axis). In cases where expected peak locations already found in other samples were not automatically detected, missing peaks were identified manually using the Quick Peaks Gadget in order to maintain a consistent peak selection. Quick Peaks was also used to determine the relevant peaks from the data obtained from the PerkinElmer Spectrum 100 instrument since these were not separately defined in the data files.

3.6.3 Extraction of Peak Features

Curve fitting for plotted XRD data was performed by using a built-in Gauss function. This nonlinear fitting was implemented using the NonLinear Fitting (NLFit) dialog. The NLFit includes parameter initialization code which provides automatically assigned initial parameters. The baseline offset value y0 was always set to 0. To achieve the suitable fit, the fit was converged one iteration at a time until each peak had a seemingly suitable

fitting curve. The achieved peak centre, width and area were locked for less intense peaks whose fit varied every time a new iteration was added. After performing the fitting by clicking Fit, the succession of the fitting operation was confirmed by checking that there was a message stating the following: “Fit converged. Chi-Sqr tolerance value of 1E-9 was reached. The prompted reports of the results for each sample included parameter values and fit statistics for peak area, height, width, centre, FWHM, X and Y scale, and sigma of the peaks.

For the FTIR data, the full width at half maximum (FWHM) of the peak at 1000 cm^{-1} (ref. (Augusto de Castro et al., 2022) was done manually, as this measurement was needed to calculate a parameter presented in the following section. This process involved calculating the half value of the peak’s maximum intensity from the Y axis. This value was in turn used to determine the values of 2θ (X axis) from both sides of the peak (2Th min & 2Th max). The FWHM was obtained by subtracting the value of 2Th min from the value of 2Th max (Figure 14).

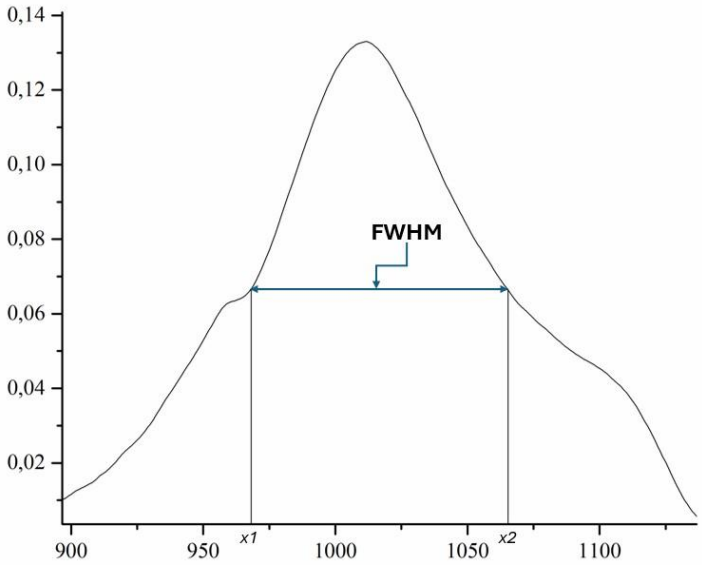

Figure 14. Representation of full width at half maximum (FWHM) of a spectral peak. FWHM is defined as the width of a peak measured at 50% of its maximum intensity, located by using two 2θ values, 2TH min (x1) & 2Th max (x2).

3.6.4 Parameters

XRD parameters chosen to be featured in this study were d-spacing, crystallite size, and c-axis orientation.

D-spacing, also known as interplanar spacing, defines the distance between two consecutive atomic planes in crystalline materials. It is determined with Bragg's equation:

$$d = n\lambda / (2sin\theta) \; or \; n\lambda = 2d \; sin \; \theta$$

where:

n is the order of diffraction

λ is the wavelength of incident radiation

d is the spacing of crystal planes

θ the peak position expressed in radians

To calculate the crystallite size, the 2θ value and the Full Width at Half Maximum (FWHM) of the prominent peaks were utilized in the Scherrer formula. The Scherrer formula is expressed as

$$D = K\lambda/\beta cos\theta$$

where:

D represents the crystallite size,

K is the shape factor, taken as 0.94 for the bone (Cañas-Gutiérrez et al., 2022),

λ denotes the wavelength of the X-ray radiation used (0.15406 nm),

β corresponds to the FWHM of the peak,

θ is the Bragg angle at the peak position.

C-axis orientation was analysed to assess how aligned the crystals were within each sample. This parameter was obtained by dividing the area of peak 0 0 2 by the area of peak 3 1 0.

Several parameters describing the characteristics of bone material were chosen for the FTIR analysis, and they are listed in Table 4 below.

Table 4. A summary of FTIR-derived parameters, spectral regions and ratios, interpretations, and the references from which the information was obtained.

The reported peak positions represent typical values from the literature. Since the samples and instruments vary depending on the experiment, some variation is expected between references and the current data.

Parameter	Spectral Ratio	Interpretation	Reference(s)
Amide I to phosphate	1635 cm^{-1} / 1000 cm^{-1}	*The relative organic preservation*	Augusto de Castro et al. 2022
Amide II to phosphate	1547 cm^{-1} / 1000 cm^{-1}	*The relative organic preservation*	Augusto de Castro et al. 2022
Amide III +Collagen to phosphate	(1201 cm^{-1} + 1240 cm^{-1} + 1281 cm^{-1}) / 1000 cm^{-1}	*Indicator for changes in protein integrity vs. mineral*	Augusto de Castro et al. 2022
Amide I +Amide II to phosphate	(1547 cm^{-1} + 1635 cm^{-1}) / 1000 cm^{-1}	*The total collagen preservation in relation to minerals*	Augusto de Castro et al. 2022
Amides +Collagen to phosphates	(1201 cm^{-1} + 1240 cm^{-1} + 1281 cm^{-1} + 1635 cm^{-1} + 1547 cm^{-1}) / 1000 cm^{-1}	*The organic-to-mineral content ratio*	Augusto de Castro et al. 2022
Carbonate accumulation	870 cm^{-1} / 1635 cm^{-1}	*The relative accumulation of carbonate in relation to the organic collagen matrix*	Augusto de Castro et al. 2022
Carbonate content of bioapatite CO3/PO4	1415 cm^{-1} / 604 cm^{-1}	*The bone mineral quality (the level of carbonate substitution in the apatite lattice)*	Dal Sasso et al. 2018
Carbonate to mineral ratio	870 cm^{-1} / (553 cm^{-1} + 597 cm^{-1} + 1000 cm^{-1})	*The degree of carbonate substitution relative to the total phosphate content*	Augusto de Castro et al. 2022
Crystallinity	1 / FWHM of 1000 cm^{-1}	*The degree of structural order within the bone mineral*	Augusto de Castro et al. 2022
Infrared Splitting Factor (IRSF)	(604 cm^{-1} + 563 cm^{-1}) / 590 cm^{-1}	*The degree of crystallization of bone bioapatite*	Colmenares-Prado et al. 2025; Dal Sasso et al. 2018; France et al. 2020
Mineral to matrix ratio	area of 900 - 1200 cm^{-1} / area of 1600-1720 cm^{-1} Alternative: (553 cm^{-1} + 597 cm^{-1}) / 1635 cm^{-1} *	*The degree of mineralization (the relative ratio of inorganic vs. organic components)*	Kourkoumelis et al. 2019; Augusto de Castro et al. 2022 *
Mineral maturity	1030 cm^{-1} / 1101 cm^{-1} Alternative: 604 cm^{-1} / 553 cm^{-1} *	*Indicator for the degree of apatite crystallinity and maturity (crystal size & structural order)*	Kourkoumelis et al. 2019; Augusto de Castro et al. 2022 *

Parameter	Spectral Ratio	Interpretation	Reference(s)
Secondary structure of proteins	1635 cm^{-1} / 1240 cm^{-1}	*The folding and structure of collagen*	Augusto de Castro et al. 2022

3.7 Statistical analysis

To determine whether there were statistically significant differences in the calculated parameters among the three bones, IBM SPSS software [version 29.0.0.0 (241)] was used to compute a one-way ANOVA which was followed by Tukey's Honestly Significant Difference (HSD) test for multiple comparisons.

4 Results

4.1 XRD results

The peak finding process involved a combination of intensity thresholding and second derivative methods to detect possible overlapping and hidden peaks. All XRD spectra were baseline corrected and smoothed prior to further data handling to reduce possible background noise (see Appendix 2 for raw XRD data, and Appendix 3 for processed data). Despite all the data being processed identically with these preprocessing steps, spectral quality and resulting number of detected peaks varied across the samples. Figure 15 shows two spectra, in one of which (a) finding peaks using the Origin program was very straightforward, while in the other (b) the background noise was stronger and resulted in a higher number of detected peaks. Clearer spectra typically resulted with 37-38 detected peaks, whereas the largest peak counts in the spectra varied between 50 and 65. It is likely that the outcome of the latter was due to the sensitive second derivative method interpreting residual noise as small peaks. It is possible that sample material properties such as sample density, crystallinity, or the amount of organic material may have affected the signal and background noise, leading to the observed differences. On average, it appeared that fewer peaks were observed in tibia samples than in antler samples, which would support the assumption that the composition of the sample material acted as an influencing factor on the quality of the analysis and the success of the peak finding. However, upon closer inspection, the location of some of the peaks appearing in spectra yielding a greater number of peaks resembled those of known diffraction angles of hydroxyapatite, suggesting a possibility that not all were caused by background contribution, although noise-induced artifacts cannot be entirely excluded.

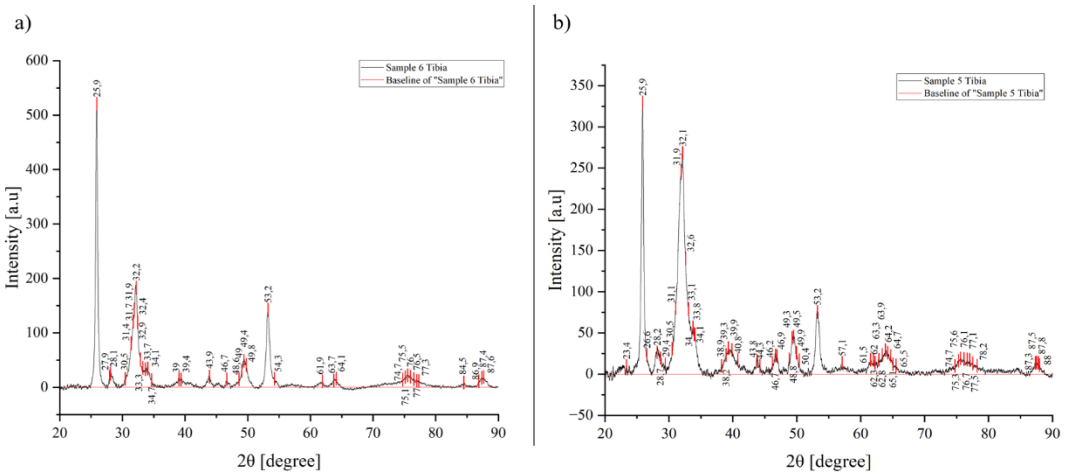

Figure 15. XRD spectra of two tibia samples with differing noise levels. a) A spectrum with a cleaner profile with 38 detected peaks. b) A noisier spectrum with 54 detected peaks.

The obtained X-ray diffraction patterns of antler and tibia samples were reviewed against the 2θ positions and Miller indices (hkl) of stoichiometric hydroxyapatite (HAp) standard reference (coded as 96-901-3628 in Crystallography Open Database). The observed peak positions matched with those of the reference pattern, which indicates that a hydroxyapatite-like phase is present in the mineral composition of both antler and tibia. Peaks corresponding to the crystallographic planes at (0 0 2), (1 1 2), and (0 0 4) were the most prominent among the analysed samples. An example of the diffraction patterns of different samples from the same individual and the peaks corresponding to the characteristic crystallographic planes of hydroxyapatite standard are presented in the Figure 16. The peaks clearly matching the reference have been marked with dotted lines and were observed in all the samples.

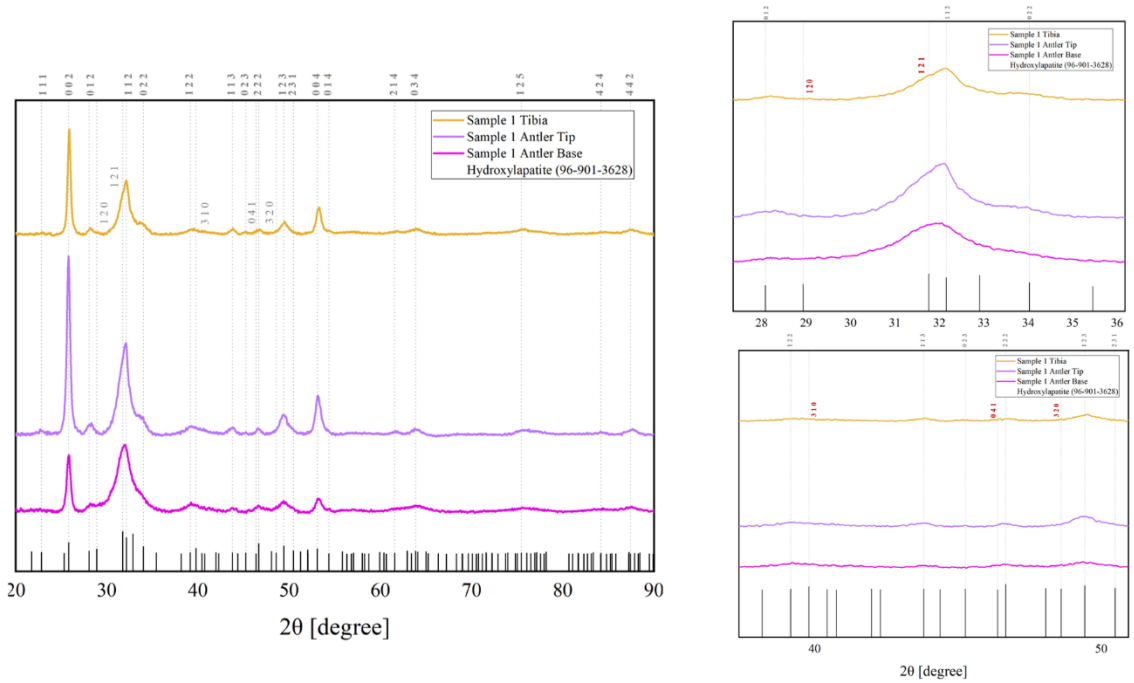

Figure 16. XRD Diffraction patterns of tibia (yellow/top), antler tip (lilac/middle), and antler base (violet/bottom) were compared with each other and the standard for hydroxyapatite (HAp). a) X-ray diffractogram of sample 1 with reference peak positions for HAp annotated by vertical dotted lines and labelled with corresponding Miller indices (hkl). The observed peak positions in the sample correspond to positions seen in the HAp standard (black vertical lines), suggesting the presence of a hydroxyapatite-like mineral. b) Expanded view between the angles 28-36 (above) and angles 40-50 (below), showing the locations of the peaks 1 2 0, 1 2 1, 3 1 0, 0 4 1 and 3 2 0 in more detail.

The diffraction peaks of the spectra underwent peak fitting in order to calculate parameters related to the crystal structure, such as crystal size (Figure 17). The most distinct peaks were fitted successfully in most cases; however, the software was unable to separate (deconvolve) or reliably fit subpeaks in areas such as the peak complex including planes 1 2 1, 1 1 2, and 0 0 2. Therefore, only the two best defined peaks, 0 0 2 and 0 0 4, were selected for analysis. These peaks were systematically located at the similar 2θ values in all samples, corresponding to identifiable crystal surfaces of HAp. Peak fitting graphs for each sample have been included in Appendix 4.

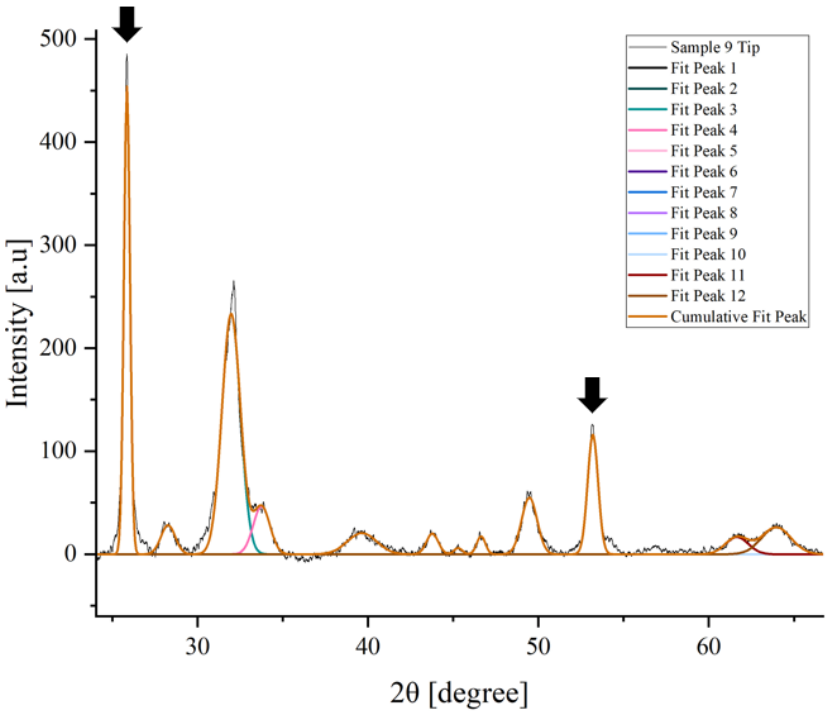

Figure 17. XRD spectrum of a sample 9 antler tip (black line) and attempted fit (orange line). Two clearly determinable peaks (marked with black arrows) were selected for further analysis.

Structural characteristics of the samples were analysed from the XRD parameters of d-spacing, crystallite size and the 0 0 2 / 3 1 0 peak area ratio as an indicator of c-axis orientation. To observe the existing lattice features and crystallite organisation across the bone samples, the peak position (2θ), full width at half maximum (FWHM), and interplanar spacing of the 0 0 2 and 0 0 4 reflections were assessed (Table 5 and Appendix 5). When comparing the mean 2θ value for the 0 0 2 peak, it was observed to be highest in tibia (25.88° ± 0.06), while in the antler samples it was very similar at both the tip (25.79° ± 0.11) and the base (25.79° ± 0.12). The slight shift in the position of the tibial peak may possibly be associated with a subtle reduction in the lattice spacing or greater crystallinity compared to antlers.

In terms of FWHM, this value was found to be the smallest in tibia (0.44° ± 0.03), whereas in the antlers these values were larger than in the tibia and resembled each other between the tip (0.52° ± 0.09) and the base (0.52° ± 0.06). The broader peaks in the antler could indicate a smaller crystallite size. With d-spacing, the mean value for tibia was 3.44 Å (with SD of ± 0.008) while for both antler tip and base it was 3.45 Å with SDs of 0.01 and ± 0.02, respectively.

The 2θ position of the 0 0 4 peak varied slightly among the samples. The largest mean 2θ value was determined from tibia samples (53.25° ± 0.07), while antler tip and antler base expressed marginally lower values similar to each other (53.19° ± 0.11 and 53.20° ± 0.11). This slight shift towards a higher angle observed in the tibia samples is in line with the phenomenon observed in the 0 0 2 peak. A similar trend was visible with the FWHM values of the 0 0 4 peak. The narrowest peak was found in tibia (0.70° ± 0.08), from where the progressive increase in value was noticeable first in the antler tip (0.75° ± 0.09) and then at its highest in the antler base (0.80° ± 0.13). The observations on the 2θ position and FWHM of the 0 0 4 peak reinforce the trend met in the 0 0 2 reflection, the tibia being expressed with narrower, higher-angle peaks. Although minor differences in peak position and FWHM were noted, the d-spacing values for the 0 0 4 peak appeared to be consistent across all groups (1.72 Å ± 0.002–0.003), therefore suggesting that the crystallographic plane in question possess a stable interplanar spacing.

Table 5. Comparison of two theta peak position (2θ), FWHM, and Interplanar Spacing (d) for tibia, antler base, and antler tip in planes (hkl) 0 0 2 and 0 0 4.

The values for FWHM and calculations for d-spacing are based on the 2θ values obtained with the NonLinear Fitting (NLFit) function. All the values are presented as mean ± SD (n=9). D-spacing was calculated using Bragg's law: $d = n\lambda / (2\sin\theta)$, with Cu Kα (λ = 1.5406 Å).

Miller indices (hkl)	Sample type	2θ [°]	FWHM	d [Å]
0 0 2	Tibia	25.88 ± 0.06	0.44 ± 0.03	3.44 ± 0.008
0 0 2	Antler tip	25.79 ± 0.11	0.52 ± 0.09	3.45 ± 0.01
0 0 2	Antler base	25.79 ± 0.12	0.52 ± 0.06	3.45 ± 0.02
0 0 4	Tibia	53.25 ± 0.07	0.70 ± 0.08	1.72 ± 0.002
0 0 4	Antler tip	53.19 ± 0.11	0.75 ± 0.09	1.72 ± 0.003
0 0 4	Antler base	53.20 ± 0.11	0.80 ± 0.13	1.72 ± 0.003

Crystallite size was evaluated from the full width at half maximum (FWHM) of the peak responding to the 0 0 2 reflection by using the Scherrer equation (Appendix 5). The calculated mean values of each group are visualized in Figure 18, and the results from the statistical analyses are summarized in Table 6. Of the three sample types examined, the largest average crystal size was observed in tibial samples (mean = 19,54 nm), whereas for antler tip and antler base these values were 16,88 nm and 16,56 nm,

respectively. The variation in crystal size was observed to be greatest in antler tip samples, where the standard deviation was 2,56 nm, and smallest in tibial samples (SD = 1,19 nm). Statistically significant difference between tibia and antler samples was reached (ANOVA p-value = 0.006), while there was no significance between antler tip and antler base.

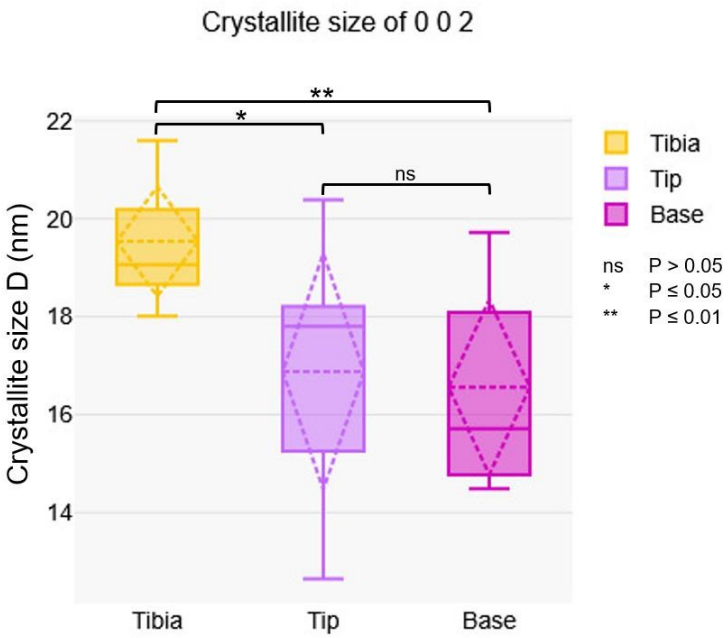

Figure 18. Crystallite size of the 0 0 2 peak across tibia (yellow), antler tip (lilac), and antler base (violet). The horizontal solid line in each box represents the median; horizontal dashed line presents the mean, and diamond shapes extending from that represent standard deviation; the box edges represent the interquartile range; and whiskers extend to the minimum and maximum values. The statistical significance between groups determined with Tukey's HSD have been indicated by different asterisks above the boxes, where ns = not significant, * = p ≤ 0.05, ** = p ≤ 0.01, *** = p ≤ 0.001.

Table 6. ANOVA and Tukey's Test Results for the Crystallite size of Peak 0 0 2.

The mean difference is significant at the 0.05 level*. ANOVA for Peak 0 0 2: F = 6.26, p = 0.006.

Tukey's Multiple Comparison Test: Crystallite size (0 0 2)	**Mean Difference**	**Std. Error**	**Sig.**	**95% CI**	**Significant?**
Tibia vs. Antler tip	2.66*	0.92	0.022	(0.35, 4.97)	Yes
Tibia vs. Antler base	2.98*	0.92	0.01	(0.67, 5.28)	Yes
Antler tip vs. Antler base	0.32	0.92	0.94	(-1.99, 2.63)	No

As with the 0 0 2 peak, the calculated crystal size for peak 0 0 4 was largest in the tibia samples (mean = 13,47 nm) and smallest in the antler base samples (mean = 11,74 nm), with the antler tip samples falling in between with an average value of 12,53 nm (Figure

19). This time the largest standard deviation within sample groups was met in antler base (SD = 1.89 nm), while it was the smallest in antler tip (SD = 1.40 nm). Unlike with peak 0 0 2, no statistical significance was found between the samples (p = 0.1) when basing the calculations on the values derived from peak 0 0 4 (Table 7).

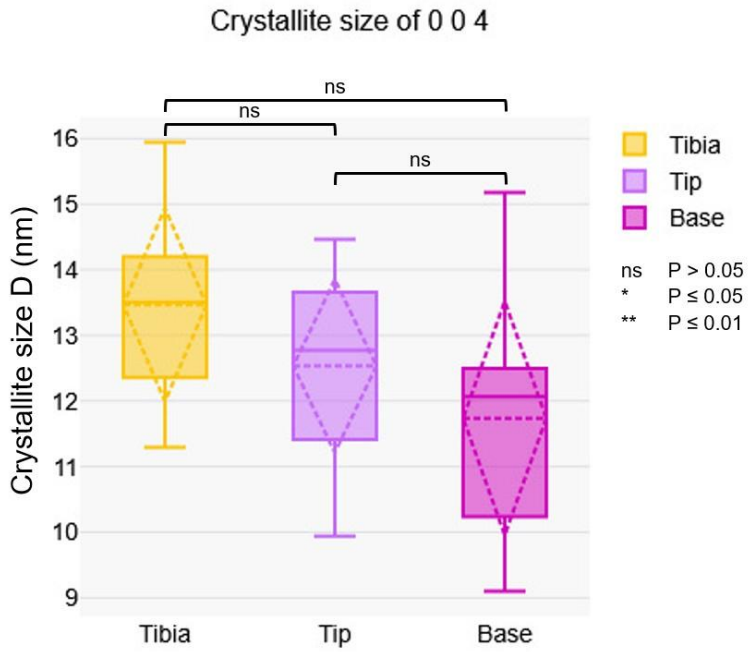

Figure 19. Crystallite size of the 0 0 4 peak across tibia (yellow), antler tip (lilac), and antler base (violet). Unlike the 0 02, no significant (ns) differences were noted regarding the peak 0 0 4. The horizontal solid line in each box represents the median; horizontal dashed line presents the mean, and diamond shapes extending from that represent standard deviation; the box edges represent the interquartile range; and whiskers extend to the minimum and maximum values.

Table 7. ANOVA and Tukey's Test Results for the Crystallite size of Peak 0 0 4.

The mean difference is significant at the 0.05 level*. ANOVA for Peak 0 0 4: F = 2.53, p = 0.1.

Tukey's Multiple Comparison Test: Crystallite size (0 0 4)	**Mean Difference**	**Std. Error**	**Sig.**	**95% CI**	**Significant?**
Tibia vs. Antler tip	0.93	0.77	0.46	(-0.99, 2.85)	No
Tibia vs. Antler base	1.73	0.77	0.08	(-0.19, 3.65)	No
Antler tip vs. Antler base	0.80	0.77	0.56	(-1.12, 2.71)	No

The c-axis orientation of the samples was assessed by comparing the area ratio of the 0 0 2 and 3 1 0 peaks ($A_{(002)}/A_{(310)}$). Distribution for each sample group is presented in Figure 20. The mean of this value was found to be greatest in tibia (3.62 ± 1.60), followed

by the antler tip (3.17 ± 1.96) and finally lowest in the antler base (2.58 ± 1.28). No significant difference between the sample groups was found (Table 8).

The 0 0 2 peak could be clearly distinguished in the peak fitting step. The 3 1 0 peak was determined as a single peak, although at least another, possible subpeak, also appeared in its vicinity. This may have affected the accuracy of the area of the 3 1 0 peak and therefore the calculated ratio (see Appendix 6 for calculations).

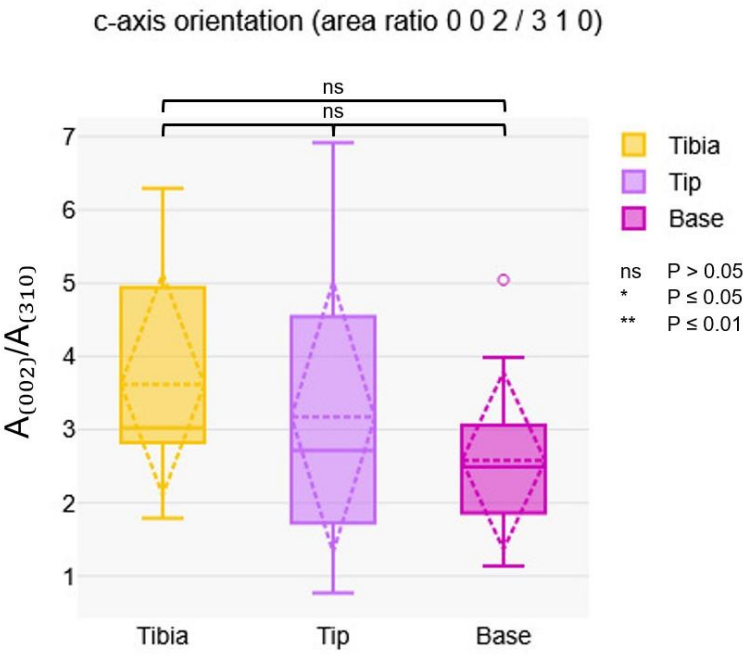

Figure 20. C-orientation derived from the area ratio between 0 0 2 and 3 1 0 across tibia (yellow), antler tip (lilac), and antler base (violet). No significant (ns) differences were noted regarding this parameter. The horizontal solid line in each box represents the median; horizontal dashed line presents the mean, and diamond shapes extending from that represent standard deviation; the box edges represent the interquartile range; whiskers extend to the minimum and maximum values; and the light dot indicates the presence of suspected outliers with k = 1.5.

Table 8. ANOVA and Tukey's Test Results for the c-axis orientation (0 0 2 / 3 1 0 peak area ratio).

The mean difference is significant at the 0.05 level*. ANOVA: F = 0.91, p = 0.42.

Tukey's Multiple Comparison Test: c-axis orientation (area ratio 0 0 2/3 1 0)	**Mean Difference**	**Std. Error**	**Sig.**	**95% CI**	**Significant?**
Tibia vs. Antler tip	0.45	0.77	0.83	(-1.48, 2.38)	No
Tibia vs. Antler base	1.04	0.77	0.38	(-0.89, 2.97)	No
Antler tip vs. Antler base	0.59	0.77	0.73	(-1.34, 2.52)	No

4.2 ATR-FTIR results

The analyses of this study revealed absorption bands characteristic of bone: amides, carbonates, and phosphate groups. The occurring peak features across the samples have been listed on Table 9 with their wavenumber (cm^{-1}) and assignment according to previous publications. Overall, all nine samples seemingly have the same main peak positions with subtle differences, reflecting the presence of the same functional groups. The relative intensities and sharpness of the peaks, however, differ notably across the samples, which may indicate variance in the nature of their structural properties and the maturity of minerals. The raw and processed instrument data from both PerkinElmer Frontier IR and Spectrum 100 have been included in Appendix sections 7 and 8.

Table 9. Wavenumbers found in present data, and their assignments based on the previous literature.

The spectra obtained with the Frontier IR instrument were analysed more extensively in the case of peak locations, while the observations on the spectra obtained with the Spectrum 100 were focused on the peak values needed for parameter calculations. The peak positions used in parameter calculations are marked with bold numbers.

Wavenumber cm^{-1} (n=27)	Assignment	Reference(s)
555, 598 (Spectrum 100)	PO4 3-v4	Augusto de Castro et al. 2022; Kourkoumelis & Tzaphlidou 2010; Kourkoumelis et al. 2019
871 (Frontier IR) **872** (Spectrum 100)	CO3 2–v2	Augusto de Castro et al 2022; Kimura-Suda & Ito 2017; Kourkoumelis & Tzaphlidou 2010; Kourkoumelis et al. 2019
960 (Frontier IR)	PO4 3-v1	Augusto de Castro et al. 2022; Kourkoumelis & Tzaphlidou 2010; Kourkoumelis et al. 2019; Movasaghi et al., 2008
1011, 1103 (Frontier IR) **1009** (Spectrum 100)	PO4 3-v3	Augusto de Castro et al. 2022; Kimura-Suda & Ito 2017; Kourkoumelis & Tzaphlidou 2010; Kourkoumelis et al. 2019
1204 (Frontier IR)	Collagen proteins-amide III	Augusto de Castro et al. 2022; Kimura-Suda & Ito 2017
1239 (Frontier IR)	Amide III	Kimura-Suda & Ito 2017; Kourkoumelis & Tzaphlidou 2010; Kourkoumelis et al. 2019
1281 (Frontier IR)	Amide III	Colmenares-Prado & Martínez Cortizas 2025; Stani et al., 2020

Wavenumber cm^{-1} (n=27)	Assignment	Reference(s)
1339 (Frontier IR)	CH2 wagging; Collagen	Augusto de Castro et al. 2022; Kourkoumelis & Tzaphlidou 2010; Kourkoumelis et al. 2019
1408 (Spectrum 100)	CH3 asymmetric deformation	Augusto de Castro et al. 2022
1448 (Frontier IR)	δ(CH2), lipids, fatty acids	Augusto de Castro et al. 2022; Baker et al., 2014
1546 (Frontier IR)	δ(N-H) ν(C-N), amide II	Augusto de Castro et al. 2022; Baker et al. 2014, Kimura-Suda & Ito 2017; Kourkoumelis & Tzaphlidou 2010; Kourkoumelis et al. 2019; Morris & Finney 2004; Movasaghi et al. 2008
1639 (Frontier IR) **1636** (Spectrum 100)	ß-sheet structure of amide I	Augusto de Castro et al. 2022; Baker et al. 2014, Kimura-Suda & Ito 2017; Kourkoumelis & Tzaphlidou 2010; Kourkoumelis et al. 2019; Morris & Finney 2004; Movasaghi et al. 2008
2854 (Frontier IR)	νSCH2, lipids	Augusto de Castro et al. 2022; Baker et al. 2014; Kourkoumelis and Tzaphlidou, 2010
2875 (Frontier IR)	νSCH3	Augusto de Castro et al. 2022; Kourkoumelis & Tzaphlidou 2010
2929 (Frontier IR)	νASCH2, lipids	Augusto de Castro et al. 2022; Baker et al. 2014; Kourkoumelis & Tzaphlidou 2010
2959 (Frontier IR)	νASCH3, lipids	Augusto de Castro et al. 2022; Baker et al. 2014; Kourkoumelis & Tzaphlidou 2010
3075 (Frontier IR)	Amide B	Augusto de Castro et al. 2022; Kourkoumelis & Tzaphlidou 2010
3297 (Frontier IR)	Hydroxy group. H-bonded OH stretch, Amide A (N-H stretching)	Coates, 2006; Kourkoumelis & Tzaphlidou 2010; Martínez Cortizas and López-Costas, 2020; Morris & Finney 2004; Movasaghi et al. 2008

The most distinguishable spectral features derived from PerkinElmer Frontier IR have been presented in Figure 21. In the 4000-2500cm^{-1} region (single bond region), features indicating presence of organic and hydroxyl groups were observed. Within this region, peaks reflecting symmetric and asymmetric stretching vibrations of methylene groups were visible at ~ 2854cm^{-1} and ~2929cm^{-1}, appearing as tiny sharp protrusion in some of the samples, whereas some were more subtle. Additionally, barely visible bumps at

~2875 cm^{-1} ($vsCH_3$) and ~2959 cm^{-1} ($vasCH_3$) were noted, reflecting methyl group stretching associated with lipides. A broad absorption band with its centre approximately at ~3297cm^{-1} was observed, this feature being associated with hydrogen-bonded hydroxyl groups and amide A (N–H stretching). In connection to this feature, a weak band corresponding to amide B was noted at ~3075cm^{-1}. No peaks were evident in the 2500-2000 cm^{-1} region (triple bond region).

The region 2000-1500cm^{-1} (double bond region) included prominent peaks at ~1639cm^{-1} and ~1546cm^{-1} across all the samples, which correspond to the Amide I and Amide II bands characteristic of collagen. Amide III band appeared with relative intensity around ~1239cm^{-1}. The strongest peak was visible in the 1500-400cm^{-1} region at ~1011cm^{-1} with associated shoulders around ~960cm^{-1} and ~1103cm^{-1}, indicating the presence of phosphate groups from hydroxyapatite, which is the major mineral phase in bone. Carbonate peak around ~871cm^{-1} was also present, suggesting carbonate substitution in the mineral matrix. A peak was observed near 1408cm^{-1}, which may correspond either to CH_3 (methyl) asymmetric deformation associated with proteinaceous material, or to carbonate substitution within the bone mineral matrix.

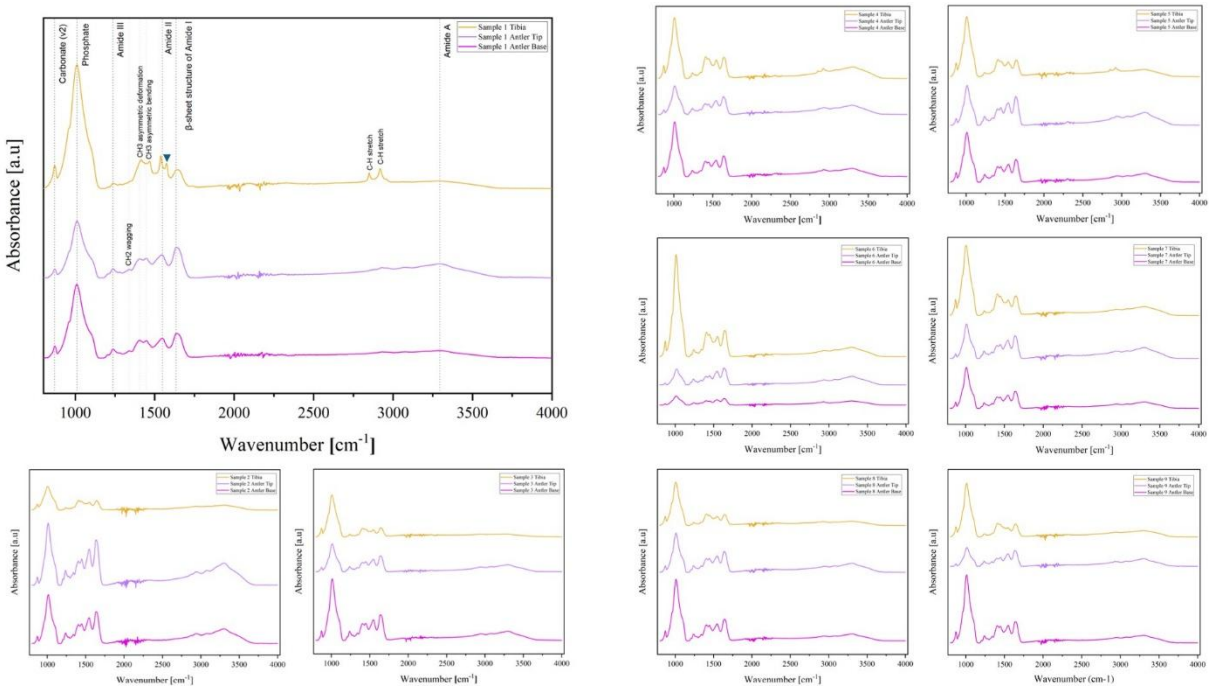

Figure 21. Representative ATR-FTIR absorbance spectrums of tibia (yellow/top), antler tip (lilac/middle), and antler base (violet/bottom) for each sample obtained from PerkinElmer Frontier IR. Prominent peaks corresponding to Amide I and Amide II were observed, together with phosphate related peaks and

carbonate peaks. Sharp peak at 1575cm^{-1} (blue triangle) was only observed in tibial sample of individual #1.

In this study, the height of the peaks in the ATR-FTIR spectra were treated as a measure of peak absorbance intensities. For the carbonate content of bioapatite (Dal Sasso et al., 2018) and carbonate to mineral ratio (Augusto de Castro et al., 2022) parameters, peaks were evaluated from spectra measured with PerkinElmer Spectrum 100 FT-IR spectrometer. Mineral to matrix ratio, mineral maturity, and crystallinity index, also known as infrared splitting factor (IRSF), were also derived from these measurements by using peak information received from area 400-800 cm^{-1} (Augusto de Castro et al., 2022; Colmenares-Prado et al., 2025; Dal Sasso et al., 2018; France et al., 2020). Therefore, there are two sets of values for the mineral to matrix ratio, mineral maturity, and crystallinity parameters, which are compared to see whether the trend changes between differently acquired ratios. The parameter calculations have been included in the Appendix sections 9 and 10.

Mineral to matrix ratio was calculated from PerkinElmer Frontier IR measurements by dividing the absorbance of the phosphate peak between 900-1200 cm^{-1} with absorbance of the amide I peak between 1600-1720 cm^{-1} (Kourkoumelis et al., 2019), with the peaks in the spectra of this study being centred on the average locations of 1011 cm^{-1} and 1639cm^{-1}. Based on this approach, the mineral to matrix ratio was observed to be significantly higher in tibia (mean = 4.12) compared to antler tip (mean = 1.52) and antler base (mean = 2.46), the ANOVA score being $p < 0.001$ (Figure 22). Furthermore, Tukey's post hoc test showed that this ratio in tibia was significantly higher compared to both antler locations, the mean difference between tibia and tip being 2.60 with p-value of <0.001, while these values between tibia and base were 1.66 and $p = 0.001$. It was noted that the mean difference of 0.94 between base and tip was not significant ($p = 0.072$).

According to literature (Augusto de Castro et al. 2022), mineral to matrix ratio can also be evaluated from the absorbance ratio calculated by adding the values of the peaks at ~553 cm^{-1} and ~597 cm^{-1} together and dividing this by the peak at ~1635 cm^{-1}. These absorbance ratios were derived from the PerkinElmer Spectrum 100 FT-IR measurements. In the present data, the average locations of these peaks were at 555

cm^{-1}, 598 cm^{-1}, and 1636 cm^{-1} (the peak at 1639 cm^{-1} in Frontier IR measurements). A trend similar to the previous assessment was also observed with this approach (Figure 22); tibia was significantly higher (p = <0.001) than antler with the mean value of 5.12, which was followed by antler base (mean = 3.16) and antler tip (mean = 1.99). The mean difference between tibia and tip was 3.12 (p = <0.001), and 1.96 between tibia and base (p = <0.001). The mean difference between base and tip was 1.17, with a p-value being very close to the significance level (p = 0.051).

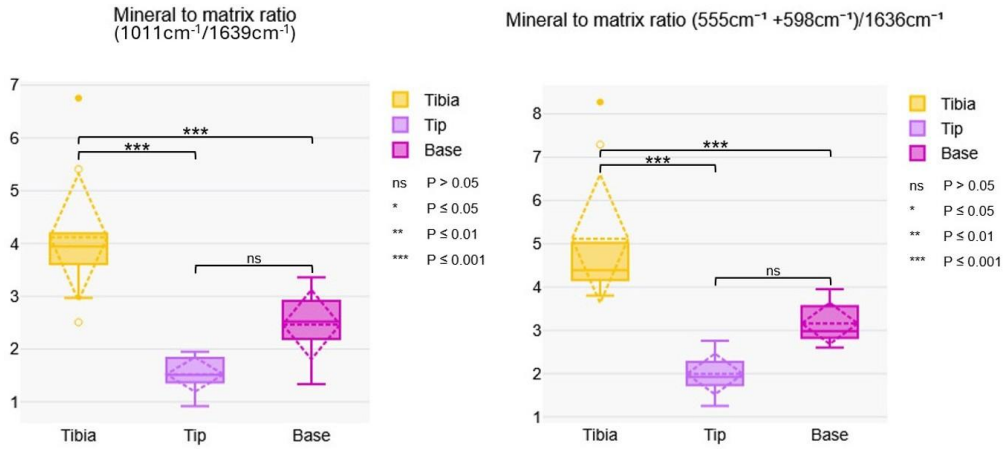

Figure 22. Mineral to matrix ratio across the antler and tibial bones implemented using two different approaches. The horizontal solid line in each box represents the median; horizontal dashed line presents the mean, and diamond shapes extending from that represent standard deviation; the box edges represent the interquartile range; whiskers extend to the minimum and maximum values; and the light dots indicate the presence of suspected outliers with k = 1.5 while black dots represent outliers with k=3. The statistical significance between groups determined with Tukey's HSD have been indicated by different asterisks above the boxes, where ns = not significant, * = p ≤ 0.05, ** = p ≤ 0.01, *** = p ≤ 0.001.

Mineral maturity was first calculated by dividing the peak at approximately 1011 cm^{-1} by subpeak at 1103 cm^{-1}, adapted from the ratio presented as 1030/1101 cm^{-1} by Kourkoumelis and colleagues (2019). Tibia, antler tip and antler base had the mean values of 3.25, 3.03, and 3.14, ANOVA showing no significant difference between these structures (p = 0.229). Additionally, PerkinElmer Spectrum 100 FT-IR measurements were utilized to obtain this parameter (Figure 23). By dividing peak at 598 cm^{-1} by peak at 555 cm^{-1}, the mineral maturity ratio was determined to be the highest in the antler tip with mean value of 0.55, ANOVA score of p = 0.008 indicating a significant difference to antler base (mean = 0.53) and tibia (mean = 0.52). More specifically, Tukey's post hoc test revealed that the mean difference of 0.025 between antler tip and antler base was significant (p = 0.045), and that the divergence between the tip and the tibia was yet greater in the comparison (MD = 0.033, p = 0.008). Manifestation of the statistical

significance in the latter calculation method could possibly indicate that the choice of peak points used in ratio evaluation may influence the interpretation of the parameter.

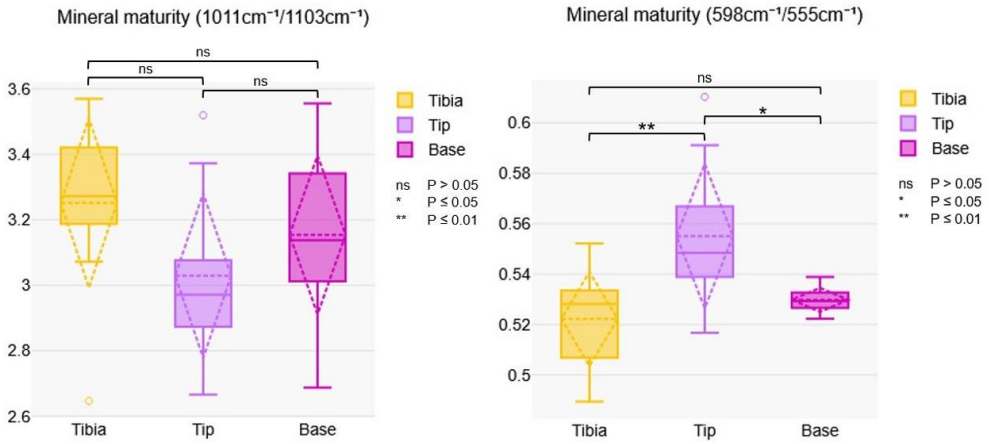

Figure 23. Mineral maturity derived from two calculation methods. The horizontal solid line in each box represents the median; horizontal dashed line presents the mean, and diamond shapes extending from that represent standard deviation; the box edges represent the interquartile range; whiskers extend to the minimum and maximum values; and the dots represent outliers. The statistical significance between groups determined with Tukey's HSD have been indicated by different asterisks above the boxes, where ns = not significant, * = $p \leq 0.05$, ** = $p \leq 0.01$, *** = $p \leq 0.001$.

To assess crystallinity, the inverse-bandwidth of the peak around 1011 cm^{-1} phosphate mode was calculated (1/FWHM of 1000 cm^{-1} in Augusto de Castro et al. 2022). The full width at half maximum was evaluated manually from this main phosphate peak (see Appendix 11). When looking at the internal values of individuals in terms of tibia and antlers, the greatest FWHMs were met in tibia, the exception being sample 6, where the antler base had the largest FWHM. The internal and inter-sample variability regarding the analysed antlers was quite uniform, with some individuals exhibiting slightly larger values at the base region compared to tip, whereas the remaining individuals had a reverse trend. The peak profile in most of the samples appeared smooth in the region through which the manually determined FWHM line passes, however, in some individuals, small sub-features were distinguishable (Figure 24). Smooth profiles were observed in most of the antler tip and base samples, with two exceptions in both groups (ID #4 and #6 for tip, #5 and #6 for base).

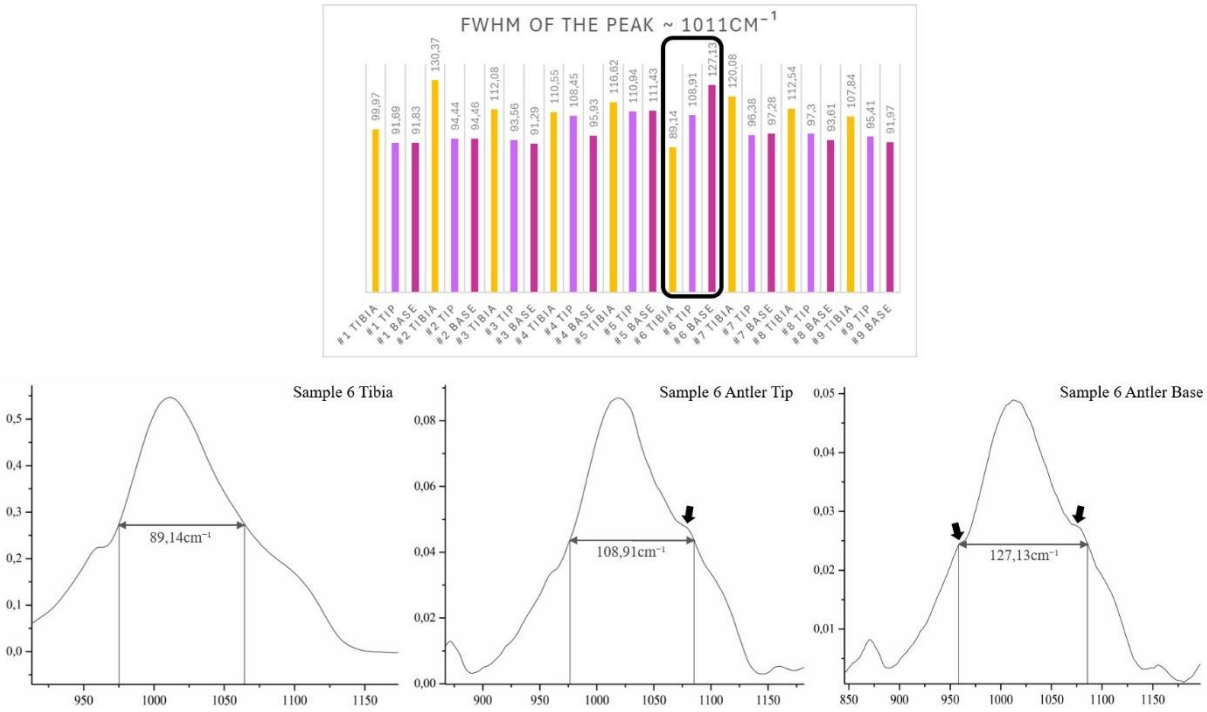

Figure 24. Individual comparison of the manually measured Full width at half maximum (FWHM) values of the FTIR peak at 1011cm^{-1}. Tibia has the greatest FWHM values across the samples, with one exception (sample #6). For this individual, the antler base has the largest FWHM. When examining the phosphate peaks in samples from this individual, it can be observed that the manually measured width in the antlers also extends to the side of possible subpeaks (black arrows). This extension is not visible in the other antler specimen, however, in contrast, the phenomenon occurs in the majority of other tibia samples analysed.

The lowest reciprocal value (1/FWHM) was obtained from tibia with a mean of 0.0091, while antler tip and base were observed to have slightly higher mean values, 0.0101 and 0.0102 respectively. A statistically significant overall effect ($p = 0.045$) was detected with the ANOVA, suggesting differences among the group means. However, the post hoc comparisons did not identify any specific pairwise differences as significant (Figure 25). This would suggest that while variability exists between these groups, it was not sufficient between any specific groups to reach significance after correction.

Another reported way to evaluate bioapatite crystallinity is to calculate the crystallinity index (CI)/infrared splitting factor (IRSF) by adding up the intensities of the peak at 604 cm^{-1} and the peak at 565 cm^{-1} and dividing the resulting sum by the intensity of the gap between these peaks. In this data, these peaks were located approximately at 598 cm^{-1} and 555 cm^{-1}. With this method, antler base had the lowest CI with the mean value of 3.14, whereas means for antler tip and tibia were 3.4519 and 3.5416. No significant difference was observed (ANOVA 0.369).

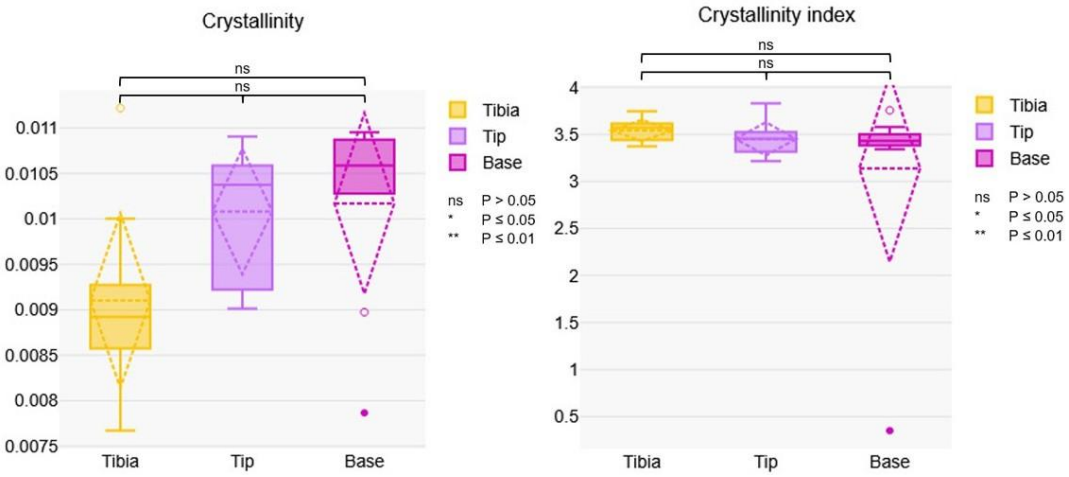

Figure 25. The degree of crystallinity derived from two different instrument analyses. No significant differences (ns) were observed regarding this parameter. The horizontal solid line in each box represents the median; horizontal dashed line presents the mean, and diamond shapes extending from that represent standard deviation; the box edges represent the interquartile range; whiskers extend to the minimum and maximum values; and the dots represent outliers.

Three carbonate-related parameters were examined to evaluate the carbonate incorporation: carbonate content of bioapatite (CO_3/PO_4 ratio), carbonate accumulation in the apatite crystal, and carbonate to mineral ratio (Figure 26). These values exhibited differing trends. Antler tip showed the greatest CO_3/PO_4 ratio (mean = 0.93), pointing to increased carbonate substitution in comparison to antler base (mean = 0.66) and tibia (mean = 0.59). This difference was statistically significant, both ANOVA and Tukey HSD being p = <0.001 between antler tip vs. antler base (mean difference = 0.27), and antler tip vs. tibia (mean difference = 0.34).

The carbonate to mineral ratio in tibia (mean = 0.081) was observed to be higher than in antlers. When compared to the antler tip region (mean = 0.076), there was no significant difference, the mean difference being 0.0048 with a p-value of 0.425. The difference between tibia and antler base was deemed to be significant (mean difference = 0.01085, p = 0.022).

Carbonate accumulation in the apatite crystal, however, was considerably greater in tibia (mean = 0.81) in contrast to antler tip (mean = 0.22) and antler base (mean = 0.38). The mean differences of tibia to antler tip and base were 0.598 and 0.436, respectfully, making the significance level as p = <0.001. In addition, the difference between antler tip and base were also noted to be significant (p = 0.04), although to a smaller extent than the relation of these to tibia.

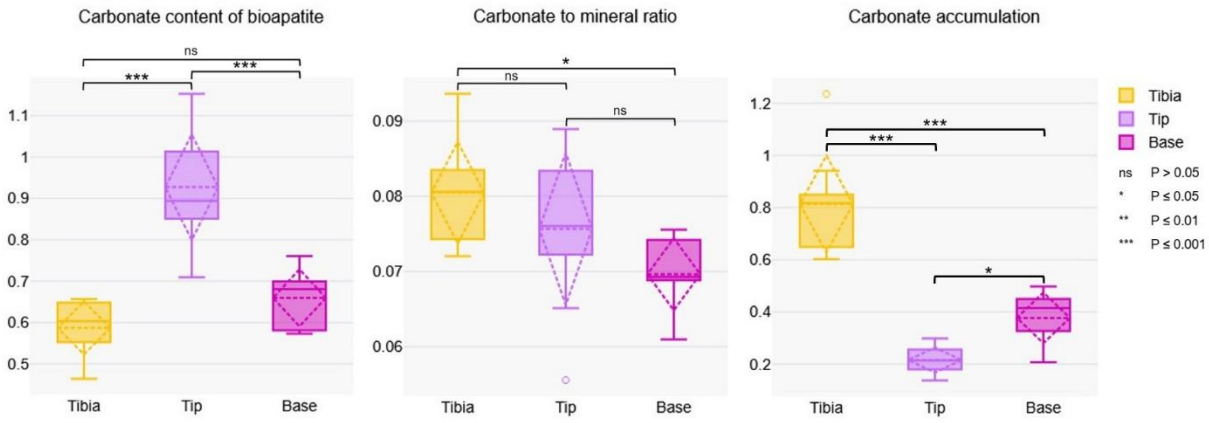

Figure 26. ATR-FTIR derived carbonate parameters. The horizontal solid line in each box represents the median; horizontal dashed line presents the mean, and diamond shapes extending from that represent standard deviation; the box edges represent the interquartile range; and whiskers extend to the minimum and maximum values. The statistical significance between groups determined with Tukey's HSD have been indicated by different asterisks above the boxes, where ns = not significant, * = $p \leq 0.05$, ** = $p \leq 0.01$, *** = $p \leq 0.001$.

Of the bone sample groups, tibia had the highest outcome in regard to secondary structure of proteins (mean = 4.60). The mean values of antler tip and antler base were calculated to be very similar, 3.28 and 3.22, respectively. The difference between tibia and antler regions was statistically proven to be significant, with ANOVA p-value being 0.008, while Tukey HSD between tibia and antler tip was p = 0.02, and p = 0.016 between tibia and antler base.

All the calculated amide parameters were found to follow a similar trend, the ratios being more prominent in antler tips. The significance between antler tip and tibia was always p = <0.001, whereas there was a minor variation between antler tip and antler base: Amides III + Collagen to phosphate parameter presented a significance of p = 0.039, while in the other amide parameters this varied slightly, but was always greater (Figure 27).

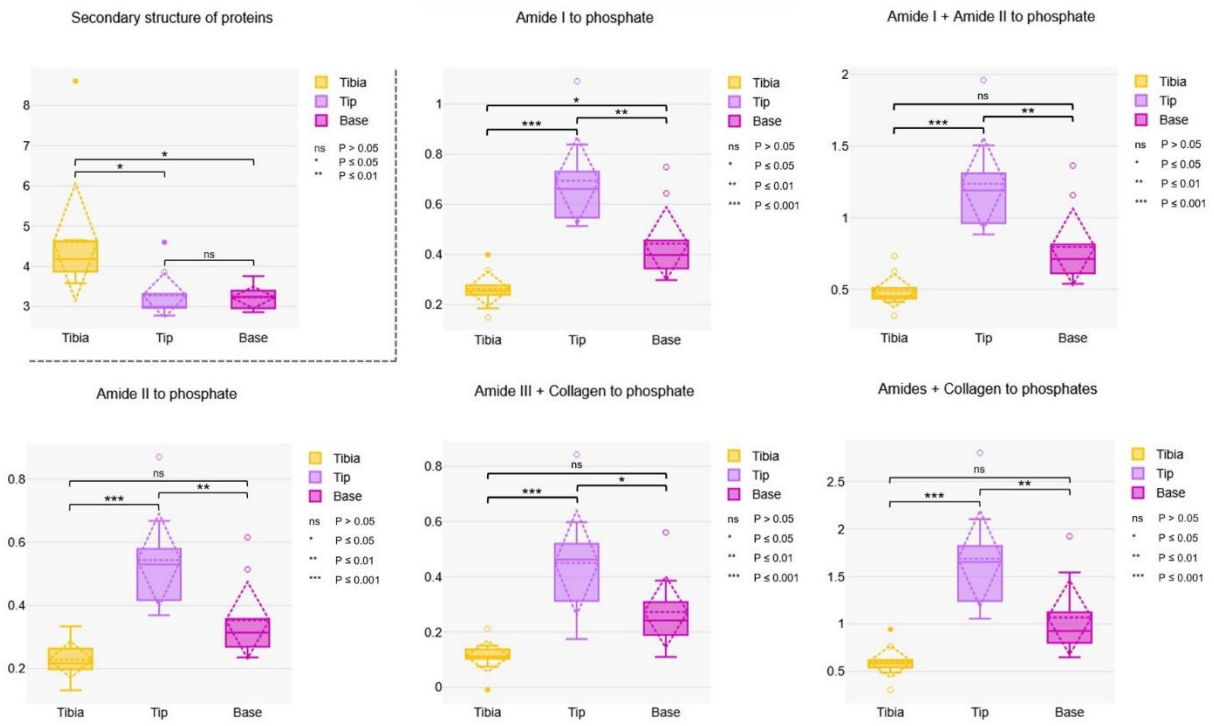

Figure 27. Box plots of secondary structure of proteins and amide contribution in reindeer antler and tibia. The horizontal solid line in each box represents the median; horizontal dashed line presents the mean, and diamond shapes extending from that represent standard deviation; the box edges represent the interquartile range; whiskers extend to the minimum and maximum values; and the dots represent outliers. The statistical significance between groups determined with Tukey's HSD have been indicated by different asterisks above the boxes, where ns = not significant, * = $p \leq 0.05$, ** = $p \leq 0.01$, *** = $p \leq 0.001$.

4.3 Micro-CT results

In order to examine the inter-individual variability in reindeer tibia, mean values across the four ROIs per individual were calculated (Table 10). For bone mineral density, the obtained values ranged from 0.91 to 1.13 g/cm^3, the mean value being 1.0007g/cm^3 with a standard deviation of 0.064. This suggests that bone mineral density (BMD) is consistent across the individuals involved. As in the evaluation of the tibia, average density values for antler were calculated by bone type by averaging the four selected ROIs for each individual. BMD was constantly lowest on the centre of the antler at both the tip and base. In antler base, densest values were always met in the intermediate region, whereas in antler tip, six out of nine samples exhibited this trend. The standard deviations in antler measurements were notably stronger compared to tibia, varying from 0.0651 to 0.1358 in antler base, and from 0.1338 up to 0.1822 in antler tip.

Table 10. Mean and standard deviation of bone mineral density (BMD) micro-CT parameter in each bone group (tibia, antler tip, antler base) and their regions, with ANOVA expressed as a between-groups value.

Bone mineral density	**BMD (g/cm³)**
Tibia	1.001 ± 0.064
Antler tip centre	0.348 ± 0.134
Antler tip intermediate	0.646 ± 0.182
Antler tip peripheral	0.645 ± 0.141
Antler base centre	0.376 ± 0.136
Antler base intermediate	0.807 ± 0.131
Antler base peripheral	0.663 ± 0.065
p (ANOVA)	< 0.001

The assessment of intra-bone variation was followed with inter-bone comparisons across the three bone types: tibia, antler base, and antler tip. Figure 28 exhibits the mean bone mineral density values for each bone type. Bone mineral density (BMD) varied noticeably among the different bone regions. The highest BMD (1.0007g/cm^3) was observed in tibia while the values in the antlers were lower overall. This difference was significant with ANOVA and Tukey's HSD being p = <0.001 between tibia and antler regions, the exception being the comparison of tibia and the intermediate region of the antler base, where Tukey's HSD was p = 0.034. Within the antlers, greater bone mineral density was expressed in the intermediate and peripheral regions compared to the centre, especially at the base. The average BMD within the antler tip increased from centre (0.3481g/cm^3) to intermediate region (0.6457g/cm^3), remaining relatively similar in the peripheral region (0.6449g/cm^3). Similarly, BMD in the antler base increased from the centre (0.3759g/cm^3) to the intermediate region (0.8070g/cm^3). Tukey's HSD revealed that antler tip had significantly lower BMD (p = <0.001) compared to the other regions of antler tip and base, except for the centre region of antler base. A similar trend was observed with the centre of the antler base, with significant differences (p = <0.001) with all but the centre of the antler tip. Interestingly, the intermediate region in the antler base was greater compared to the corresponding area of the antler tip, making its difference to the centre and peripheral region (0.6633g/cm^3) of the antler base more visible.

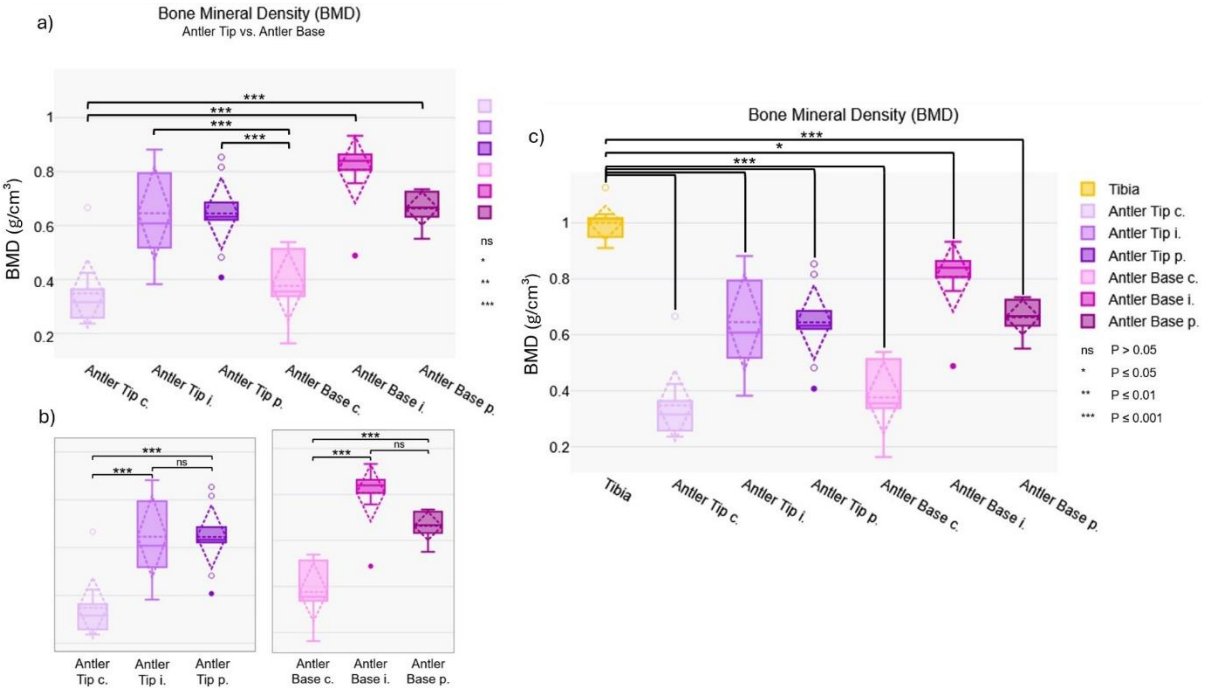

Figure 28. Bone mineral density values across reindeer tibia, antler tip, and antler base with their determined regions (c = centre, i = intermediate, p = peripheral). The statistical significance between bone groups and antler regions determined with Tukey's HSD have been indicated by different asterisks above the boxes, where ns = not significant, * = p ≤ 0.05, ** = p ≤ 0.01, *** = p ≤ 0.001. a) Density differences between the regions of antler tip and the regions of antler base (Tukey's HSD; p ≤ 0.001). b) Internal density differences between regions in antler tip and antler base. c) Bone density of the tibia compared to the bone density of the antler regions. The horizontal solid line in each box represents the median; horizontal dashed line presents the mean, and diamond shapes extending from that represent standard deviation; the box edges represent the interquartile range; whiskers extend to the minimum and maximum values; and the dots represent outliers.

Regarding porosity parameters, no significant differences were found between the bone groups (tibia, antler tip, antler base) in terms of closed porosity [Po(cl)]. ANOVA between groups was computed as 0.013; however, in Tukey's multiple comparisons, value only reached to p = 0.075, this relation being between the intermediate region of antler tip (mean = 0.1169%) and the centre of antler base (mean = 0.0064%) The highest Po(cl) percentage within the antler tip was observed in the intermediate region, whereas at the antler base, the sealed pores seemed to appear the most in the peripheral region. In both antler groups the lowest Po(cl) reading was met in the centre of the bone, 0.0319% at the antler tip and 0.0064% at the antler base, respectively. The closed porosity of the tibia (mean = 0.01%) appeared to be similar to these readings.

One-way ANOVA showed a significant difference (p = <0.001) between the groups in terms of open porosity [Po(op)] and total porosity [Po(tot)]. The centre of the antler tip and antler base had an alike mean percentage relative to each other, 48.77% and

46.83%, making them the bone sections with the highest porosity (Figure 29). These values appeared the same in both open and total porosity parameters; based on Tukey's post hoc test, the centre regions formed a homogeneous subgroup that differed significantly from all other determined bone groups (p = <0.001). Another significant relation was observed between these centre regions and tibia (p = <0.001), the latter which turned out to have the least porous structure [mean Po(Op) = 1.62%, mean Po(Tot) = 1.63%].

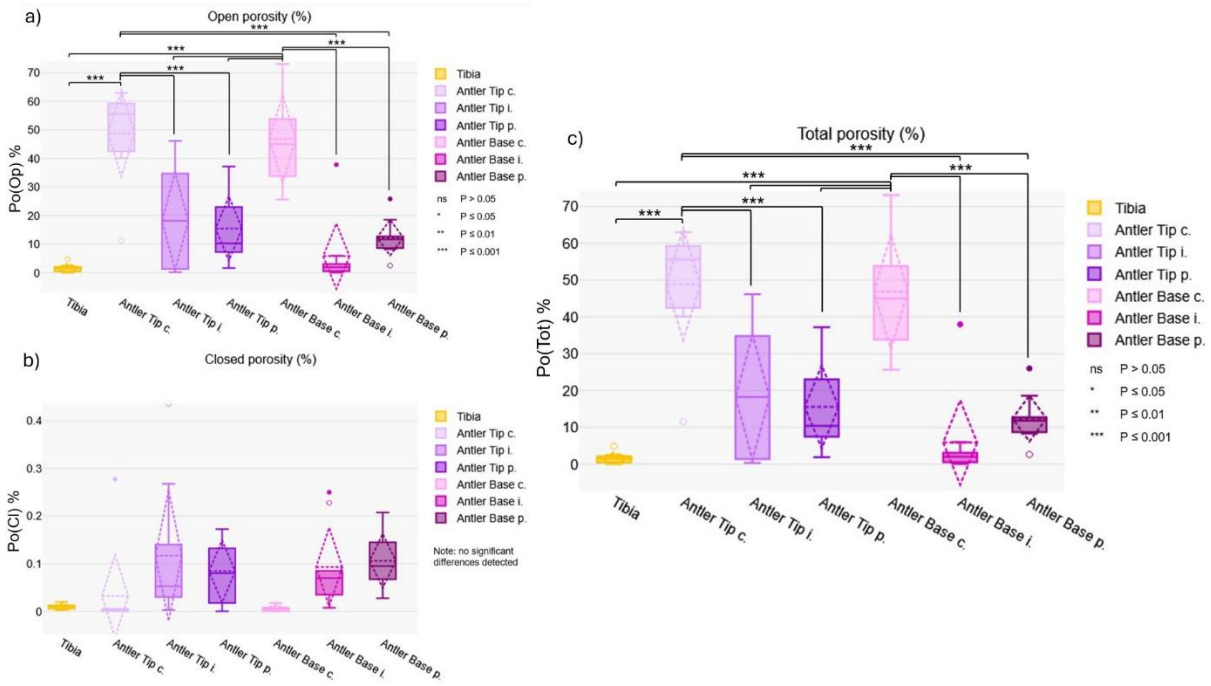

Figure 29. The distribution of different forms of a) open, b) closed, and c) total porosity in tibia and antler sampling regions. The statistical significance between bone groups and antler regions determined with Tukey's HSD have been indicated by different asterisks above the boxes, where ns = not significant, * = p ≤ 0.05, ** = p ≤ 0.01, *** = p ≤ 0.001. The horizontal solid line in each box represents the median; horizontal dashed line presents the mean, and diamond shapes extending from that represent standard deviation; the box edges represent the interquartile range; whiskers extend to the minimum and maximum values; and the dots represent outliers. c = centre, i = intermediate, p = peripheral.

The results of the intermediate region of antler tip showed the largest standard deviation in all porosity variables (Table 11), which would indicate that the variation between individuals is greater in this antler section compared to the other sections.

Table 11. Mean and standard deviation of micro-CT porosity parameters (closed, open, total) in each bone group (tibia, antler tip, antler base) and their regions, with ANOVA expressed as a between-groups value.

Porosity parameters	**Closed porosity (%)**	**Open porosity (%)**	**Total porosity (%)**
Tibia	0.010 ± 0.006	1.624 ± 1.479	1.635 ± 1.482

Porosity parameters	Closed porosity (%)	Open porosity (%)	Total porosity (%)
Antler tip centre	0.032 ± 0.092	48.77 ± 16.10	48.78 ± 16.02
Antler tip intermediate	0.117 ± 0.146	18.09 ± 18.12	18.21 ± 18.02
Antler tip peripheral	0.084 ± 0.069	15.47 ± 12.01	15.55 ± 11.95
Antler base centre	0.006 ± 0.069	46.86 ± 16.48	46.83 ± 16.48
Antler base intermediate	0.093 ± 0.088	7.778 ± 12.17	5.864 ± 12.19
Antler base peripheral	0.106 ± 0.060	12.29 ± 6.632	12.38 ± 6.626
p (ANOVA)	0.013	< 0.001	< 0.001

Antlers were evaluated for trabecular-specific properties. Bone volume fraction percentage (BV/TV) indicating the proportion of mineralized tissue was the greatest in the intermediate region of the antler base (94.14 ± 12.19%) and smallest in the centre of the antler tip (51.25 ± 16.02%). The values received from the centre of the antler base (53.17 ± 16.48%) were similar to the results of antler tip. ANOVA showed that the differences between groups were significant (p = <0.001). The relations between each group have been depicted in more detail in the Figure 30.

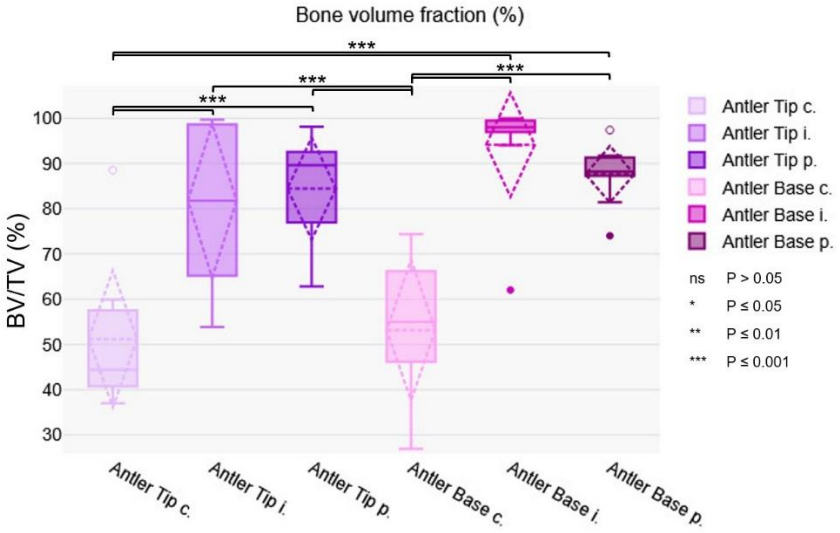

Figure 30. Micro-CT derived bone volume fraction in different antler regions. The statistical significance between antler groups and regions determined with Tukey's HSD have been indicated by different asterisks above the boxes, where ns = not significant, * = p ≤ 0.05, ** = p ≤ 0.01, *** = p ≤ 0.001.The horizontal solid line in each box represents the median; horizontal dashed line presents the mean, and diamond shapes extending from that represent standard deviation; the box edges represent the interquartile range; whiskers extend to the minimum and maximum values; and the dots represent outliers. c = centre, i = intermediate, p = peripheral.

No significant statistical difference in terms of trabecular number (Tb.N) between sample groups was spotted (ANOVA = 0.812). With both antler tip and antler base

samples, the centre region had the lowest and peripheral region the highest values in their own group. While the standard variation in antler tip regions ranged between 0.848mm/1 and 1.275mm/1, the variation in antler base regions was notably higher, fluctuating between 3.373mm/1 and 5.981mm/1 (Table 12).

Table 12. Mean and standard deviation of trabecular specific micro-CT parameters in each bone group (tibia, antler tip, antler base) and their regions, with ANOVA expressed as a between-groups value.

Trabecular specific parameters	**BV/TV**	**Tb.Th**	**Tb.Sp**	**Tb.N**
Antler tip centre	51.25 ± 16.02	0.090 ± 0.020	0.106 ± 0.026	5.614 ± 0.848
Antler tip intermediate	81.80 ± 18.02	0.154 ± 0.062	0.054 ± 0.034	5.688 ± 1.151
Antler tip peripheral	84.45 ± 11.95	0.149 ± 0.053	0.051 ± 0.019	6.069 ± 1.275
Antler base centre	53.17 ± 16.48	0.115 ± 0.037	0.152 ± 0.071	5.332 ± 3.373
Antler base intermediate	94.14 ± 12.19	0.206 ± 0.100	0.034 ± 0.029	6.663 ± 5.981
Antler base peripheral	87.62 ± 6.626	0.148 ± 0.057	0.050 ± 0.015	7.464 ± 5.038
p (ANOVA)	< 0.001	0.005	< 0.001	0.812

Based on Tukey's multiple comparisons, significant differences in trabecular thickness (Tb.Th) were observed between the intermediate region of the antler base and both the antler tip centre ($p = 0.002$) and antler base centre regions ($p = 0.026$), trabeculae being thicker in the intermediate region compared to centre regions. No statistically significant differences manifested between the other bone regions.

Trabecular separation (Tb.Sp), on the other hand, exhibited a greater significant variation between different regions of the antler (Figure 31). The centre region of the antler base stood out the most from other regions ($p = < 0.001$), indicating the largest distances between trabeculae. In contrast, trabecular spacing in the middle and outer regions of the antler base was significantly smaller compared to the centre region of the antler tip, p values of 0.002 and 0.026 respectively; this would suggest that the trabecular network becomes denser toward the periphery of the antler. A similar interpretation is supported by the result according to which trabeculae at the centre of the antler tip was significantly more dispersed compared to the outermost measured region ($p = 0.032$).

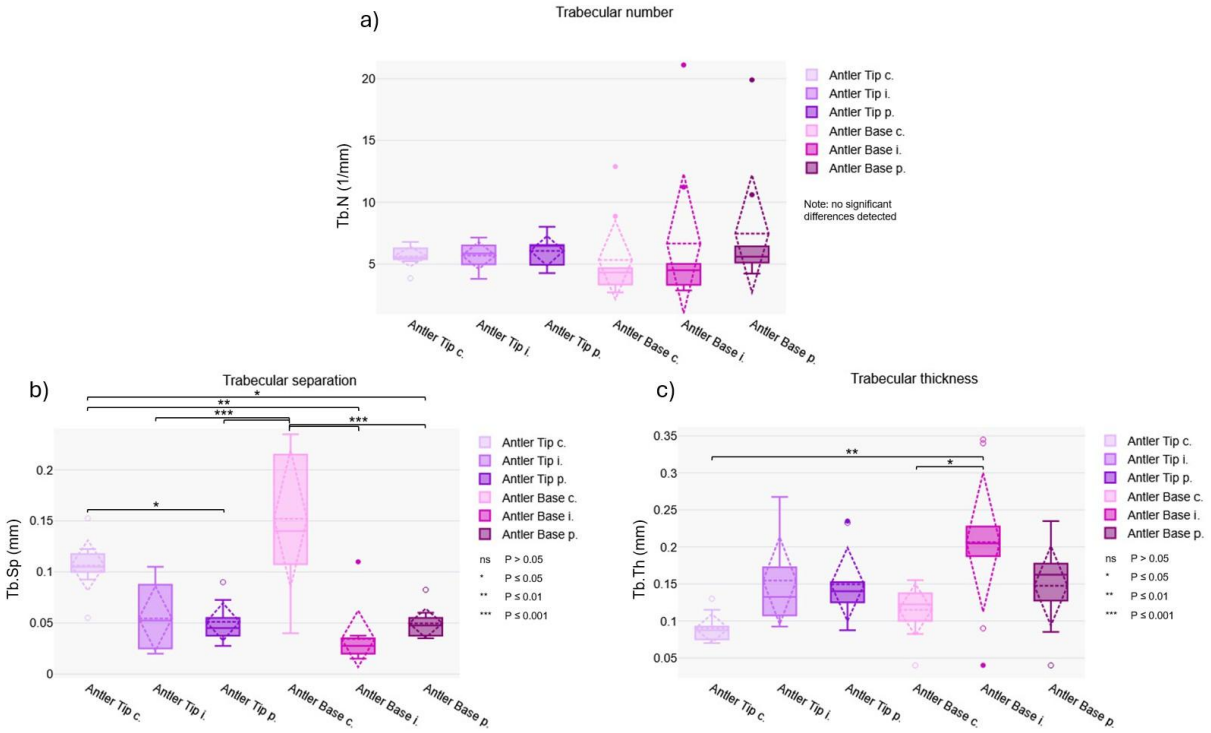

Figure 31. Trabecular-specific parameters including a) tb.number, b) tb.separation, and c) tb.thickness across antler samples. The statistical significance between antler groups and regions determined with Tukey's HSD have been indicated by different asterisks above the boxes, where ns = not significant, * = $p \leq 0.05$, ** = $p \leq 0.01$, *** = $p \leq 0.001$. The horizontal solid line in each box represents the median; horizontal dashed line presents the mean, and diamond shapes extending from that represent standard deviation; the box edges represent the interquartile range; whiskers extend to the minimum and maximum values; and the dots represent outliers. c = centre, i = intermediate, p = peripheral.

2D and 3D micro-CT images of the analysed samples are presented in Appendix 12 while the averages of the four ROIs by region for the parameters discussed in this section are listed for each individual in Appendix 13.

5 Discussion

This thesis used XRD and ATR-FTIR to assess the crystallographic and chemical compositional attributes of the bone material. In addition, the samples were scanned with a micro-CT system to examine the BMD, structural organization, and porosity of the samples.

The peaks observed on the obtained XRD patterns were identifiable with respect to the hydroxyapatite standard, suggesting that hydroxyapatite-like phase was present, and, from a technical point of view, that the data acquisition was successful. Mathematical fit functions can be applied to pure crystalline structures exhibiting well-defined peaks; however, bone mineral is known to contain separate apatite formation resulting in lower crystallinity, which makes the peaks more difficult to distinguish (Tadano and Giri, 2011). This was evident with phases where underlying peaks caused issues with peak fitting, hindering the quantitative analysis of that area. In the previous literature utilizing XRD technique for bone analysis (Farlay et al., 2010; Ou-Yang et al., 2001; Rao et al., 2017; Tadano and Giri, 2011; Taylor et al., 2021), the (0 0 2) peak has been generally recommended for quantitative analysis due to its sharper and more refined shape, reassuring that the analysis does not suffer from interference. Therefore, (0 0 2) was chosen as the main focus in order to minimise potential errors from less distinct peaks.

The statistical analysis of calculated crystallite size from XRD Peaks (0 0 2) and (0 0 4) showed that there was a significant difference in crystallite size between tibia and antler when derived from the (0 0 2) diffraction peak, tibial samples exhibiting larger mineral size. This conclusion, however, was not reached when evaluating the crystallite size from the (0 0 4) peak, as no significance was found. Both of these peaks are reflections of the c-axis of the apatite crystal structure; however, the peak located at (0 0 2) plane is concerned to correspond to higher intensity and occurs at a lower diffraction angle. The reason why the values calculated from the peak (0 0 4) did not yield significant differences between sample types may be due to the lower relative intensity of this peak, which in turn might have an effect on its sensitivity to size-related broadening. Given the earlier discussion on the challenge of peak fitting and the favouritism towards peak (0 0 2), it can probably be noted that the (0 0 2) reflection is more reliable for

evaluating crystallite size differences in this context, and that the observations made based on this approach likely reflect the actual biological differences in mineral growth between antler and tibia. The crystallite size in tibia appeared larger in the comparison made in this work which aligns with the commonly reported association between a greater hydroxyapatite mineral size and a more mature and stable bone (Mavrych et al., 2025). In this light, this observation may be interpreted to reflect differing developmental dynamics, where the remodelling of mineral phase is more prolonged in tibia compared to the rapid mineralization of antler.

To complement the insights on the crystalline characteristics, the present study assessed the molecular composition of the bone with ATR-FTIR spectroscopy. The mineral-matrix ratio was used to define the amount of mineral in relation to the amount of collagen present in the examined bone groups. The tibia possessed a higher mineral-to-matrix ratio compared to both antler regions. Therefore, this finding would indicate that a greater degree of mineralization has taken place in tibial bone. This is consistent with the view that mineralization is lower in a more recently developed bone in comparison to older tissue (Oftadeh et al., 2015). It is mentioned in the literature that the mineral-to-matrix ratio is considered to act as an indicator for bone mineral density (BMD) and tends to increase with age (Kourkoumelis et al., 2019). In the present study, micro-CT analysis revealed that the tibia has significantly higher bone mineral density compared to the antler, thus underlining the connection between these parameters obtained from two methods. The observed differences between the long bone and antler would seem to reflect the nature of tibia as a more mature and permanent bone compared to the seasonally regenerated antler tissue. Tibia was also observed to possess higher secondary structure of proteins and greater carbonate incorporation into the mineral phase (870 cm^{-1} / 1635 cm^{-1}), indicating more organised and mature collagen, which together with the results from XRD analysis of a larger crystal size, support the view of tibia as a more structurally developed bone. These findings also fit the narrative of tibia's structural role in load bearing; tibia as a dense and stiff bone is optimized for supporting the weight of the animal.

Lower mineral to matrix ratio and higher amide intensities in the antler tip, however, indicate that not only antler contains less mineral and more organic matrix compared to

tibia, but that these values may also reflect the differences in mineral profiles between antler regions. These findings concerning the composition patterns together with higher porosity noted in the antler tip aligns with previous publications, according to which calcium and phosphorus got reduced in the antler tip of red deer (*Cervus elaphus*) due to physiological exhaustion caused by rapid growth (Landete-Castillejos et al., 2007c), whereas with Iberian red deer (*Cervus elaphus hispanicus*), potassium and magnesium contents were higher in the top tine (Landete-Castillejos et al., 2007b).

The carbonate content of bioapatite (CO_3/PO_4 ratio) as well was found to be highest in the antler tip. This contradicts with previous literature stating how immature bone contains mineral with higher HPO_4^{2-} and lower CO_3^{2-} content (Mkukuma et al., 2004; Pang et al., 2020). According to Taylor and colleagues (2021), the change in mineral maturity/ crystallinity (MMC) is governed by the type and extent of carbonate substitution, the low carbonate content contributing to A-type and B-type substitution, while B-type substitution takes place in conditions where the carbonate content is higher. These present results would therefore suggest that the elevated CO_3/PO_4 ratio in antler represents its less crystallized nature, likely with the involvement of B-type substitution. Spatial variations in CO_3^{2-} content have been associated with both crystallinity and cellular activity in mineralized tissues where greater carbonate substitution has been reported to decrease hydroxyapatite (HA) crystallinity (Ou-Yang et al., 2001; Taylor et al., 2021). This view aligns with the FTIR and XRD findings from the current study showing how the reindeer tibia contains lower CO_3/PO_4 and higher crystallite size in comparison to the antler. Similarly, it seems that parallels can be drawn between the higher crystallite size in reindeer tibia and properties observed in archaeological human bones where crystallinity was reported to be greater in denser, cortical bones such as femurs and petrous bones in comparison to trabecular-rich tarsal bones (Leskovar et al., 2024). The elevated CO_3/PO_4 ratio observed on the tip of the antler may be an indicator of localized mineral turnover, thus showing parallels to trabecular-dominant human tarsals, which have been noted to possess proportionally higher carbonate concentrations with collagen sidebands in relation to cortical bones (Leskovar et al., 2024). In addition, Leskovar and colleagues (2024) reported the collagen concentrations and lower crystallinity to be the highest in infant femora.

Although any direct comparison cannot be done due to the differences between species and the unknown age of the reindeer individuals included in this current study, these properties of the immature human bone may be analogues to characteristics of the antler tip, given that it represents the youngest and most recently formed part of the antler.

In this work, open and total porosity were noted to be lowest in tibia, and highest at the centre of the antler compared to the rest of the evaluated antler regions. The differences in porosity are consistent with the formation mechanisms of antlers and tibia. Gomez and colleagues have described the development of antler cortex in red deer antlers as a process in which the initially formed porous trabecular scaffold of woven bone is incompletely filled with primary osteons due to time constraints, which, together with a decrease in the rate of mineral apposition in later stages of osteon formation, results in a more porous structure (Gomez et al., 2013). The structure of the tibia, in contrast, is denser and less porous, as longer remodelling allows for more complete osteonal filling.

The distribution of bone volume fraction (BV/TV), on the other hand, was observed to be highest in the intermediate region of the antler base and lowest in the central region of the tip. Furthermore, a regional microstructural differentiation in the antler base was noted: besides the higher BV/TV, the intermediate region also possessed greater trabecular thickness (Tb.Th), while the centre had the greatest trabecular separation (Tb.Sp) which fits with the observations of higher porosity in this region. While the current study used cut bone sections for the material analysis, some degree of comparison at the conceptual level with previous studies on graft materials can be discussed. Smaller hydroxyapatite grain sizes and significantly higher volumetric porosity have been reported in decellularized cancellous bone (DCB) of antler when compared to DCBs from human, bovine, and other deer sources, alongside observations of larger pore size, increased surface roughness, hydrophilicity, and levels of magnesium, silicon, and sulphur (Li et al., 2025). Greater surface roughness and variability observed in *Cervus elaphus* xenograft particles have been speculated to promote osteoblast adhesion and raise immune response (Mahboubian et al., 2024). When considering the particle variation in antler presented by Mahboubian and

colleagues, the findings made in this thesis can be viewed to support the idea that reindeer antler is regionally heterogeneous. Additionally, the enhanced osteogenic response can be seen to be consistent with the current notations of higher amide content and carbonate substitution in the reindeer antler tip; these features could be interpreted to point towards active, less mineralised tissue structure potentially supporting bone remodelling.

The presence of less mineralized tissue and lower mineral accumulation may partly reflect factors affecting mineral intake and accumulation. A decrease in tissue mineral content and alterations in cortical geometry due to vitamin D and calcium deficiency have been suggested to exhaust bone's capability to bear burdens directed towards it (Donnelly et al., 2010), these conditions also being associated with osteoporosis (Fischer et al., 2018; Voulgaridou et al., 2023). Given the high mineral demands of antler regeneration, such deficiencies could be seen to inhibit this process. However, the consistently lower mineral-to-matrix ratio in reindeer antler observed in the current study aligns with previously established biological distinction between permanent skeletal structures and antlers (Currey, 2003; Landete-Castillejos et al., 2019), demonstrating that despite their lower mineralization, the antlers had still reached their potential as functional structure. While the focus here was on the material characterisation, the observed differences may be connected to the possible adaptations taken place in the antler metabolism. Curiously, a previous genetic research on reindeer antlers identified species-specific mutations in two genes associated with enhanced vitamin D synthesis and utilization, implying that these changes may be in key role for providing adequate calcium needed for antler growth (Lin et al., 2019). Therefore, adaptation like this could shed light on how a relatively less mineralized tissue can maintain bone quality while being able to withstand mechanical stress during the rutting season. Observations on the relationship of optimized mineral metabolism to various bone functions could potentially be applied to conditions such as osteoporosis, where bone mineralization and remodelling are disrupted.

While these findings provide insights into the material differences between reindeer antler and tibia, the interpretation is subject to certain methodological limitations related to data acquisition and analysis, which need to be acknowledged. The first

limitation of this study focuses on the XRD analysis. The XRD quantification was attempted with peak fitting function of Origin software, however, this method was not completely successful for the entire diffractogram. Due to the overlapping apatite reflections, the software was unable to detect or resolve all subpeaks. Therefore, Origin was not necessarily the best option for processing the existing dataset. Secondly, some of the XRD measurements had significant background noise which made it difficult to do any kind of fitting with the data as it was. It was discussed that in the future studies of this kind, a longer measurement time and a lower resolution would be recommended in order to get a reliable fit from which a quantitative analysis, preferably conducted with the instrument's own software meant for diffraction data, could be performed.

The analyses for ATR-FTIR spectra were executed without normalization in consideration for the preservation of original intensity relations and the possible distortion caused to height ratios due to this procedure. Therefore, the performed comparisons between individuals and sample types represent proportional peak intensities instead of normalized area absorbance ratios. With this kind of methodological approach, differing sample thickness or baseline may introduce a bias, however, the preparation of the analysed samples followed the same conditions. The phosphate band at around 1011cm^{-1} underwent a manual determination of full width at half maximum (FWHM), which was needed for calculating the crystallinity parameter (1/FWHM). Defined in this manner, the presence of small sub-features was noted within the FWHM interval. Overlapping bands in the spectra denote a broadening of the examined interval, which in turn may skew the way the physical properties will be interpreted, in other words, the crystallinity values may appear lower than they truly are. Generally, the area ratio obtainment and exclusion of subpeaks have been dealt with the application of deconvolution and peak fitting techniques (Alebrahim et al., 2023; El-Hansi et al., 2021; Gardegaront et al., 2018; Gieroba et al., 2021; Kourkoumelis et al., 2019; Querido et al., 2018; Taylor et al., 2021). Another factor which should be taken into account is the choice of approach taken when determining parameters like these. Alongside splitting factor, 1030/1020 ratio has been applied in research (Alebrahim et al., 2023; Kimura-Suda and Ito, 2017; Kourkoumelis et al., 2019; Mata-Miranda et al., 2019; Taylor et al., 2021), however, it was not tested in this study and therefore it is not

possible to ascertain whether this sub-peak ratio would have made a difference to the results in comparison to results obtained by other ratios. It could also be noted that this ratio has been labelled as “not adequate” as well (Querido et al., 2018).

Finally, a dilemma with the variation of spectroscopy techniques exists. It has been argued that FTIR is more improved in mineral maturity determination, while Raman spectroscopic imaging is superior in crystallinity evaluation (Kimura-Suda and Ito, 2017). However, the opposite stance has been taken as well, stating that FT-IR has greater sensitivity to crystallinity compared to Raman (Taylor et al., 2021). Based on this study, it is not possible to comment on the effectiveness between these two techniques. This study used two different FTIR analysers, PerkinElmer Frontier IR and PerkinElmer Spectrum 100, in the latter of which the output data was obtained in transmittance form, which was then converted to absorption. The difference in the produced intensities between these two instruments was not assessed here, as the focus was on the internal parameter relationships of each measurement method.

Micro-CT morphometric parameters were obtained directly from the automatic ASBMR-standardized (The American Society for Bone and Mineral Research) analysis pipeline of the instrument without performing additional manual image-based segmentation or independent examination of the internal bone structure. While incorporating densitometry calibrated with hydroxyapatite phantoms, the lack of further image analysis needs to be addressed as a methodological limitation; variability dependent on the type of thresholding has been noted across the micromorphometric parameter results, the automated methods producing the most fluctuating outcomes (Buyuksungur et al., 2024).

The ROI dimensions applied for micro-CT analysis were not uniform inside and across the bone groups, therefore the influence of this variation on the results cannot be excluded. Considerable ranges were introduced in the tissue volume, the most notable one being between 205x205 and 87x87 pixels which corresponds to ~5.5-fold difference in sampled areas. In addition to the locations and sizes of the ROIs, the determined subdivision of the antler itself proved to be challenging when interpreting the results. The division of antler cross-sections into central, intermediate, and peripheral regions

was based on a benchmarking analysis composed on one representative individual prior to the whole micro-CT imaging series executed in this study. Based on the antler base sample, the porosity appeared to be greatest at the centre region, and lowest at the intermediate region. However, it was also revealed that there was no constant pattern across the antler since in the same individual's antler tip sample, the intermediate region was more porous than both the central and outer regions. Therefore, the regions defined in this study deviate from the classical differentiation into a central trabecular tissue, a trabecular-like transition zone, and an external compact tissue layer (Kierdorf et al., 2013; Lefebvre et al., 2016). The presence of an outer cortical zone has, however, been reported to vary depending on the part of the antler. More specifically, the presence of the cortical zone has only been noted in the lower parts of the antler while being absent in the upper parts and tines, which has been suggested to be due to the shorter formation time (Gomez et al., 2013).

Another limitation concerns the number of images inside VOI. While the intended depth of 51 slices could be applied to the majority of the samples (n = 16), exposure-related artefacts prevented this layer inclusion to the other portion of the samples (n = 11), therefore altering the total volume of bone analysis.

In this study, bone sections from tibia were taken from the diaphysis. Since this region contains primarily compact bone, evaluation of the trabecular bone properties was not performed in relation to antler. In hindsight, the focus of previous research involving the application of micro-CT has appeared to be firmly on the proximal tibia, where habitual loading (i.e. constant stress directed to the same anatomical area) has been noted to lead to trabecular adaptations, such as changes in trabecular bone volume fraction, thickness, and the degree of anisotropy, across species including mice (Sugiyama et al., 2010), pigs (Tanck et al., 2001), humans (Sun et al., 2021), and other primates (Lukova et al., 2025). An experimental study in sheep also reported similar adaptive sensitivity to altered loading in the distal end of tibia (Barak et al., 2011), although such research appears to be less common in relation to studies on proximal bone regions. The functional-adaptation studies covering artiodactyls such as deer, on the other hand, have utilized the calcaneus as an adaptation model (Sinclair et al., 2013; Skedros, 2025; Skedros et al., 2024, 2019, 2004). It has been speculated that the lack of large

mammals in trabecular bone modelling research is caused by the challenges to implement a modelling response that correlates with mobility in practice, as well as the number of resources needed to care for the animals and meet the requirements of animal welfare legislation (Barak, 2024).

Meaningful differences in antler properties such as modulus, toughness, and stiffness between sexes has yet to be established (Board et al., 2024; Shah et al., 2008). In this study, the sex of the studied individuals was not confirmed. Therefore, hypotheses and observations on whether prolonged antler retention in females might be associated with differences in mineral density, cortical structure, or collagen composition were not made. On the other hand, due to the sample size of this preliminary study, it would not have been possible to do any generalisations of the results.

6 Conclusions

This thesis demonstrates that there are noticeable differences in the structure and composition between rapidly formed antler tissue of reindeer and permanent, weight-bearing tibia. Greater mineral-to-matrix ratio and crystal size, as well as lower carbonate substitution resulting from the analyses performed with FTIR and XRD reflect tibia's role as a well mineralized structure adapted to endure mechanical loading. The characteristics of antler tissue, on the other hand, included lower mineral content and crystal size, together with elevated carbonate-to-phosphate ratios in the tip of the antler - traces of fast-phased growth and the mineral scarcity accompanied with it. Micro-CT analyses provide preliminary insights into the differences between antler and tibia, as well as heterogeneity within the antler. Greater bone mineral density and lower porosity of tibia are signs of maturation that has occurred at a slower pace supporting mechanical stability, while less dense and more porous structure of antler reflects growth strategy more optimised for a temporary functional role, where primary bone deposition is rapid, but maturation falls incomplete. The intermediate region of the antler base was found to possess the greatest proportion of mineralized tissue (BV/TV) and trabecular thickness, whereas the central region, particularly in the antler tip, had the largest porosity and trabecular separation. These observations seem to align with the antler maturation process; the development begins from the proximal part of the antler, offering the opportunity for more thorough mineralization, whereas the lastly developing distal end suffers from a higher mineral demand, resulting in more immature and carbonate-richer structure. All in all, it can be stated that these results support the prevailing understanding of the connection between growth period and mineral supply and the internal compositional and structural variation in antler. The results paint a picture where the antler and tibia are positioned at two extremes on the bone formation spectrum: rapid annual regeneration versus long-term stability, as reflected in the material properties of bone in terms of crystallinity, chemical composition, and microstructure.

7 Future Research Directions

Future research should include a larger sample size to verify the validity of the results obtained from this study and how they fit into a larger reindeer population. While variation in mineralization and microstructure was observed between antler regions and between tibia and antler, a larger sample would reflect natural variation within the species and thus serve as a more solid basis for ensuring real occurring differences. As previously discussed, inclusion of trabecular regions of the tibia would offer a broader perspective to its functional adaptations and provide a more straightforward comparison pair for the largely cancellous antler. It would also be ideal if the age of the individuals was included in the sample, as age can be indicative of the health of the individual. Furthermore, since reindeer are a unique species in that both sexes bear antlers with differing casting time, sex should be confirmed for each individual if comparison between male and female characteristics is desired. It could also be beneficial to contribute to the already commenced research trend on the effects of living environment and nutrition on *Cervidae* bone composition by conducting a material characterization using bones of both domesticated and wild reindeer. The evaluation on how different conditions and their effects are reflected in bone properties and overall wellbeing of reindeer would also serve herders and caretakers working with reindeer in captivity.

Incorporating both healthy and pathological (e.g. osteoporotic) representation would additionally enable a more profound overview of the differences between typical bone and bone with altered mineralization, and how the microstructural integrity is affected. In this study, one osteoporotic reference sample, taken from the base of the antler, was analysed alongside the samples examined. Regarding the microstructural and compositional values, there were some notable deviations from the rest of the dataset. In ATR-FTIR analysis, the osteoporosis antler base sample exhibited the largest mineral maturity (1011 cm^{-1}/1103 cm^{-1}), crystallinity (1 / FWHM of 1000 cm^{-1}), carbonate to mineral ratio, and secondary structure of proteins compared to other samples, whereas the Amide III + Collagen to phosphate value was the lowest. In the micro-CT analysis, it was observed that the BMD in the intermediate region of the osteoporosis sample had decreased. In addition, BV/TV and Tb.N were lower, while Tb.Sp was larger in

comparison to the whole sample. Region wise, open and total porosity were overall greater in the pathological sample. However, as a single sample is not representative on its own, further interpretation was outside the scope of this study, and therefore statistical comparison between the results was not included into this thesis.

Method wise, the primary focus in the future work should be on the standardization and optimization of data-acquisition parameters. For XRD, the scan speed and resolution should be evaluated further to achieve an optimal base for the data acquisition appropriate for Rietveld refinement. In the analysis phase of FTIR derived data, it is recommended to apply normalization procedures before further parameter evaluation. Finally, to ensure comparability across samples analysed with micro-CT and to enhance reproducibility, a uniform ROI size and layer number should be standardized if possible while considering the representation of each bone and their region. Histological validation and backscattered scanning electron (BSE) imaging could also assist in confirming the anatomical zoning of the antler, and the existence of cartilage remnants and demineralization defects.

Beyond these additions, other methodological directions could expand the possibilities of data gathering. Examining seasonal effects on mineral maturity and carbonate-phosphate substitution patterns by incorporating samples from different stages of the antler growth cycle could bring information about the degree of influence caused by the timing of antler growth and availability of the minerals. However, in terms of methodology, the question would be whether it is possible to gain samples from the same individual during the growth cycle, and if that is not feasible, would inter-individual research be beneficial. Longitudinal monitoring on the same individuals sets a challenge both logistically and ethically, the sampling intervals involving risks of infection or morphological alterations in the intact antlers. Therefore, if the goal is long-term monitoring to detect changes in the antlers, the future research could incorporate minimally invasive, in vivo alternatives such as portable X-ray fluorescence (pXRF) for determining the elemental composition of the antler surface or ultrasound to evaluate structural properties. Combining a micro-chemical technique would also enable an opportunity to distinguish the nature of ionic substitution patterns taking place and

provide insights about their relations with apatite crystal properties, maturation of the bone mineral, physiological exhaustion, and mechanical function.

8 Acknowledgements

I would like to express my gratitude to my supervisors Miho Nakamura and Pere Puigbò for giving me this opportunity to work on this topic, for their guidance and support in completing this thesis as well as in other various matters, and for the additional, well needed academic encouragement along the way. Working with them has been a positive and welcoming journey, an experience made possible by their kindness and openness. Many thanks to everyone involved in the Phylobone project and to all collaborators.

I would like to extend my appreciation to the academic personnel of the MSc Programme in Biomedical Imaging. They have built a great degree program, and I hope it will continue to flourish in the future, producing specialists in their chosen field. My special thanks go to Kari for acting as a teaching tutor; his active check-ups regarding well-being and progress in studies, and his willingness to help with questions and concerns made the study environment feel safe and supportive.

Finally, I am deeply grateful to my partner, my father, Helmiina, and my closest friends for their encouragement and support during the course of this thesis. Thank you for being on my team even in times when I don't believe in my own chances in the future.

This study was supported by the Sigrid Juselius Foundation, JSPS Grants-in-Aid for Scientific Research (JP23K08670), the Murata Foundation and the Turku Collegium for Science, Medicine and Technology. Thank you very much for your contributions to this research project.

References

Al-Qtaitat, A.I., Aldalaen, S.M., 2014. A Review of Non-Collagenous Proteins; their Role in Bone. AJLS 2, 351–355. https://doi.org/10.11648/j.ajls.20140206.14.

Alebrahim, M.A., Al-Akhras, M.-A.H., Al-Hiyasat, A.S., Ba Rajjash, A.S., Mousa, M.S., Al Darayseh, A., 2023. Microstructural Changes of Bone after Soft Tissue Removal: ATR-FTIR and XRD Spectroscopies. Journal of Spectroscopy 2023, 1–8. https://doi.org/10.1155/2023/6599002.

Ali, A., Chiang, Y.W., Santos, R.M., 2022. X-ray Diffraction Techniques for Mineral Characterization: A Review for Engineers of the Fundamentals, Applications, and Research Directions. Minerals 12, 205. https://doi.org/10.3390/min12020205.

Amirrah, I.N., Lokanathan, Y., Zulkiflee, I., Wee, M.F.M.R., Motta, A., Fauzi, M.B., 2022. A comprehensive review on collagen type I development of biomaterials for tissue engineering: from biosynthesis to bioscaffold. Biomedicines 10. https://doi.org/10.3390/biomedicines10092307.

Augusto de Castro, P.A., Dias, D.A., Del-Valle, M., Veloso, M.N., Ribeiro Somessari, E.S., Zezell, D.M., 2022. Assessment of bone dose response using ATR-FTIR spectroscopy: A potential method for biodosimetry. Spectrochim. Acta A Mol. Biomol. Spectrosc. 273, 120900. https://doi.org/10.1016/j.saa.2022.120900.

Baker, M.J., Trevisan, J., Bassan, P., Bhargava, R., Butler, H.J., Dorling, K.M., Fielden, P.R., Fogarty, S.W., Fullwood, N.J., Heys, K.A., Hughes, C., Lasch, P., Martin-Hirsch, P.L., Obinaju, B., Sockalingum, G.D., Sulé-Suso, J., Strong, R.J., Walsh, M.J., Wood, B.R., Gardner, P., Martin, F.L., 2014. Using Fourier transform IR spectroscopy to analyze biological materials. Nat. Protoc. 9, 1771–1791. https://doi.org/10.1038/nprot.2014.110.

Barak, M.M., Lieberman, D.E., Hublin, J.-J., 2011. A Wolff in sheep's clothing: trabecular bone adaptation in response to changes in joint loading orientation. Bone 49, 1141–1151. https://doi.org/10.1016/j.bone.2011.08.020.

Barak, M.M., 2024. Cortical and trabecular bone modeling and implications for bone functional adaptation in the mammalian tibia. Bioengineering (Basel) 11. https://doi.org/10.3390/bioengineering11050514.

Berendsen, A.D., Olsen, B.R., 2015. Bone development. Bone 80, 14–18. https://doi.org/10.1016/j.bone.2015.04.035.

Board, R., Sackett, E., Hangen, U., Jestine, J., Oyen, M., Johnston, R., 2024. Correlative Characterisation of Rangifer tarandus (Reindeer) Antler, Evaluating Differences Between Male, Female, and Calving Females. Microscopy and Microanalysis 30, ozae044.280.

Boerckel, J.D., Mason, D.E., McDermott, A.M., Alsberg, E., 2014. Microcomputed tomography: approaches and applications in bioengineering. Stem Cell Res. Ther. 5, 144. https://doi.org/10.1186/scrt534.

Boskey, A., 2003. Bone mineral crystal size. Osteoporos. Int. 14 Suppl 5, S16-20; discussion S20. https://doi.org/10.1007/s00198-003-1468-2.

Bubenik, G.A., Schams, D., White, R.J., Rowell, J., Blake, J., Bartos, L., 1997. Seasonal levels of reproductive hormones and their relationship to the antler cycle of male and female reindeer (Rangifer tarandus). Comp Biochem Physiol B, Biochem Mol Biol 116, 269–277. https://doi.org/10.1016/s0305-0491(97)00183-1.

Bubenik, G.A., 1990. The antler as a model in biomedical research, in: Bubenik, G.A., Bubenik, A.B. (Eds.), Horns, Pronghorns, and Antlers. Springer New York, New York, NY, pp. 474–487. https://doi.org/10.1007/978-1-4613-8966-8_19.

Buddhachat, K., Klinhom, S., Siengdee, P., Brown, J.L., Nomsiri, R., Kaewmong, P., Thitaram, C., Mahakkanukrauh, P., Nganvongpanit, K., 2016. Elemental Analysis of Bone, Teeth, Horn and Antler in Different Animal Species Using Non-Invasive Handheld X-Ray Fluorescence. PLoS ONE 11, e0155458. https://doi.org/10.1371/journal.pone.0155458.

Burr, D.B., 2002. The contribution of the organic matrix to bone's material properties. Bone 31, 8–11. https://doi.org/10.1016/s8756-3282(02)00815-3.

Buyuksungur, A., Szabó, B.T., Dobai, A., Orhan, K., 2024. The Effect of Micro-Computed Tomography Thresholding Methods on Bone Micromorphometric Analysis. J. Funct. Biomater. 15. https://doi.org/10.3390/jfb15110343.

Cañas-Gutiérrez, A., Arboleda-Toro, D., Monsalve-Vargas, T., Castro-Herazo, C., Meza-Meza, J.M., 2022. Techniques for bone assessment and characterization: porcine hard palate case study. Heliyon 8, e09626. https://doi.org/10.1016/j.heliyon.2022.e09626.

Cappelli, J., Atzori, A.S., Ceacero, F., Landete-Castillejos, T., Cannas, A., Gallego, L., García Díaz, A.J., 2017. Morphology, chemical composition, mechanical properties and structure in antler of Sardinian reddeer (Cervus elaphus corsicanus). Hystrix the Italian Journal of Mammalogy 28, 110–112.

Cappelli, J., Garcia, A., Ceacero, F., Gomez, S., Luna, S., Gallego, L., Gambin, P., Landete-Castillejos, T., 2015. Manganese Supplementation in Deer under Balanced Diet Increases Impact Energy and Contents in Minerals of Antler Bone Tissue. PLoS ONE 10, e0132738. https://doi.org/10.1371/journal.pone.0132738.

Ceacero, F., Pluháček, J., Landete-Castillejos, T., García, A.J., Gallego, L., 2015. Inter-Specific Differences in the Structure and Mechanics but not the Chemical Composition of Antlers in Three Deer Species. Ann. Zool. Fennici 52, 368–376. https://doi.org/10.5735/086.052.0501.

Chadefaux, C., Vignaud, C., Menu, M., Reiche, I., 2008. Effects and efficiency of consolidation treatments on Palaeolithic reindeer antler. Multi-analytical study by means of XRD, FT-IR microspectroscopy, SEM, TEM and μ-PIXE/PIGE analyses. Appl. Phys. A 92, 171–177. https://doi.org/10.1007/s00339-008-4469-3.

Chappard, D., 2022. Technical aspects, in: Bone Cancer. Elsevier, pp. 93–104. https://doi.org/10.1016/B978-0-12-821666-8.00053-0.

Chen, P.Y., Stokes, A.G., McKittrick, J., 2009. Comparison of the structure and mechanical properties of bovine femur bone and antler of the North American elk (Cervus elaphus canadensis). Acta Biomater. 5, 693–706. https://doi.org/10.1016/j.actbio.2008.09.011.

Clarke, B., 2008. Normal bone anatomy and physiology. Clin. J. Am. Soc. Nephrol. 3 Suppl 3, S131-9. https://doi.org/10.2215/CJN.04151206.

Coates, J., 2006. Interpretation of infrared spectra, A practical approach, in: Meyers, R.A. (Ed.), Encyclopedia of Analytical Chemistry: Applications, Theory and Instrumentation. John Wiley & Sons, Ltd, Chichester, UK. https://doi.org/10.1002/9780470027318.a5606.

Colmenares-Prado, M., Martínez Cortizas, A., Veiga-Rilo, C., López-Costas, O., 2025. Application of FTIR spectroscopy to infer ante- and post-mortem changes in

archaeological human bone. Spectrochim. Acta A Mol. Biomol. Spectrosc. 330, 125675. https://doi.org/10.1016/j.saa.2024.125675.

Currey, J D, Landete-Castillejos, T., Estevez, J., Ceacero, F., Olguin, A., Garcia, A., Gallego, L., 2009. The mechanical properties of red deer antler bone when used in fighting. J. Exp. Biol. 212, 3985–3993. https://doi.org/10.1242/jeb.032292.

Currey, John D., Landete-Castillejos, T., Estevez, J.A., Olguin, A., Garcia, A.J., Gallego, L., 2009. The Young's Modulus and Impact Energy Absorption of Wet and DryDeer Cortical Bone. The Open Bone Journal 1, 38–45.

Currey, J.D., 2003. The many adaptations of bone. J. Biomech. 36, 1487–1495. https://doi.org/10.1016/s0021-9290(03)00124-6.

Currey, J.D., 1988. The effect of porosity and mineral content on the Young's modulus of elasticity of compact bone. J. Biomech. 21, 131–139. https://doi.org/10.1016/0021-9290(88)90006-1.

Dal Sasso, G., Asscher, Y., Angelini, I., Nodari, L., Artioli, G., 2018. A universal curve of apatite crystallinity for the assessment of bone integrity and preservation. Sci. Rep. 8, 12025. https://doi.org/10.1038/s41598-018-30642-z.

Davison, K.S., Siminoski, K., Adachi, J.D., Hanley, D.A., Goltzman, D., Hodsman, A.B., Josse, R., Kaiser, S., Olszynski, W.P., Papaioannou, A., Ste-Marie, L.-G., Kendler, D.L., Tenenhouse, A., Brown, J.P., 2006. Bone strength: the whole is greater than the sum of its parts. Semin. Arthritis Rheum. 36, 22–31. https://doi.org/10.1016/j.semarthrit.2006.04.002.

Davis, E.B., Brakora, K.A., Lee, A.H., 2011. Evolution of ruminant headgear: a review. Proc. Biol. Sci. 278, 2857–2865. https://doi.org/10.1098/rspb.2011.0938.

DeMIGUEL, D., Azanza, B., Morales, J., 2014. Key innovations in ruminant evolution: a paleontological perspective. Integr. Zool. 9, 412–433. https://doi.org/10.1111/1749-4877.12080.

Donnelly, E., Chen, D.X., Boskey, A.L., Baker, S.P., van der Meulen, M.C.H., 2010. Contribution of mineral to bone structural behavior and tissue mechanical properties. Calcif. Tissue Int. 87, 450–460. https://doi.org/10.1007/s00223-010-9404-x.

El-Hansi, N.S., Said, H.H., Desouky, O.S., Khalaf, M.A., Talaat, M.S., Sallam, A.M., 2021. XRD and ATR-FTIR techniques for integrity assessment of gamma radiation

sterilized cortical bone pretreated by antioxidants. Cell Tissue Bank. 22, 305–321. https://doi.org/10.1007/s10561-020-09879-4.

Espmark, Y., 1964a. Rutting behaviour in reindeer (Rangifer tarandus L.). Animal Behaviour 12, 159–163. https://doi.org/10.1016/0003-3472(64)90117-4.

Espmark, Y., 1964b. Studies in dominance-subordination relationship in a group of semi-domestic reindeer (Rangifer tarandus L.). Animal Behaviour 12, 420–426. https://doi.org/10.1016/0003-3472(64)90061-2.

Estevez, J.A., Landete-Castillejos, T., Martínez, A., García, A.J., Ceacero, F., Gaspar-López, E., Calatayud, A., Gallego, L., 2009. Antler mineral composition of Iberian red deer Cervus elaphus hispanicus is related to mineral profile of diet. Acta Theriol. 54, 235–242. https://doi.org/10.4098/j.at.0001-7051.070.2008.

Fadlelmoula, A., Pinho, D., Carvalho, V.H., Catarino, S.O., Minas, G., 2022. Fourier Transform Infrared (FTIR) Spectroscopy to Analyse Human Blood over the Last 20 Years: A Review towards Lab-on-a-Chip Devices. Micromachines (Basel) 13. https://doi.org/10.3390/mi13020187.

Farlay, D., Panczer, G., Rey, C., Delmas, P.D., Boivin, G., 2010. Mineral maturity and crystallinity index are distinct characteristics of bone mineral. J. Bone Miner. Metab. 28, 433–445. https://doi.org/10.1007/s00774-009-0146-7.

Feng, X., McDonald, J.M., 2011. Disorders of bone remodeling. Annu. Rev. Pathol. 6, 121–145. https://doi.org/10.1146/annurev-pathol-011110-130203.

Feng, X., 2009. Chemical and Biochemical Basis of Cell-Bone Matrix Interaction in Health and Disease. Curr. Chem. Biol. 3, 189–196. https://doi.org/10.2174/187231309788166398.

Figueiredo, M.M., Gamelas, J.A.F., Martins, A.G., 2012. Characterization of Bone and Bone-Based Graft Materials Using FTIR Spectroscopy, in: Theophile, T. (Ed.), Infrared Spectroscopy - Life and Biomedical Sciences. InTech. https://doi.org/10.5772/36379.

Fischer, V., Haffner-Luntzer, M., Amling, M., Ignatius, A., 2018. Calcium and vitamin D in bone fracture healing and post-traumatic bone turnover. Eur. Cell. Mater. 35, 365–385. https://doi.org/10.22203/eCM.v035a25.

Flueck, W.T., Smith-Flueck, J.A.M., 2008. Age-independent osteopathology in skeletons of a South American cervid, the Patagonian huemul (Hippocamelus bisulcus). Journal of Wildlife Diseases 44, 636–648.

Fontcuberta-Rigo, M., Nakamura, M., Puigbò, P., 2023. Phylobone: a comprehensive database of bone extracellular matrix proteins in human and model organisms. Bone Res. 11, 44. https://doi.org/10.1038/s41413-023-00281-w.

France, C.A.M., Sugiyama, N., Aguayo, E., 2020. Establishing a preservation index for bone, dentin, and enamel bioapatite mineral using ATR-FTIR. Journal of Archaeological Science: Reports 33, 102551. https://doi.org/10.1016/j.jasrep.2020.102551.

Fratzl, P., Weinkamer, R., 2007. Nature's hierarchical materials. Prog. Mater. Sci. 52, 1263–1334. https://doi.org/10.1016/j.pmatsci.2007.06.001.

Gambín, P., Serrano, M.P., Gallego, L., García, A., Cappelli, J., Ceacero, F., Landete-Castillejos, T., 2017. Does Cu supplementation affect the mechanical and structural properties and mineral content of red deer antler bone tissue? Animal 11, 1312–1320. https://doi.org/10.1017/S1751731116002767.

Gao, Z., Yang, F., McMahon, C., Li, C., 2012. Mapping the morphogenetic potential of antler fields through deleting and transplanting subregions of antlerogenic periosteum in sika deer (Cervus nippon). J. Anat. 220, 131–143. https://doi.org/10.1111/j.1469-7580.2011.01457.x.

Gardegaront, M., Farlay, D., Peyruchaud, O., Follet, H., 2018. Automation of the peak fitting method in bone FTIR microspectroscopy spectrum analysis: human and mice bone study. Journal of Spectroscopy 2018, 1–11. https://doi.org/10.1155/2018/4131029.

Gieroba, B., Przekora, A., Kalisz, G., Kazimierczak, P., Song, C.L., Wojcik, M., Ginalska, G., Kazarian, S.G., Sroka-Bartnicka, A., 2021. Collagen maturity and mineralization in mesenchymal stem cells cultured on the hydroxyapatite-based bone scaffold analyzed by ATR-FTIR spectroscopic imaging. Mater. Sci. Eng. C Mater. Biol. Appl. 119, 111634. https://doi.org/10.1016/j.msec.2020.111634.

Goldman, L.W., 2007. Principles of CT and CT technology. J. Nucl. Med. Technol. 35, 115–28; quiz 129. https://doi.org/10.2967/jnmt.107.042978.

Gómez, J., Landete-Castillejos, T., García, A.J., Gaspar-López, E., Estevez, J.A., Gallego, L., 2008. Lactation growth influences mineral composition of first antler in Iberian red deer Cervus elaphus hispanicus. Wildlife Biol. 14, 331–338. https://doi.org/10.2981/0909-6396(2008)14[331:LGIMCO]2.0.CO;2.

Gomez, S., Garcia, A., Landete-Castillejos, T., Gallego, L., Pantelica, D., Pantelica, A., Preoteasa, E.A., Scafes, A., Straticiuc, M., 2016. Potential of the Bucharest 3 MV TandetronTM for IBA studies of deer antler mineralization. Nuclear Instruments and Methods in Physics Research Section B: Beam Interactions with Materials and Atoms 371, 413–418. https://doi.org/10.1016/j.nimb.2015.10.012.

Gomez, S., Garcia, A.J., Luna, S., Kierdorf, U., Kierdorf, H., Gallego, L., Landete-Castillejos, T., 2013. Labeling studies on cortical bone formation in the antlers of red deer (Cervus elaphus). Bone 52, 506–515. https://doi.org/10.1016/j.bone.2012.09.015.

González, A., 2012. 1.5 X-Ray Crystallography: Data Collection Strategies and Resources, in: Comprehensive Biophysics. Elsevier, pp. 64–91. https://doi.org/10.1016/B978-0-12-374920-8.00106-5.

Grace, N.D., Wilson, P.R., Nicol, A.M., 2003. The copper nutrition of grazing deer. NZGA R&P Series 9, 113–119. https://doi.org/10.33584/rps.9.2002.3410.

Hamed, E., Jasiuk, I., Yoo, A., Lee, Y., Liszka, T., 2012. Multi-scale modelling of elastic moduli of trabecular bone. J. R. Soc. Interface 9, 1654–1673. https://doi.org/10.1098/rsif.2011.0814.

Haraguchi, R., Kitazawa, R., Kohara, Y., Ikedo, A., Imai, Y., Kitazawa, S., 2019. Recent Insights into Long Bone Development: Central Role of Hedgehog Signaling Pathway in Regulating Growth Plate. Int. J. Mol. Sci. 20. https://doi.org/10.3390/ijms20235840.

Hart, N.H., Newton, R.U., Tan, J., Rantalainen, T., Chivers, P., Siafarikas, A., Nimphius, S., 2020. Biological basis of bone strength: anatomy, physiology and measurement. J. Musculoskelet. Neuronal Interact. 20, 347–371.

Hong, M.-H., Lee, J.H., Jung, H.S., Shin, Heungsoo, Shin, Hyunjung, 2022. Biomineralization of bone tissue: calcium phosphate-based inorganics in collagen fibrillar organic matrices. Biomater. Res. 26, 42. https://doi.org/10.1186/s40824-022-00288-0.

Høymork, A., Reimer, E., 2002. Antler development in reindeer in relation to age and sex. Rangifer 22, 75–82.

Jabłońska, M., Kramarczyk, M., Smieja-Król, B., Janeczek, J., 2016. Barium concentration in cast roe deer antlers related to air pollution caused by burning of barium-enriched coals in southern Poland. Environ. Sci. Pollut. Res. Int. 23, 5978–5982. https://doi.org/10.1007/s11356-016-6154-y.

Jacobsen, B.W., Colman, J.E., Reimers, E., 1998. The frequency of antlerless females among Svalbard reindeer. Rangifer 18, 81–84.

Kan, L., 2013. Animal Models of Bone Diseases-A, in: Animal Models for the Study of Human Disease. Elsevier, pp. 353–390. https://doi.org/10.1016/B978-0-12-415894-8.00016-6.

Kavan, J., Anděrová, V., 2019. Svalbard reindeer (Rangifer tarandus platyrhynchus) antler characteristics reflecting the local environmental conditions. Folia Oecologica 46, 16–23. https://doi.org/10.2478/foecol-2019-0003.

Kenkre, J.S., Bassett, J., 2018. The bone remodelling cycle. Ann. Clin. Biochem. 55, 308–327. https://doi.org/10.1177/0004563218759371.

Kierdorf, U., Flohr, S., Gomez, S., Landete-Castillejos, T., Kierdorf, H., 2013. The structure of pedicle and hard antler bone in the European roe deer (Capreolus capreolus): a light microscope and backscattered electron imaging study. J. Anat. 223, 364–384. https://doi.org/10.1111/joa.12091.

Kierdorf, U., Kierdorf, H., Szuwart, T., 2007. Deer antler regeneration: cells, concepts, and controversies. J. Morphol. 268, 726–738. https://doi.org/10.1002/jmor.10546.

Kierdorf, U., Kierdorf, H., 2005. Antlers as biomonitors of environmental pollution by lead and fluoride: A review. Eur. J. Wildl. Res. 51, 137–150. https://doi.org/10.1007/s10344-005-0093-0.

Kierdorf, U., Kierdorf, H., 2000. Delayed ectopic antler growth and formation of a double-head antler in the metacarpal region of a fallow buck (Dama dama L.) following transplantation of antlerogenic periosteum. Ann. Anat. 182, 365–370. https://doi.org/10.1016/S0940-9602(00)80013-8.

Kierdorf, U., Stock, S.R., Gomez, S., Antipova, O., Kierdorf, H., 2022. Distribution, structure, and mineralization of calcified cartilage remnants in hard antlers. Bone Rep. 16, 101571. https://doi.org/10.1016/j.bonr.2022.101571.

Kierdorf, U., Stoffels, E., Stoffels, D., Kierdorf, H., Szuwart, T., Clemen, G., 2003. Histological studies of bone formation during pedicle restoration and early antler regeneration in roe deer and fallow deer. Anat. Rec. A Discov. Mol. Cell. Evol. Biol. 273, 741–751. https://doi.org/10.1002/ar.a.10082.

Kieser, D.C., Kanade, S., Waddell, N.J., Kieser, J.A., Theis, J.-C., Swain, M.V., 2014. The deer femur--a morphological and biomechanical animal model of the human femur. Biomed Mater Eng 24, 1693–1703. https://doi.org/10.3233/BME-140981.

Kimura-Suda, H., Ito, T., 2017. Bone quality characteristics obtained by Fourier transform infrared and Raman spectroscopic imaging. Journal of Oral Biosciences 59, 142–145. https://doi.org/10.1016/j.job.2017.04.002.

Kourkoumelis, N., Tzaphlidou, M., 2010. Spectroscopic assessment of normal cortical bone: differences in relation to bone site and sex. ScientificWorldJournal 10, 402–412. https://doi.org/10.1100/tsw.2010.43.

Kourkoumelis, N., Zhang, X., Lin, Z., Wang, J., 2019. Fourier transform infrared spectroscopy of bone tissue: bone quality assessment in preclinical and clinical applications of osteoporosis and fragility fracture. Clin. Rev. Bone Miner. Metab. 17, 24–39. https://doi.org/10.1007/s12018-018-9255-y.

Krauss, S., Wagermaier, W., Estevez, J.A., Currey, J.D., Fratzl, P., 2011. Tubular frameworks guiding orderly bone formation in the antler of the red deer (Cervus elaphus). J. Struct. Biol. 175, 457–464. https://doi.org/10.1016/j.jsb.2011.06.005.

Landete-Castillejos, T., Currey, J.D., Ceacero, F., García, A.J., Gallego, L., Gomez, S., 2012. Does nutrition affect bone porosity and mineral tissue distribution in deer antlers? The relationship between histology, mechanical properties and mineral composition. Bone 50, 245–254. https://doi.org/10.1016/j.bone.2011.10.026.

Landete-Castillejos, T., Currey, J.D., Estevez, J.A., Fierro, Y., Calatayud, A., Ceacero, F., Garcia, A.J., Gallego, L., 2010. Do drastic weather effects on diet influence changes in chemical composition, mechanical properties and structure in deer antlers? Bone 47, 815–825. https://doi.org/10.1016/j.bone.2010.07.021.

Landete-Castillejos, T., Currey, J.D., Estevez, J.A., Gaspar-López, E., Garcia, A., Gallego, L., 2007a. Influence of physiological effort of growth and chemical composition on antler bone mechanical properties. Bone 41, 794–803. https://doi.org/10.1016/j.bone.2007.07.013.

Landete-Castillejos, T., Estevez, J.A., Martínez, A., Ceacero, F., Garcia, A., Gallego, L., 2007b. Does chemical composition of antler bone reflect the physiological effort made to grow it? Bone 40, 1095–1102. https://doi.org/10.1016/j.bone.2006.11.022.

Landete-Castillejos, T., Garcia, A., Gallego, L., 2007c. Body weight, early growth and antler size influence antler bone mineral composition of Iberian red deer (Cervus elaphus hispanicus). Bone 40, 230–235. https://doi.org/10.1016/j.bone.2006.07.009.

Landete-Castillejos, T., Kierdorf, H., Gomez, S., Luna, S., García, A.J., Cappelli, J., Pérez-Serrano, M., Pérez-Barbería, J., Gallego, L., Kierdorf, U., 2019. Antlers - Evolution, development, structure, composition, and biomechanics of an outstanding type of bone. Bone 128, 115046. https://doi.org/10.1016/j.bone.2019.115046.

Larkin, P., 2011. Instrumentation and sampling methods, in: Infrared and Raman Spectroscopy. Elsevier, pp. 27–54. https://doi.org/10.1016/B978-0-12-386984-5.10003-5.

Lefebvre, A., Rochefort, G.Y., Santos, F., Le Denmat, D., Salmon, B., Pétillon, J.-M., 2016. A Non-Destructive Method for Distinguishing Reindeer Antler (Rangifer tarandus) from Red Deer Antler (Cervus elaphus) Using X-Ray Micro-Tomography Coupled with SVM Classifiers. PLoS ONE 11, e0149658. https://doi.org/10.1371/journal.pone.0149658.

Leskovar, T., Jerman, I., Zupanič Pajnič, I., 2024. Unveiling intra-skeletal variability in mature and immature human skeletal remains via ATR-FTIR spectroscopy. Vib. Spectrosc. 132, 103688. https://doi.org/10.1016/j.vibspec.2024.103688.

Lindtner, R., Kampik, L., Putzer, D., Klosterhuber, M., Pallua, A.K., Streif, W., Schirmer, M., Degenhart, G., Arora, R., Pallua, J.D., 2025. Advancements in High-Resolution Computed Tomography: Revolutionising Bone Health Micro-Research. Bioengineering (Basel) 12. https://doi.org/10.3390/bioengineering12111189.

Lin, X., Patil, S., Gao, Y.-G., Qian, A., 2020. The bone extracellular matrix in bone formation and regeneration. Front. Pharmacol. 11, 757. https://doi.org/10.3389/fphar.2020.00757.

Li, C., Clark, D.E., Lord, E.A., Stanton, J.-A.L., Suttie, J.M., 2002. Sampling technique to discriminate the different tissue layers of growing antler tips for gene discovery. Anat. Rec. 268, 125–130. https://doi.org/10.1002/ar.10120.

Li, S., Yang, Y., Yu, B., Gao, Xueli, Gao, Xue, Nie, S., Qin, T., Hao, Y., Guo, L., Wu, H., Ma, T., Zheng, Y., Geng, D., Gao, J., Xue, B., Zhang, Y., Yang, S., Wei, Y., Xia, B., Luo, Z., Huang, J., 2025. A Novel Deer Antler-Inspired Bone Graft Triggers Rapid Bone Regeneration. Adv. Mater. 37, e2411571. https://doi.org/10.1002/adma.202411571.

Lin, Z., Chen, L., Chen, X., Zhong, Y., Yang, Yue, Xia, W., Liu, C., Zhu, W., Wang, H., Yan, B., Yang, Yifeng, Liu, X., Sternang Kvie, K., Røed, K.H., Wang, K., Xiao, W., Wei, H., Li, G., Heller, R., Gilbert, M.T.P., Li, Z., 2019. Biological adaptations in the Arctic cervid, the reindeer (Rangifer tarandus). Science 364. https://doi.org/10.1126/science.aav6312.

Lincoln, G.A., Tyler, N.J., 1994. Role of gonadal hormones in the regulation of the seasonal antler cycle in female reindeer, Rangifer tarandus. J. Reprod. Fertil. 101, 129–138. https://doi.org/10.1530/jrf.0.1010129.

López, J.M., 2024. Bone development and growth. Int. J. Mol. Sci. 25. https://doi.org/10.3390/ijms25126767.

Lukova, A., Bachmann, S., Synek, A., Pahr, D.H., Kilbourne, B., Dunmore, C.J., Kivell, T.L., Skinner, M.M., 2025. Trabecular architecture of the proximal tibia in extant hominids. American Journal of Biological Anthropology 187, e70084. https://doi.org/10.1002/ajpa.70084.

Mahboubian, M.H., Kadkhodazadeh, M., Amid, R., Moscowchi, A., 2024. Comparative assessment of the physical structure of antler and bovine bone substitutes: An in vitro study. J. Adv. Periodontol. Implant Dent. 16, 4–8. https://doi.org/10.34172/japid.2024.012.

Marks, S.C., Odgren, P.R., 2002. Structure and development of the skeleton, in: Principles of Bone Biology. Elsevier, pp. 3–15. https://doi.org/10.1016/B978-012098652-1.50103-7.

Markusson, E., Folstad, I., 1997. Reindeer antlers: visual indicators of individual quality? Oecologia 110, 501–507. https://doi.org/10.1007/s004420050186.

Martínez Cortizas, A., López-Costas, O., 2020. Linking structural and compositional changes in archaeological human bone collagen: an FTIR-ATR approach. Sci. Rep. 10, 17888. https://doi.org/10.1038/s41598-020-74993-y.

Mata-Miranda, M.M., Guerrero-Ruiz, M., Gonzalez-Fuentes, J.R., Hernandez-Toscano, C.M., Garcia-Andino, J.R., Sanchez-Brito, M., Vazquez-Zapien, G.J., 2019. Characterization of the biological fingerprint and identification of associated parameters in stress fractures by FTIR spectroscopy. Biomed Res. Int. 2019, 1241452. https://doi.org/10.1155/2019/1241452.

Mavrych, V., Bolgova, O., Abuzubida, A., 2025. Comparative X-ray Diffraction Analysis of the Hydroxyapatite Crystal Structure in Developing and Mature Lumbar Vertebrae. Cureus 17, e84669. https://doi.org/10.7759/cureus.84669.

McGee-Lawrence, M.E., Secreto, F.J., Syed, F.A., 2013. Animal Models of Bone Disease-B, in: Animal Models for the Study of Human Disease. Elsevier, pp. 391–417. https://doi.org/10.1016/B978-0-12-415894-8.00017-8.

Melnycky, N.A., Weladji, R.B., Holand, Ø., Nieminen, M., 2013. Scaling of antler size in reindeer (Rangifer tarandus): sexual dimorphism and variability in resource allocation. J. Mammal 94, 1371–1379. https://doi.org/10.1644/12-MAMM-A-282.1.

Meschaks, P., Nordkvist, M., 1962. On the sexual cycle in the reindeer male. Acta Vet. Scand. 3, 151–162. https://doi.org/10.1186/BF03547136.

Mikla, V.I., Mikla, V.V., 2014. Computed Tomography, in: Medical Imaging Technology. Elsevier, pp. 23–38. https://doi.org/10.1016/B978-0-12-417021-6.00002-2.

Miller, J.H., Druckenmiller, P., Bahn, V., 2013. Antlers on the Arctic Refuge: capturing multi-generational patterns of calving ground use from bones on the landscape. Proc. Biol. Sci. 280, 20130275. https://doi.org/10.1098/rspb.2013.0275.

Mkukuma, L.D., Skakle, J.M.S., Gibson, I.R., Imrie, C.T., Aspden, R.M., Hukins, D.W.L., 2004. Effect of the proportion of organic material in bone on thermal decomposition of bone mineral: an investigation of a variety of bones from different species using thermogravimetric analysis coupled to mass spectrometry, high-temperature X-ray diffraction, and Fourier transform infrared

spectroscopy. Calcif. Tissue Int. 75, 321–328. https://doi.org/10.1007/s00223-004-0199-5.

Mohamed, A.M., 2008. An overview of bone cells and their regulating factors of differentiation. Malays. J. Med. Sci. 15, 4–12.

Mohamed, M.A., Jaafar, J., Ismail, A.F., Othman, M.H.D., Rahman, M.A., 2017. Fourier transform infrared (FTIR) spectroscopy, in: Membrane Characterization. Elsevier, pp. 3–29. https://doi.org/10.1016/B978-0-444-63776-5.00001-2.

Mohamed, M.A., Mohd Hir, Z.A., Wan Mokthar, W.N.A., Osman, N.S., 2020. Features of metal oxide colloidal nanocrystal characterization, in: Colloidal Metal Oxide Nanoparticles. Elsevier, pp. 83–122. https://doi.org/10.1016/B978-0-12-813357-6.00008-5.

Morris, M.D., Finney, W.F., 2004. Recent developments in Raman and infrared spectroscopy and imaging of bone tissue. Journal of Spectroscopy 18, 155–159. https://doi.org/10.1155/2004/765753.

Movasaghi, Z., Rehman, S., ur Rehman, Dr.I., 2008. Fourier Transform Infrared (FTIR) Spectroscopy of Biological Tissues. Applied Spectroscopy Reviews 43, 134–179. https://doi.org/10.1080/05704920701829043.

Nagy, S., Lindeberg, H., Nikitkina, E., Krutikova, A., Smith, E., Kumpula, J., Holand, Ø., 2021. Reproduction of male reindeer (Rangifer tarandus). Anim. Reprod. Sci. 227, 106722. https://doi.org/10.1016/j.anireprosci.2021.106722.

Nandiyanto, A.B.D., Oktiani, R., Ragadhita, R., 2019. How to read and interpret FTIR spectroscope of organic material. IJOST 4, 97. https://doi.org/10.17509/ijost.v4i1.15806.

Nasoori, A., 2020. Formation, structure, and function of extra-skeletal bones in mammals. Biol. Rev. Camb. Philos. Soc. 95, 986–1019. https://doi.org/10.1111/brv.12597.

Nieminen, M., 2017. Röntgensäteilyyn perustuvat menetelmät, in: Blanco Sequeiros, R., Koskinen, S., Aronen, H., Lundbom, N., Vanninen, R., Tervonen, O. (Eds.), Kliininen Radiologia. Kustannus Oy Duodecim.

Niinimäki, S., Härkönen, L., Puolakka, H.-L., van den Berg, M., Salmi, A.-K., 2021. Cross-sectional properties of reindeer long bones and metapodials allow identification

of activity patterns. Archaeol. Anthropol. Sci. 13, 146. https://doi.org/10.1007/s12520-021-01337-w.

Nobakhti, S., Shefelbine, S.J., 2018. On the relation of bone mineral density and the elastic modulus in healthy and pathologic bone. Curr. Osteoporos. Rep. 16, 404–410. https://doi.org/10.1007/s11914-018-0449-5.

Nowicka, W., Machoy, Z., Gutowska, I., Noceń, I., 2006. Contents of calcium, magnesium, and phosphorus in antlers and cranial bones of the European red deer (Cervus elaphus) from different regions in Western .... Polish Journal of ....

Obata, Y., Bale, H.A., Barnard, H.S., Parkinson, D.Y., Alliston, T., Acevedo, C., 2020. Quantitative and qualitative bone imaging: A review of synchrotron radiation microtomography analysis in bone research. J. Mech. Behav. Biomed. Mater. 110, 103887. https://doi.org/10.1016/j.jmbbm.2020.103887.

Oftadeh, R., Perez-Viloria, M., Villa-Camacho, J.C., Vaziri, A., Nazarian, A., 2015. Biomechanics and mechanobiology of trabecular bone: a review. J. Biomech. Eng. 137, 0108021–01080215. https://doi.org/10.1115/1.4029176.

Ou-Yang, H., Paschalis, E.P., Mayo, W.E., Boskey, A.L., Mendelsohn, R., 2001. Infrared microscopic imaging of bone: spatial distribution of CO3(2-). J. Bone Miner. Res. 16, 893–900. https://doi.org/10.1359/jbmr.2001.16.5.893.

Palmer, L.C., Newcomb, C.J., Kaltz, S.R., Spoerke, E.D., Stupp, S.I., 2008. Biomimetic systems for hydroxyapatite mineralization inspired by bone and enamel. Chem. Rev. 108, 4754–4783. https://doi.org/10.1021/cr8004422.

Pang, S., Su, F.Y., McKittrick, J., Jasiuk, I., 2020. Deproteinized young bone reveals a continuous mineral phase and its contribution to mechanical properties with age. Journal of Materials Research and Technology 9, 15421–15432. https://doi.org/10.1016/j.jmrt.2020.11.001.

Paschalis, E.P., Gamsjaeger, S., Klaushofer, K., 2017. Vibrational spectroscopic techniques to assess bone quality. Osteoporos. Int. 28, 2275–2291. https://doi.org/10.1007/s00198-017-4019-y.

Paschalis, E.P., Mendelsohn, R., Boskey, A.L., 2011. Infrared assessment of bone quality: a review. Clin. Orthop. Relat. Res. 469, 2170–2178. https://doi.org/10.1007/s11999-010-1751-4.

Pathak, N.N., Pattanaik, A.K., Patra, R.C., Arora, B.M., 2001. Mineral composition of antlers of three deer species reared in captivity. Small Ruminant Research 42, 61–65. https://doi.org/10.1016/S0921-4488(01)00218-8.

Pearson, O.M., Lieberman, D.E., 2004. The aging of Wolff's "law": ontogeny and responses to mechanical loading in cortical bone. Am. J. Phys. Anthropol. Suppl 39, 63–99. https://doi.org/10.1002/ajpa.20155.

Pekkarinen, A.-J., Rasmus, S., Kumpula, J., Tahvonen, O., 2023. Winter condition variability decreases the economic sustainability of reindeer husbandry. Ecol. Appl. 33, e2719. https://doi.org/10.1002/eap.2719.

Pelletier, M., Kotiaho, A., Niinimäki, S., Salmi, A.-K., 2020. Identifying early stages of reindeer domestication in the archaeological record: a 3D morphological investigation on forelimb bones of modern populations from Fennoscandia. Archaeol. Anthropol. Sci. 12, 169. https://doi.org/10.1007/s12520-020-01123-0.

Picavet, P.P., Balligand, M., 2016. Organic and mechanical properties of Cervidae antlers: a review. Vet. Res. Commun. 40, 141–147. https://doi.org/10.1007/s11259-016-9663-8.

Prasanna, L.C., Bothra, Y.S., Ramakrishna Bhat, K.M., Managuli, V., 2025. Exploring the bone tissue: Instrumental methods for characterization and biomedical research application. Translational Research in Anatomy 38, 100374. https://doi.org/10.1016/j.tria.2024.100374.

Price, J.S., Allen, S., Faucheux, C., Althnaian, T., Mount, J.G., 2005. Deer antlers: a zoological curiosity or the key to understanding organ regeneration in mammals? J. Anat. 207, 603–618. https://doi.org/10.1111/j.1469-7580.2005.00478.x.

Purdey, M., 2004. Elevated silver, barium and strontium in antlers, vegetation and soils sourced from CWD cluster areas: do Ag/Ba/Sr piezoelectric crystals represent the transmissible pathogenic agent in TSEs? Med. Hypotheses 63, 211–225. https://doi.org/10.1016/j.mehy.2004.02.041.

Pynn, R., 2009. Neutron Scattering—A Non-destructive Microscope for Seeing Inside Matter, in: Liang, L., Rinaldi, R., Schober, H. (Eds.), Neutron Applications in Earth, Energy and Environmental Sciences, Neutron Scattering Applications and Techniques. Springer US, Boston, MA, pp. 15–36. https://doi.org/10.1007/978-0-387-09416-8_2.

Querido, W., Ailavajhala, R., Padalkar, M., Pleshko, N., 2018. Validated Approaches for Quantification of Bone Mineral Crystallinity Using Transmission Fourier Transform Infrared (FT-IR), Attenuated Total Reflection (ATR) FT-IR, and Raman Spectroscopy. Appl. Spectrosc. 72, 1581–1593. https://doi.org/10.1177/0003702818789165.

Raisz, L.G., 2005. Bone biology: bone structure and remodeling, in: Bone Disease of Organ Transplantation. Elsevier, pp. 31–45. https://doi.org/10.1016/B978-012183502-6/50003-1.

Rao, D.V., Gigante, G.E., Cesareo, R., Brunetti, A., Schiavon, N., Akatsuka, T., Yuasa, T., Takeda, T., 2017. Synchrotron-based XRD from rat bone of different age groups. Mater. Sci. Eng. C Mater. Biol. Appl. 74, 207–218. https://doi.org/10.1016/j.msec.2016.11.136.

Reilly, R.M., 2019. X-Ray, CT and Mammography Technology, in: Reilly, R.M. (Ed.), Medical Imaging for Health Professionals: Technologies Andclinical Applications. John Wiley & Sons, Incorporated, USA, pp. 16–22.

Salhotra, A., Shah, H.N., Levi, B., Longaker, M.T., 2020. Mechanisms of bone development and repair. Nat. Rev. Mol. Cell Biol. 21, 696–711. https://doi.org/10.1038/s41580-020-00279-w.

Salmi, A.-K., Niinimäki, S., 2021. Reindeer Physical Activity Patterns and Reconstruction of Feeding Behaviour: Implications for Reindeer Domestication and Human-Reindeer Interaction, in: Salmi, A.-K., Niinimäki, S. (Eds.), Archaeologies of Animal Movement. Animals on the Move, Themes in Contemporary Archaeology. Springer International Publishing, Cham, pp. 45–57. https://doi.org/10.1007/978-3-030-68744-1_5.

Sánchez-Reverté, A., Fontcuberta-Rigo, M., Nakamura, M., Puigbò, P., 2024. Use of the Phylobone database for the annotation of bone extracellular matrix proteins in reindeer (Rangifer tarandus). Sci. Prog. 107, 368504241244666. https://doi.org/10.1177/00368504241244666.

Shah, S.R., DesJardins, J.D., Blob, R.W., 2008. Antler stiffness in caribou (Rangifer tarandus): testing variation in bone material properties between males and females. Zoology (Jena) 111, 476–482. https://doi.org/10.1016/j.zool.2007.12.001.

Sharma, A., Ojha, S., Shelke, A., Habib, A., 2025. Scanning acoustic microscopy for biomechanical characterization of reindeer antler using singular spectral analysis. Bone 196, 117475. https://doi.org/10.1016/j.bone.2025.117475.

Shim, J., Iwaya, C., Ambrose, C.G., Suzuki, A., Iwata, J., 2022. Micro-computed tomography assessment of bone structure in aging mice. Sci. Rep. 12, 8117. https://doi.org/10.1038/s41598-022-11965-4.

Siali, C., Niinimäki, S., Harvati, K., Karakostis, F.A., 2024. Reconstructing patterns of domestication in reindeer using 3D muscle attachment areas. Archaeol. Anthropol. Sci. 16, 19. https://doi.org/10.1007/s12520-023-01910-5.

Sinclair, K.D., Farnsworth, R.W., Pham, T.X., Knight, A.N., Bloebaum, R.D., Skedros, J.G., 2013. The artiodactyl calcaneus as a potential “control bone” cautions against simple interpretations of trabecular bone adaptation in the anthropoid femoral neck. J. Hum. Evol. 64, 366–379. https://doi.org/10.1016/j.jhevol.2013.01.003.

Skedros, J.G., Dayton, M.R., Bloebaum, R.D., Bachus, K.N., Cronin, J.T., 2024. Strain-mode-specific mechanical testing and the interpretation of bone adaptation in the deer calcaneus. J. Anat. 244, 411–423. https://doi.org/10.1111/joa.13971.

Skedros, J.G., Hunt, K.J., Bloebaum, R.D., 2004. Relationships of loading history and structural and material characteristics of bone: development of the mule deer calcaneus. J. Morphol. 259, 281–307. https://doi.org/10.1002/jmor.10167.

Skedros, J.G., Keenan, K.E., Cooper, D.M.L., Bloebaum, R.D., 2014. Histocompositional organization and toughening mechanisms in antler. J. Struct. Biol. 187, 129–148. https://doi.org/10.1016/j.jsb.2014.06.004.

Skedros, J.G., Su, S.C., Knight, A.N., Bloebaum, R.D., Bachus, K.N., 2019. Advancing the deer calcaneus model for bone adaptation studies: ex vivo strains obtained after transecting the tension members suggest an unrecognized important role for shear strains. J. Anat. 234, 66–82. https://doi.org/10.1111/joa.12905.

Skedros, J.G., 2025. A 50-year perspective on the use and potential of artiodactyl calcanei in bone adaptation studies. Biol. Rev. Camb. Philos. Soc. https://doi.org/10.1111/brv.70089.

Skuterud, L., Gwynn, J.P., Gaare, E., Steinnes, E., Hove, K., 2005. (90)Sr, (210)Po and (210)Pb in lichen and reindeer in Norway. J. Environ. Radioact. 84, 441–456. https://doi.org/10.1016/j.jenvrad.2005.04.016.

Šromová, V., Sobola, D., Kaspar, P., 2023. A brief review of bone cell function and importance. Cells 12. https://doi.org/10.3390/cells12212576.

Stani, C., Vaccari, L., Mitri, E., Birarda, G., 2020. FTIR investigation of the secondary structure of type I collagen: New insight into the amide III band. Spectrochim. Acta A Mol. Biomol. Spectrosc. 229, 118006. https://doi.org/10.1016/j.saa.2019.118006.

Steiner-Bogdaszewska, Ż., Tajchman, K., Ukalska-Jaruga, A., Florek, M., Pecio, M., 2022. The mineral composition of bone marrow, plasma, bones and the first antlers of farmed fallow deer. Animals (Basel) 12. https://doi.org/10.3390/ani12202764.

Subramanian, A., Rodriguez-Saona, L., 2009. Fourier transform infrared (FTIR) spectroscopy, in: Infrared Spectroscopy for Food Quality Analysis and Control. Elsevier, pp. 145–178. https://doi.org/10.1016/B978-0-12-374136-3.00007-9.

Sugiyama, T., Price, J.S., Lanyon, L.E., 2010. Functional adaptation to mechanical loading in both cortical and cancellous bone is controlled locally and is confined to the loaded bones. Bone 46, 314–321. https://doi.org/10.1016/j.bone.2009.08.054.

Sun, S.-Z., Jiang, W.-B., Song, T.-W., Chi, Y.-Y., Xu, Q., Liu, C., Tang, W., Xu, F., Zhou, J.-X., Yu, S.-B., Sui, H.-J., 2021. Architecture of the cancellous bone in human proximal tibia based on P45 sectional plastinated specimens. Surg. Radiol. Anat. 43, 2055–2069. https://doi.org/10.1007/s00276-021-02826-2.

Tadano, S., Giri, B., 2011. X-ray diffraction as a promising tool to characterize bone nanocomposites. Sci. Technol. Adv. Mater. 12, 064708. https://doi.org/10.1088/1468-6996/12/6/064708.

Tajchman, K., Bogdaszewski, M., Kowalczuk-Vasilev, E., 2020a. Effects of supplementation with different levels of calcium and phosphorus on mineral content of first antler, bone, muscle, and liver of farmed fallow deer (Dama dama). Can. J. Anim. Sci. 100, 17–26. https://doi.org/10.1139/cjas-2018-0234.

Tajchman, K., Muszyński, S., Ceacero, F., Kasperek, K., Janiszewski, P., Dziki-Michalska, K., Tomaszewska, E., 2025. Mechanical properties of farmed fallow deer antlers

depending on age. BMC Vet. Res. 21, 656. https://doi.org/10.1186/s12917-025-05123-x.

Tajchman, K., Ukalska-Jaruga, A., Bogdaszewski, M., Pecio, M., Dziki-Michalska, K., 2020b. Accumulation of Toxic Elements in Bone and Bone Marrow of Deer Living in Various Ecosystems. A Case Study of Farmed and Wild-Living Deer. Animals (Basel) 10. https://doi.org/10.3390/ani10112151.

Tajchman, K., Ukalska-Jaruga, A., Ceacero, F., Janiszewski, P., Pecio, M., 2023. Concentration of potentially toxic elements in farmed fallow deer antlers depending on diet and age. Animals (Basel) 13. https://doi.org/10.3390/ani13223468.

Tajchman, K., Ukalska-Jaruga, A., Ceacero, F., Pecio, M., Steiner-Bogdaszewska, Ż., 2022. Concentration of macroelements and trace elements in farmed fallow deer antlers depending on age. Animals (Basel) 12. https://doi.org/10.3390/ani12233409.

Tanck, E., Homminga, J., van Lenthe, G.H., Huiskes, R., 2001. Increase in bone volume fraction precedes architectural adaptation in growing bone. Bone 28, 650–654. https://doi.org/10.1016/s8756-3282(01)00464-1.

Taylor, E.A., Mileti, C.J., Ganesan, S., Kim, J.H., Donnelly, E., 2021. Measures of Bone Mineral Carbonate Content and Mineral Maturity/Crystallinity for FT-IR and Raman Spectroscopic Imaging Differentially Relate to Physical-Chemical Properties of Carbonate-Substituted Hydroxyapatite. Calcif. Tissue Int. 109, 77–91. https://doi.org/10.1007/s00223-021-00825-4.

UniProt Consortium, 2021. UniProt: the universal protein knowledgebase in 2021. Nucleic Acids Res. 49, D480–D489. https://doi.org/10.1093/nar/gkaa1100.

van den Berg, M., Wallen, H., Salmi, A.-K., 2023. The osteometric identification of castrated reindeer (Rangifer tarandus) and the significance of castration in tracing human-animal relationships in the North. Archaeol. Anthropol. Sci. 15, 3. https://doi.org/10.1007/s12520-022-01696-y.

van den Berg, M., Wallen, H., 2025. Osteometric distinctions between domestic reindeer (Rangifer tarandus tarandus), wild mountain reindeer (R.t.t.), wild forest reindeer (R.t. fennicus), and the identification of castrated reindeer bones:

Biometric explorations and archaeological methods. Archaeol. Anthropol. Sci. 17, 94. https://doi.org/10.1007/s12520-025-02198-3.

Vierimaa, H., Sassi, M.L., Eloranta, E., Rahiala, M., Timisjärvi, J., Saarela, S., Risteli, J., 1999. Annual serum PICP and ICTP and antler growth in female reindeer (Rangifer tarandus tarandus). Comp Biochem Physiol B, Biochem Mol Biol 122, 111–117. https://doi.org/10.1016/s0305-0491(98)10153-0.

Voulgaridou, G., Papadopoulou, S.K., Detopoulou, P., Tsoumana, D., Giaginis, C., Kondyli, F.S., Lymperaki, E., Pritsa, A., 2023. Vitamin D and Calcium in Osteoporosis, and the Role of Bone Turnover Markers: A Narrative Review of Recent Data from RCTs. Diseases 11. https://doi.org/10.3390/diseases11010029.

Wang, H., Chu, P.K., 2013. Surface characterization of biomaterials, in: Characterization of Biomaterials. Elsevier, pp. 105–174. https://doi.org/10.1016/B978-0-12-415800-9.00004-8.

Wang, Y., Zhang, C., Wang, N., Li, Z., Heller, R., Liu, R., Zhao, Y., Han, J., Pan, X., Zheng, Z., Dai, X., Chen, C., Dou, M., Peng, S., Chen, X., Liu, J., Li, M., Wang, K., Liu, C., Lin, Z., Qiu, Q., 2019. Genetic basis of ruminant headgear and rapid antler regeneration. Science 364. https://doi.org/10.1126/science.aav6335.

Weldenegodguad, M., Pokharel, K., Ming, Y., Honkatukia, M., Peippo, J., Reilas, T., Røed, K.H., Kantanen, J., 2020. Genome sequence and comparative analysis of reindeer (Rangifer tarandus) in northern Eurasia. Sci. Rep. 10, 8980. https://doi.org/10.1038/s41598-020-65487-y.

Xiao, W., Wang, Y., Pacios, S., Li, S., Graves, D.T., 2016. Cellular and molecular aspects of bone remodeling. Front. Oral Biol. 18, 9–16. https://doi.org/10.1159/000351895.

Yang, X., Rozi, P., Chen, Y., Li, P., Ahmat, M., Feng, X., Liu, Y., 2025. Recent advances in the production, structural characterization, and biological activities of animal bone collagen. Food Science of Animal Products 3, 9240139. https://doi.org/10.26599/FSAP.2025.9240139.

Zysset, P.K., 2009. Indentation of bone tissue: a short review. Osteoporos. Int. 20, 1049–1055. https://doi.org/10.1007/s00198-009-0854-9.

Zysset, P.K., 2009. Indentation of bone tissue: a short review. Osteoporos. Int. 20, 1049–1055. https://doi.org/10.1007/s00198-009-0854-9.

Appendices

Appendix 1. Micro-CT ROI Geometry.

GT; grey threshold; N total = number of images; ROI = region of interest; VOI = volume of interest; Z-range (VOI) = Z-position range of VOI; OP.c = osteoporosis control

ID	Sample type	Lower GT	Upper GT	Pixel size (µm)	Image size (W/H)	N total	ROI shape	ROI (px)	ROI (µm)	VOI (N)	Z-range (VOI)
1	Tibia	40	255	7.5	1836, 1558	1836	Circular	205 x 205	1537.5 x 1537.5	51	878 - 928
	Antler Tip	40	255	7.5	1528, 1303	1528	Circular	181 x 181	1357.5 x 1357.5	31	781 - 811
	Antler Base	40	255	7.5	1880, 1479	1880	Circular	205 x 205	1537.5 x 1537.5	51	885 - 935
2	Tibia	40	255	7.5	1952, 1499	1952	Circular	205 x 205	1537.5 x 1537.5	21	976 - 996
	Antler Tip	40	255	7.5	1180, 1083	1180	Circular	87 x 87	652.5 x 652.5	51	585 - 635
	Antler Base	40	255	7.5	1704, 1492	1704	Circular	148 x 148	1110.0 x 1110.0	51	878 - 928
3	Tibia	40	255	7.5	2276, 1560	2276	Circular	205 x 205	1537.5 x 1537.5	51	1221 - 1271
	Antler Tip	40	255	7.5	1440, 1499	1440	Circular	181 x 181	1357.5 x 1357.5	51	665 - 715
	Antler Base	40	255	7.5	1684, 1473	1684	Circular	181 x 181	1357.5 x 1357.5	51	815 - 865
4	Tibia	40	255	7.5	2276, 1546	2276	Circular	205 x 205	1537.5 x 1537.5	36	1116 - 1151
	Antler Tip	40	255	7.5	1120, 1174	1120	Circular	148 x 148	1110.0 x 1110.0	51	553 - 603
	Antler Base	40	255	7.5	1672, 1443	1672	Circular	73 x 73	547.5 x 547.5	51	774 - 824
5	Tibia	40	255	7.5	1996, 1485	1996	Circular	205 x 205	1537.5 x 1537.5	51	1021 - 1071

ID	Sample type	Lower GT	Upper GT	Pixel size (µm)	Image size (W/H)	N total	ROI shape	ROI (px)	ROI (µm)	VOI (N)	Z-range (VOI)
	Antler Tip	40	255	7.5	1120, 1540	1120	Circular	148 x 148	1110.0 x 1110.0	51	531 - 581
	Antler Base	40	255	7.5	1708, 1505	1708	Circular	148 x 148	1110.0 x 1110.0	6	852 - 857
6	Tibia	40	255	7.5	2160, 1503	2160	Circular	205 x 205	1537.5 x 1537.5	36	944 - 979
	Antler Tip	40	255	7.5	1396, 1184	1396	Circular	87 x 87	652.5 x 652.5	51	706 - 756
	Antler Base	40	255	7.5	1884, 1479	1884	Circular	87 x 87	652.5 x 652.5	31	950 - 980
7	Tibia	40	255	7.5	2428, 1566	2428	Circular	205 x 205	1537.5 x 1537.5	11	1375 - 1385
	Antler Tip	40	255	7.5	1184, 1398	1184	Circular	87 x 87	652.5 x 652.5	21	592 - 612
	Antler Base	40	255	7.5	2104, 1563	2104	Circular	205 x 205	1537.5 x 1537.5	31	1051 - 1081
8	Tibia	40	255	7.5	2428, 1637	2428	Circular	205 x 205	1537.5 x 1537.5	36	1441 - 1476
	Antler Tip	40	255	7.5	880, 1022	880	Circular	87 x 87	652.5 x 652.5	51	405 - 455
	Antler Base	40	255	7.5	1396, 1506	1396	Circular	87 x 87	652.5 x 652.5	11	690 - 700
9	Tibia	40	255	7.5	2268, 1543	2268	Circular	205 x 205	1537.5 x 1537.5	51	1268 - 1318
	Antler Tip	40	255	7.5	924, 1242	924	Circular	87 x 87	652.5 x 652.5	51	395 - 445
	Antler Base	40	255	7.5	1340, 1442	1340	Circular	87 x 87	652.5 x 652.5	51	647 - 697
OP. c	Antler Base	40	255	7.5	2016, 1546	2016	Circular	205 x 205	1537.5 x 1537.5	36	983 - 1018

Appendix 2. Raw data gained from PANalytical EMPYREAN series 2 XRD analysis.

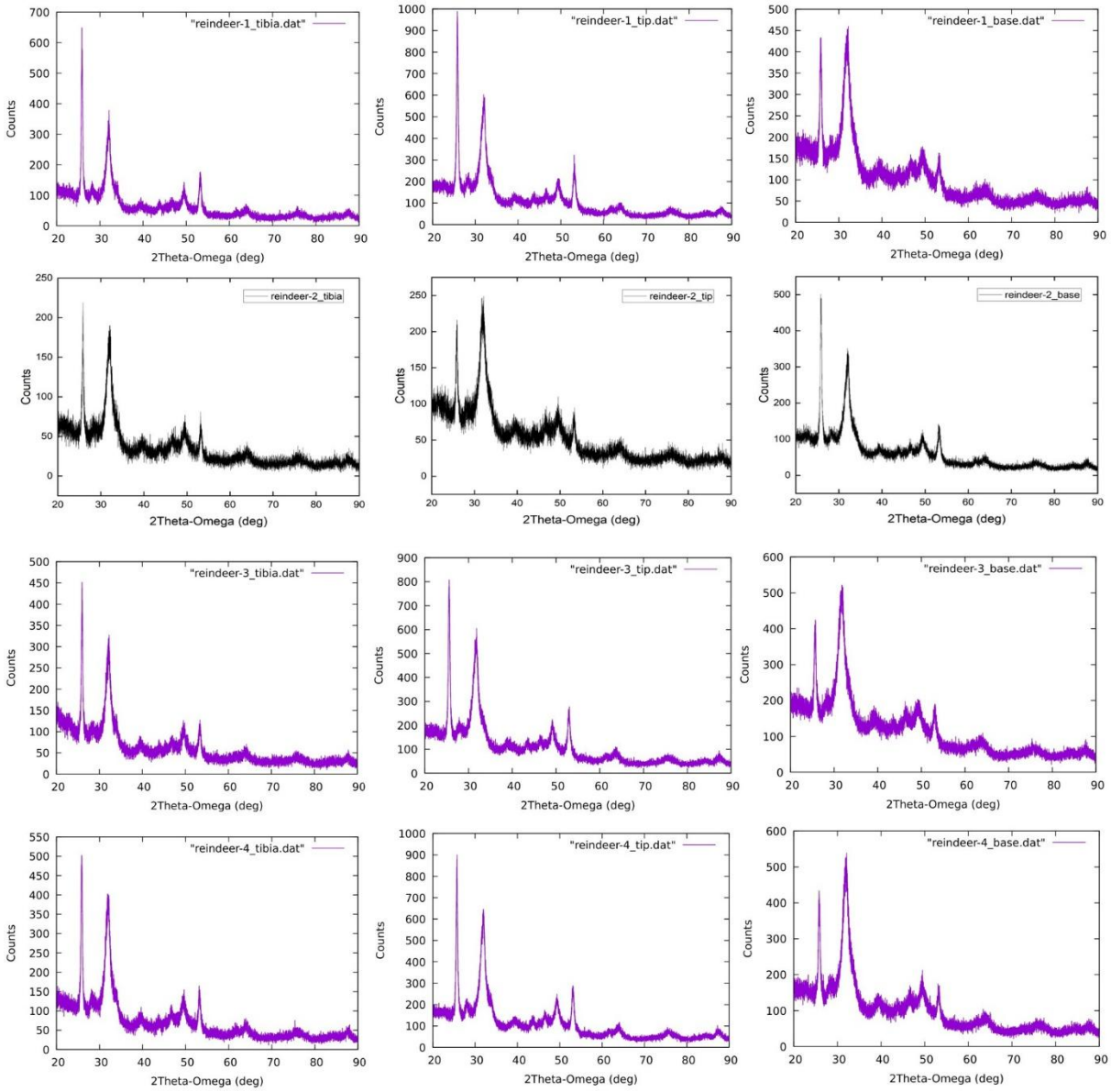

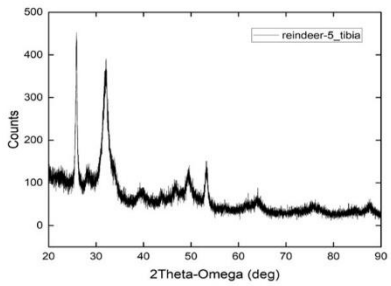
reindeer-5_tibia
Counts
2Theta-Omega (deg)

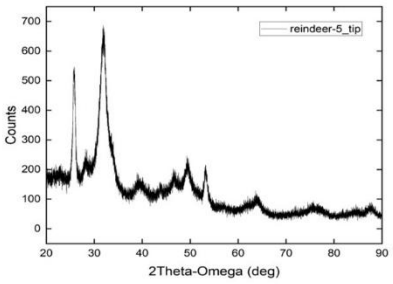
reindeer-5_tip
Counts
2Theta-Omega (deg)

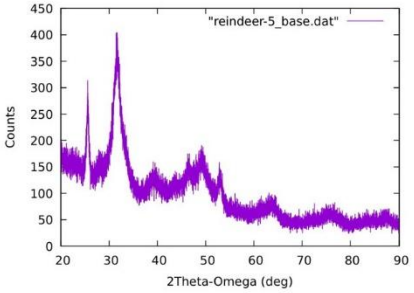
"reindeer-5_base.dat"
Counts
2Theta-Omega (deg)

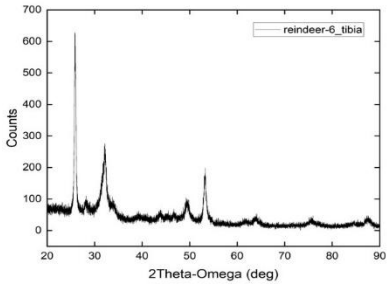
reindeer-6_tibia
Counts
2Theta-Omega (deg)

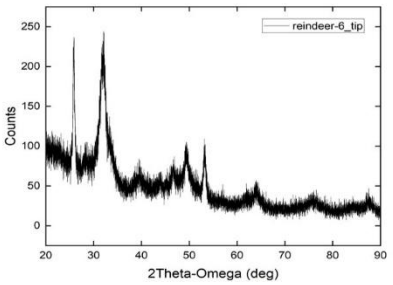
reindeer-6_tip
Counts
2Theta-Omega (deg)

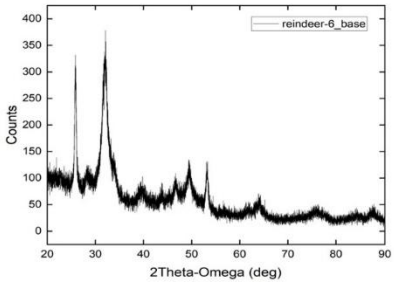
reindeer-6_base
Counts
2Theta-Omega (deg)

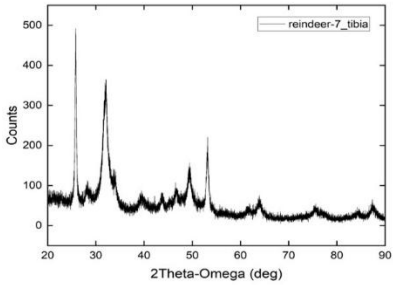
reindeer-7_tibia
Counts
2Theta-Omega (deg)

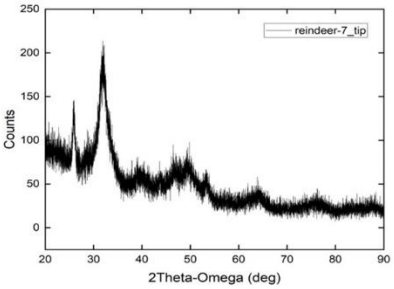
reindeer-7_tip
Counts
2Theta-Omega (deg)

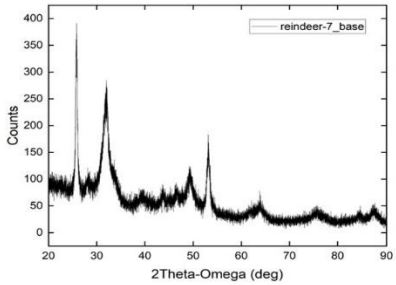
reindeer-7_base
Counts
2Theta-Omega (deg)

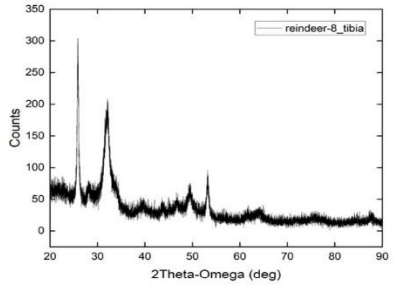
reindeer-8_tibia
Counts
2Theta-Omega (deg)

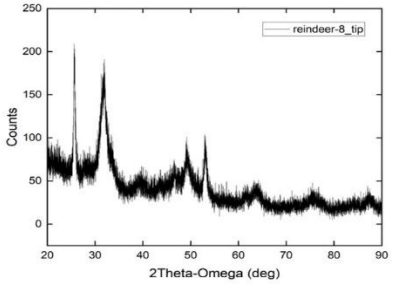
reindeer-8_tip
Counts
2Theta-Omega (deg)

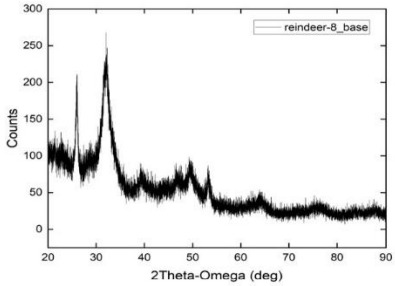
reindeer-8_base
Counts
2Theta-Omega (deg)

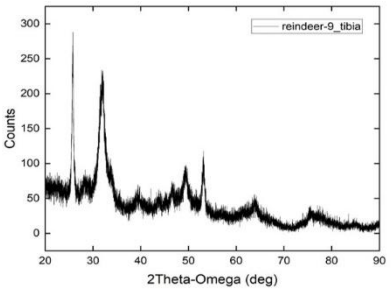
reindeer-9_tibia
Counts
2Theta-Omega (deg)

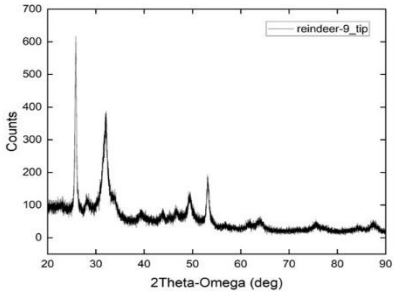
reindeer-9_tip
Counts
2Theta-Omega (deg)

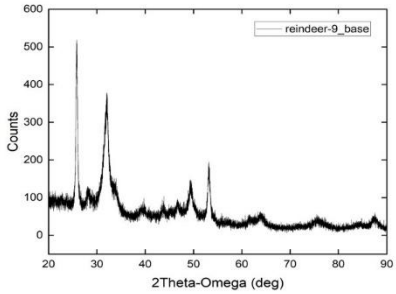
reindeer-9_base
Counts
2Theta-Omega (deg)

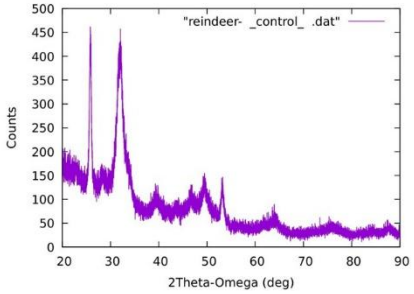
"reindeer- _control_ .dat"
Counts
2Theta-Omega (deg)

Appendix 3. Baseline corrected XRD spectra of individuals 1–9 from three sampling locations (tibia, antler tip, and antler base).

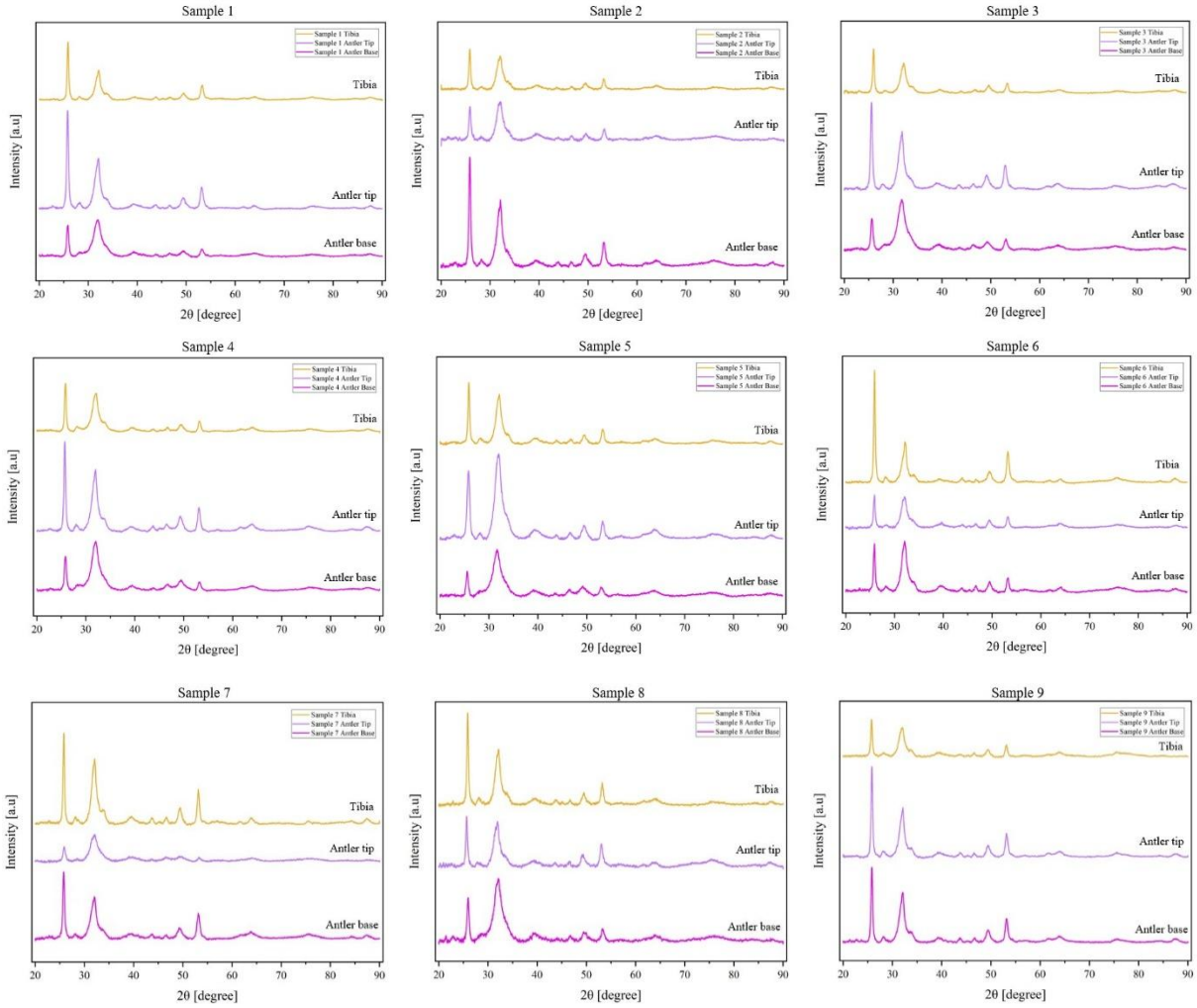

Appendix 4. Nonlinear Fitting on the baseline corrected XRD spectra.

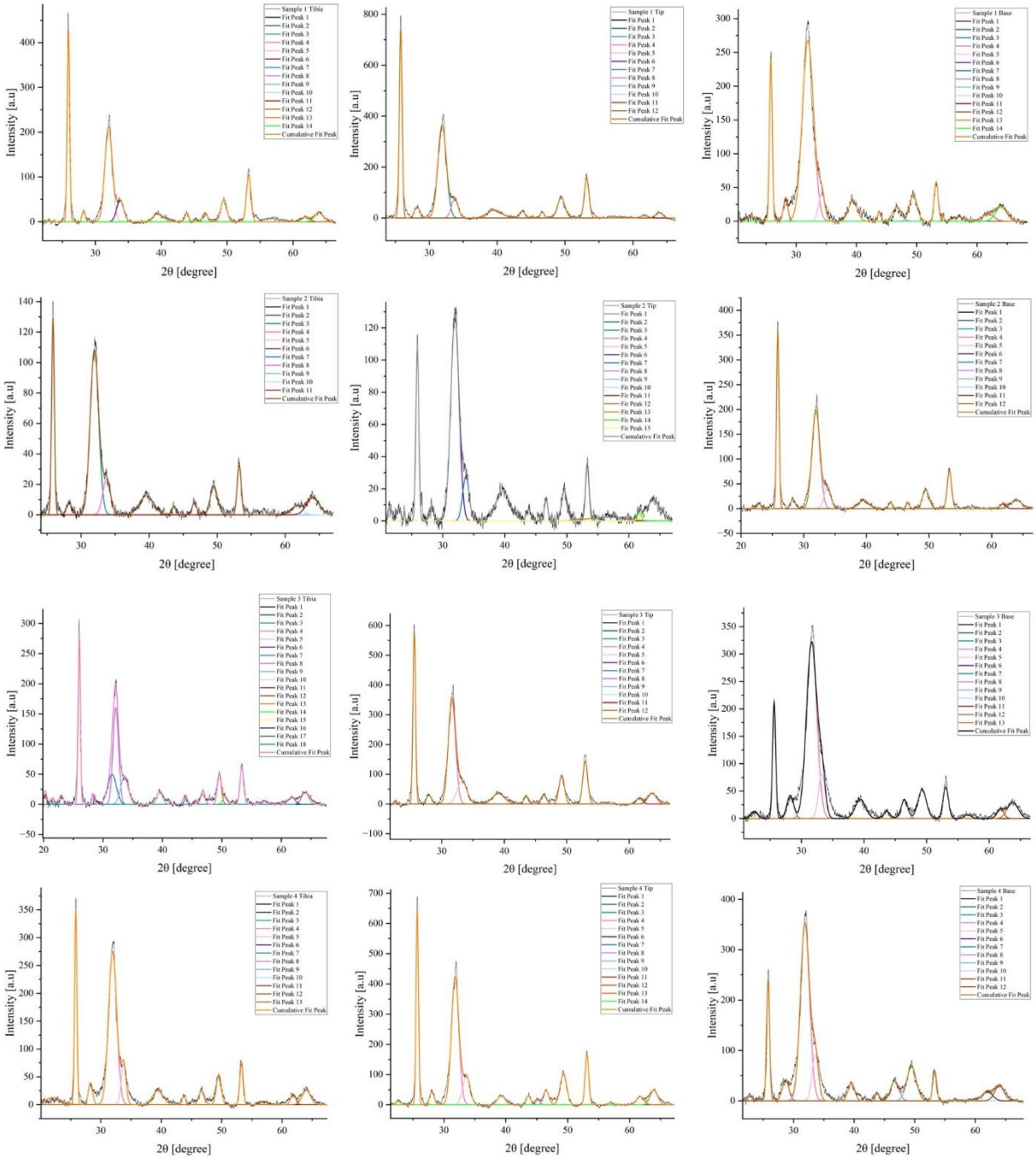

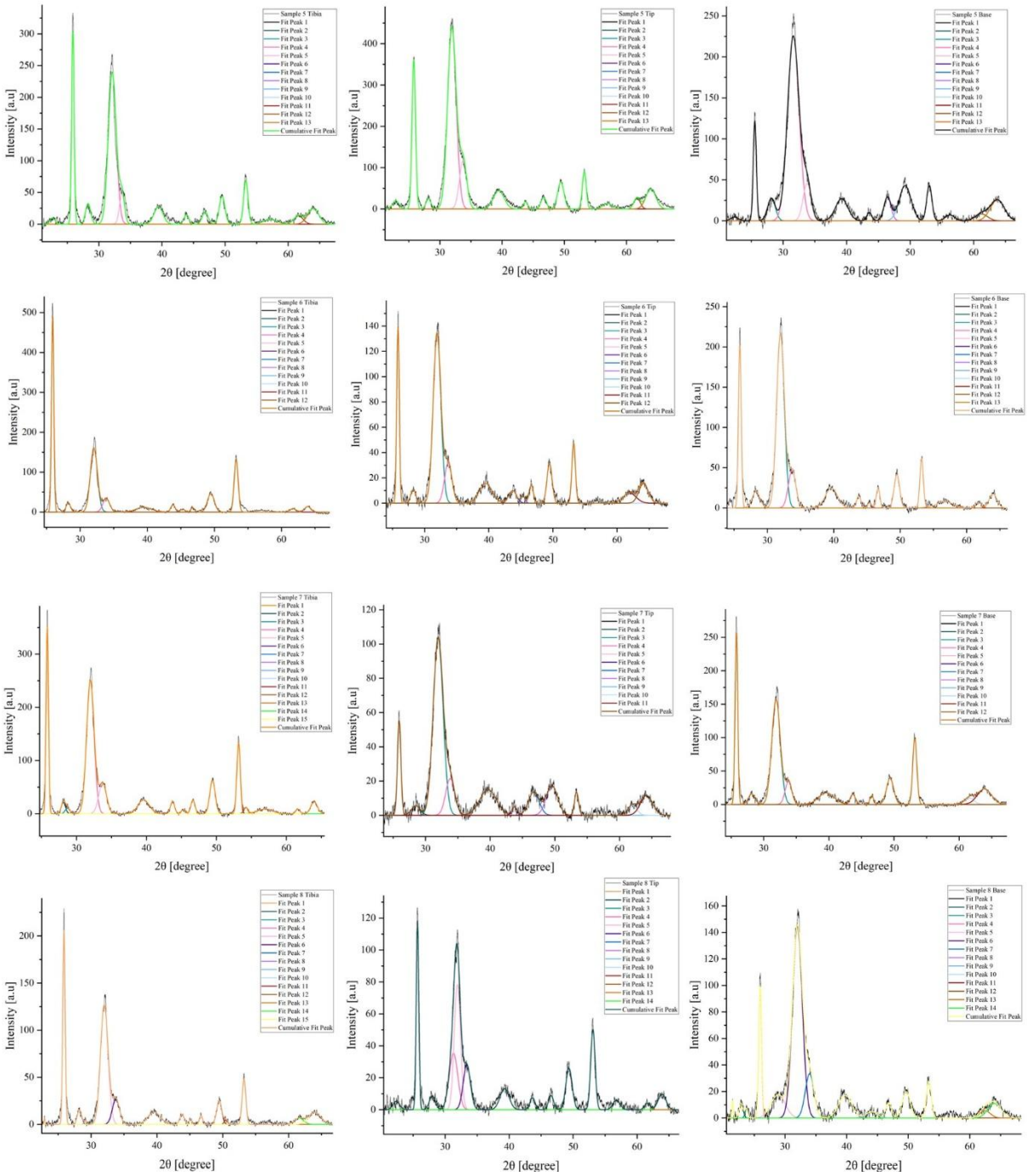
Sample 5 Tibia
Sample 5 Tip
Sample 5 Base
Sample 6 Tibia
Sample 6 Tip
Sample 6 Base
Sample 7 Tibia
Sample 7 Tip
Sample 7 Base
Sample 8 Tibia
Sample 8 Tip
Sample 8 Base
Intensity [a.u]
2θ [degree]

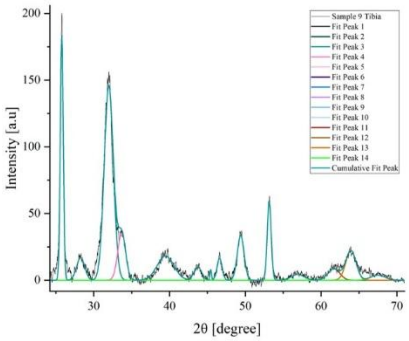
Sample 9 Tibia
Fit Peak 1
Fit Peak 2
Fit Peak 3
Fit Peak 4
Fit Peak 5
Fit Peak 6
Fit Peak 7
Fit Peak 8
Fit Peak 9
Fit Peak 10
Fit Peak 11
Fit Peak 12
Fit Peak 13
Fit Peak 14
Cumulative Fit Peak
Intensity [a.u]
2θ [degree]

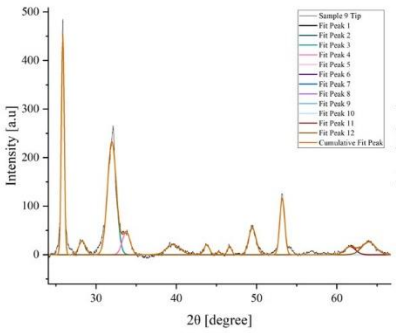
Sample 9 Tip
Fit Peak 1
Fit Peak 2
Fit Peak 3
Fit Peak 4
Fit Peak 5
Fit Peak 6
Fit Peak 7
Fit Peak 8
Fit Peak 9
Fit Peak 10
Fit Peak 11
Fit Peak 12
Cumulative Fit Peak
Intensity [a.u]
2θ [degree]

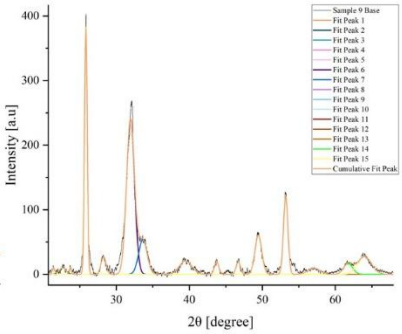
Sample 9 Base
Fit Peak 1
Fit Peak 2
Fit Peak 3
Fit Peak 4
Fit Peak 5
Fit Peak 6
Fit Peak 7
Fit Peak 8
Fit Peak 9
Fit Peak 10
Fit Peak 11
Fit Peak 12
Fit Peak 13
Fit Peak 14
Fit Peak 15
Cumulative Fit Peak
Intensity [a.u]
2θ [degree]

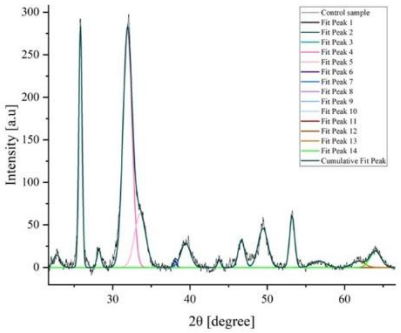
Control sample
Fit Peak 1
Fit Peak 2
Fit Peak 3
Fit Peak 4
Fit Peak 5
Fit Peak 6
Fit Peak 7
Fit Peak 8
Fit Peak 9
Fit Peak 10
Fit Peak 11
Fit Peak 12
Fit Peak 13
Fit Peak 14
Cumulative Fit Peak
Intensity [a.u]
2θ [degree]

Appendix 5. Crystallite size calculations.

ID	Sample type	Peak position of 0 0 2	FWHM of 0 0 2	Crystallite size D of 0 0 2
Sample 1	Tibia	25,90956	0,43081	19,76294585
	Antler base	25,81238	0,54183	15,7104943
	Antler tip	25,80099	0,47821	17,80017836
Sample 2	Tibia	25,861	0,47265	18,01173295
	Antler base	25,87529	0,4681	18,18733047
	Antler tip	25,90622	0,55805	15,25672901
Sample 3	Tibia	25,99985	0,44674	19,06169322
	Antler base	25,63942	0,58726	14,49014699
	Antler tip	25,57957	0,49577	17,16213899
Sample 4	Tibia	25,84431	0,4477	19,01487827
	Antler base	25,79881	0,57641	14,7675894
	Antler tip	25,70734	0,45269	18,80013495
Sample 5	Tibia	25,87825	0,45635	18,65572459
	Antler base	25,55738	0,57677	14,751287
	Antler tip	25,80417	0,67332	12,64224648
Sample 6	Tibia	25,90048	0,40613	20,96353271
	Antler base	25,86381	0,48091	17,70246722
	Antler tip	25,86369	0,46753	18,20908063
Sample 7	Tibia	25,82393	0,39409	21,60068456
	Antler base	25,80562	0,47052	18,09126514
	Antler tip	25,92081	0,63048	13,50442049
Sample 8	Tibia	25,88117	0,42171	20,18825677
	Antler base	25,96193	0,54468	15,63297858
	Antler tip	25,68217	0,46891	18,14891294
Sample 9	Tibia	25,77818	0,45792	18,58804026
	Antler base	25,83141	0,43168	19,72002683
	Antler tip	25,8433	0,41749	20,39077292

ID	Sample type	Peak position of 0 0 2	FWHM of 0 0 2	Crystallite size D of 0 0 2
Control	Antler base	25,82752	0,50109	16,98831531

ID	Sample type	Peak position of 0 0 4	FWHM of 0 0 4	Crystallite size D of 0 0 4
Sample 1	Tibia	53,27105	0,79945	11,6110523
	Antler base	53,22252	0,76903	12,06778069
	Antler tip	53,1941	0,81318	11,41116685
Sample 2	Tibia	53,23134	0,68717	13,50589126
	Antler base	53,2611	0,80701	11,50178012
	Antler tip	53,29776	0,67884	13,67559555
Sample 3	Tibia	53,3724	0,75155	12,35656811
	Antler base	53,05669	1,01932	9,097998018
	Antler tip	52,97587	0,93244	9,942205066
Sample 4	Tibia	53,28867	0,65387	14,19727434
	Antler base	53,29669	0,74611	12,44253231
	Antler tip	53,10914	0,67928	13,65547603
Sample 5	Tibia	53,28484	0,82208	11,29210795
	Antler base	53,01334	0,96683	9,590125469
	Antler tip	53,21428	0,73496	12,62674306
Sample 6	Tibia	53,24595	0,70648	13,13757836
	Antler base	53,22097	0,61137	15,17971522
	Antler tip	53,23424	0,64151	14,46736762
Sample 7	Tibia	53,17255	0,58185	15,9464796
	Antler base	53,19257	0,74268	12,49430525
	Antler tip	53,35554	0,72685	12,77552745
Sample 8	Tibia	53,23366	0,66657	13,92342509
	Antler base	53,34629	0,90684	10,2394199
	Antler tip	53,09391	0,81276	11,41207213
Sample 9	Tibia	53,14743	0,60901	15,23364405
	Antler base	53,19728	0,71202	13,0325856

ID	Sample type	Peak position of 0 0 4	FWHM of 0 0 4	Crystallite size D of 0 0 4
	Antler tip	53,20258	0,72286	12,83744642
Control	Antler base	53,20604	0,77106	12,03514233

Appendix 6. XRD peak information used for the c-orientation calculations.

ID	Sample type	Peak position (2θ) of 0 0 2	Peak Area of 0 0 2	Peak position (2θ) of 3 1 0	Peak Area of 3 1 0	Area ratio 0 0 2 / 3 1 0
Sample 1	Tibia	25,90956	197,13376	39,53227	35,14406	5,609305242
	Antler base	25,81238	138,67728	39,394	55,74906	2,487526785
	Antler tip	25,80099	382,16402	39,61456	83,03293	4,602559731
Sample 2	Tibia	25,861	64,68471	39,60895	32,42432	1,994944227
	Antler base	25,87529	178,41654	39,52736	35,36441	5,04508742
	Antler tip	25,90622	62,98229	39,69029	54,46947	1,156286081
Sample 3	Tibia	25,99985	132,82873	39,55008	26,8836	4,940883289
	Antler base	25,63942	132,98853	39,42902	71,06582	1,871343073
	Antler tip	25,57957	303,62428	39,06347	84,69133	3,585069215
Sample 4	Tibia	25,84431	167,90658	39,44625	55,53628	3,023367428
	Antler base	25,79881	148,13515	39,54775	48,44762	3,057635236
	Antler tip	25,70734	314,51688	39,27808	45,45208	6,919746687
Sample 5	Tibia	25,87825	149,70515	39,44399	47,71574	3,137437458
	Antler base	25,55738	74,95433	39,21953	65,82479	1,138694556
	Antler tip	25,80417	258,55766	39,47211	95,11446	2,718384355
Sample 6	Tibia	25,90048	211,96479	39,48323	33,6731	6,294780997
	Antler base	25,86381	104,82016	39,6467	56,26548	1,862956825
	Antler tip	25,86369	69,39415	39,52218	40,19846	1,726288768
	Tibia	25,82393	149,59547	39,60088	53,01765	2,821616386

ID	Sample type	Peak position (2θ) of 0 0 2	Peak Area of 0 0 2	Peak position (2θ) of 3 1 0	Peak Area of 3 1 0	Area ratio 0 0 2 / 3 1 0
Sample 7	Antler base	25,80562	130,95214	39,63224	52,25524	2,506009732
	Antler tip	25,92081	37,12024	39,66799	48,38948	0,767113844
Sample 8	Tibia	25,88117	92,74383	39,57685	31,55607	2,939017121
	Antler base	25,96193	57,06084	39,76445	46,19651	1,235176424
	Antler tip	25,68217	59,03828	39,28435	23,4723	2,515231997
Sample 9	Tibia	25,77818	89,51021	39,4697	49,98551	1,790723152
	Antler base	25,83141	176,68764	39,49403	44,30761	3,987749283
	Antler tip	25,8433	201,75791	39,64654	44,39108	4,545010169
Control	Antler base	25,82752	151,28742	39,43109	44,09709	3,430780126

Appendix 7. Baseline-corrected ATR-FTIR spectra (PerkinElmer Frontier IR) of analysed a) antler tibias, b) antler tips, and c) antler bases.

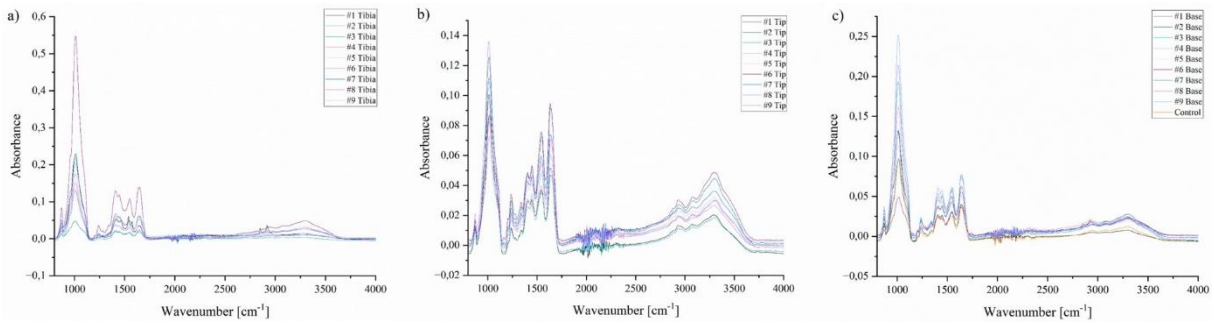

Appendix 8. Raw and processed data (conversion and baseline correction) from PerkinElmer Spectrum 100.

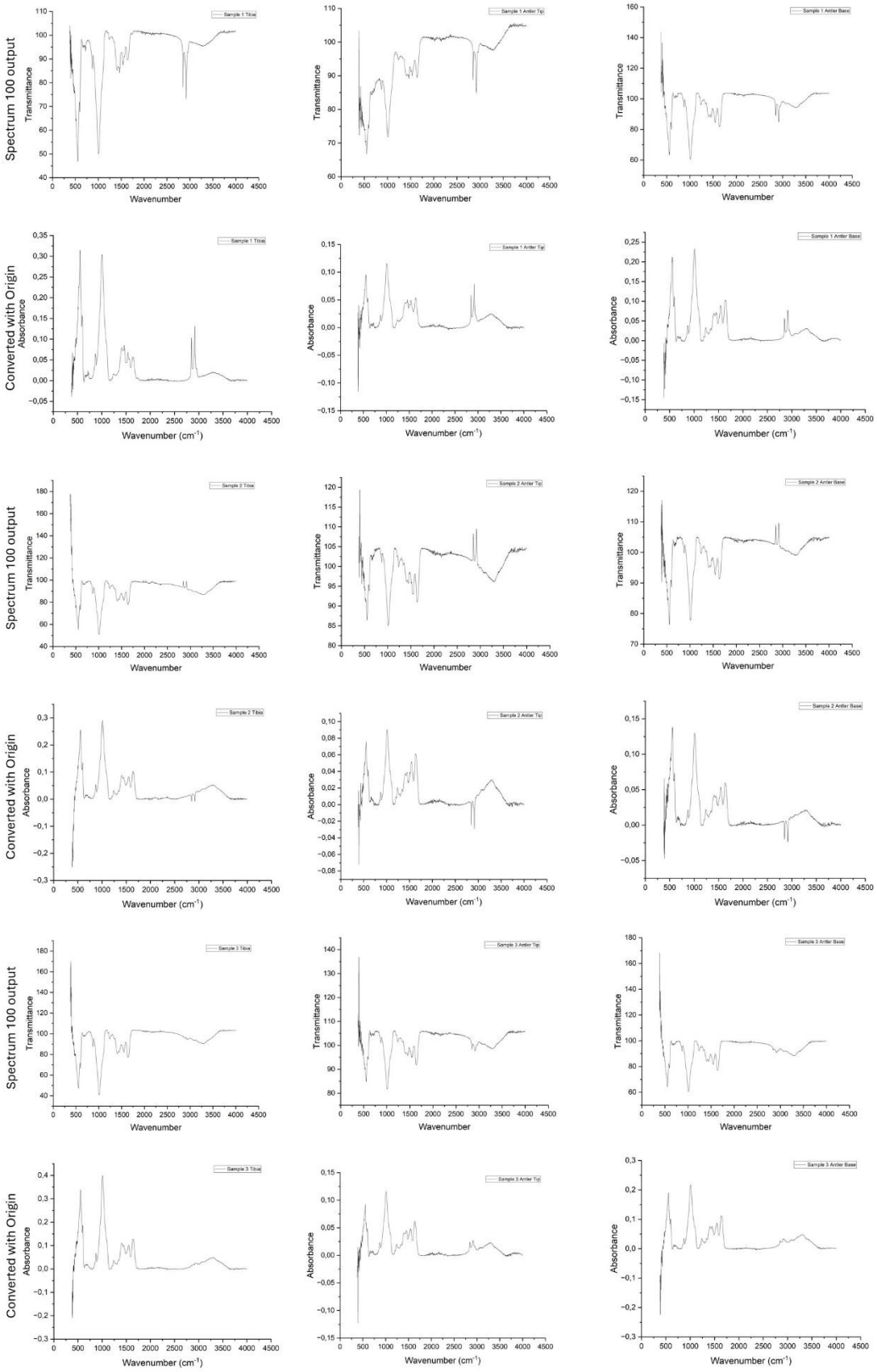

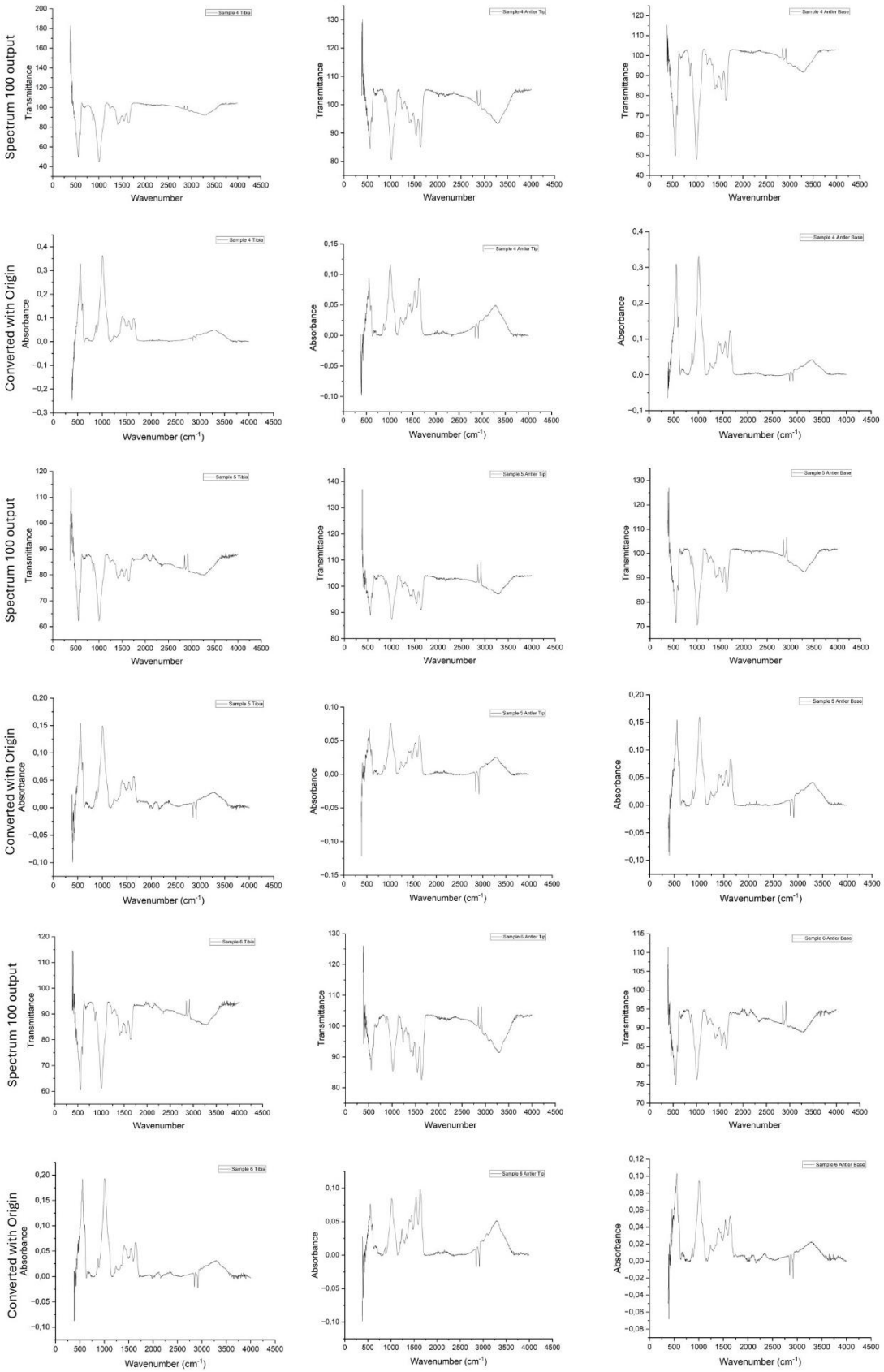
Spectrum 100 output
Transmittance
Wavenumber
Converted with Origin
Absorbance
Wavenumber (cm-1)
Sample 4 Tibia
Sample 4 Antler Tip
Sample 4 Antler Base
Sample 5 Tibia
Sample 5 Antler Tip
Sample 5 Antler Base
Sample 6 Tibia
Sample 6 Antler Tip
Sample 6 Antler Base

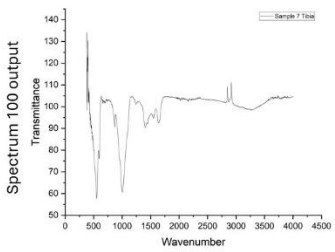
Spectrum 100 output
Transmittance
Wavenumber

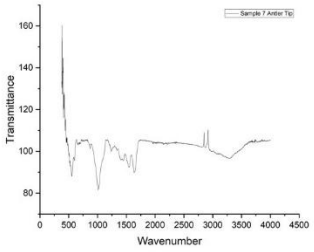
Transmittance
Wavenumber

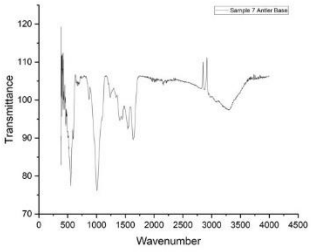
Transmittance
Wavenumber

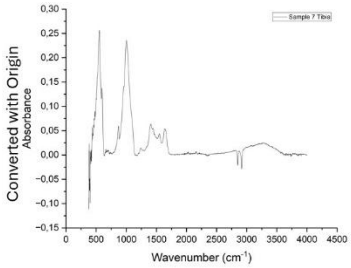
Converted with Origin
Absorbance
Wavenumber (cm-1)

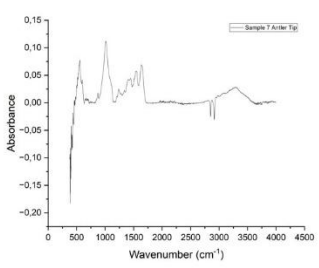
Absorbance
Wavenumber (cm-1)

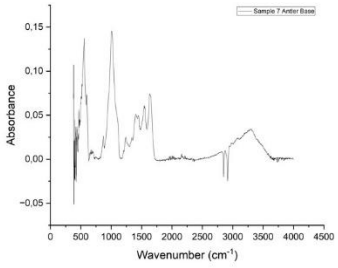
Absorbance
Wavenumber (cm-1)

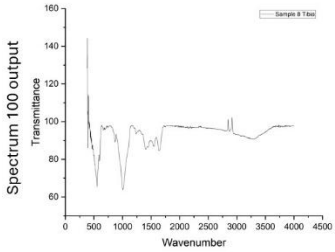
Spectrum 100 output
Transmittance
Wavenumber

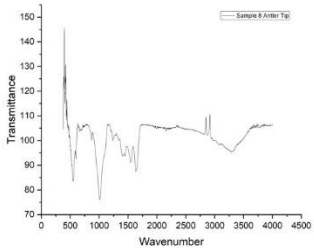
Transmittance
Wavenumber

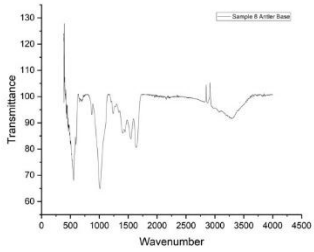
Transmittance
Wavenumber

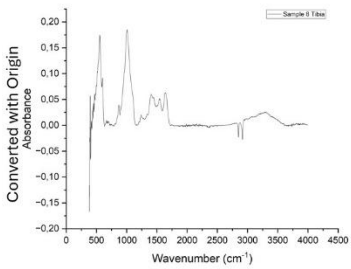
Converted with Origin
Absorbance
Wavenumber (cm-1)

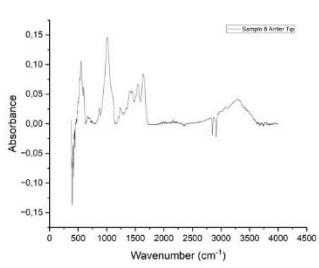
Absorbance
Wavenumber (cm-1)

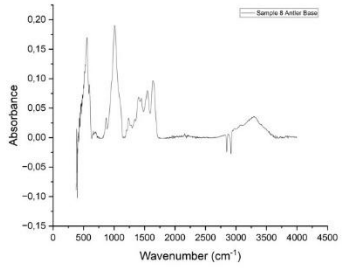
Absorbance
Wavenumber (cm-1)

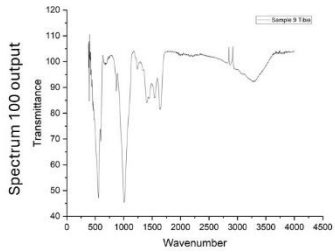
Spectrum 100 output
Transmittance
Wavenumber

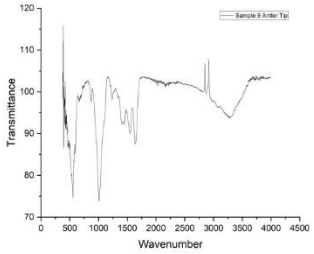
Transmittance
Wavenumber

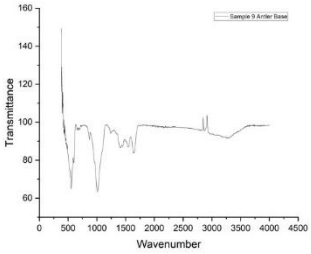
Transmittance
Wavenumber

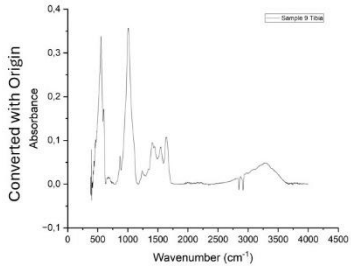
Converted with Origin
Absorbance
Wavenumber (cm-1)

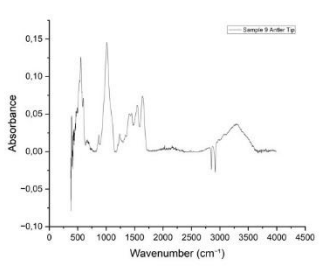
Absorbance
Wavenumber (cm-1)

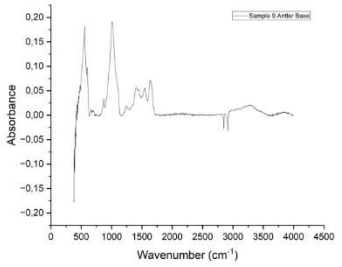
Absorbance
Wavenumber (cm-1)

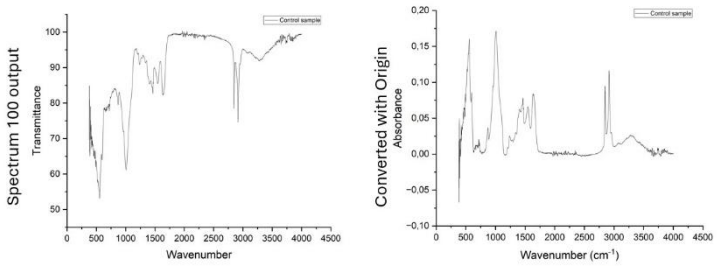
Spectrum 100 output
Transmittance
Wavenumber
Control sample
Converted with Origin
Absorbance
Wavenumber (cm-1)
Control sample

Appendix 9. ATR-FTIR parameter calculations based on the measurements obtained with PerkinElmer IR Frontier at the Turku Clinical Biomaterials Centre.

	#1 Base			#1 Tibia			#1 Tip		
Parameter	**cm-1**	**Intensity ratio**	**Result**	**cm-1**	**Intensity ratio**	**Result**	**cm-1**	**Intensity ratio**	**Result**
Amide I to phosphate	1635,13/1010,63	0,0398/0,1312	0,30335	1645,38/1010,91	0,034/0,2297	0,14802	1634,62/1011,76	0,0515/0,1003	0,51346
Amide II to phosphate	1548,11/1010,63	0,0309/0,1312	0,23552	1538,46/1010,91	0,0605/0,2297	0,26339	1547,86/1011,76	0,037/0,1003	0,36889
Amide III + Collagen to phosphate	(1205+1238,24+ 1280)/1010,63	(0,0002+0,0106+ 0,0036)/0,1312	0,10976	(1206+1238+1280) /1010,91	(0,0016+0,0088+ 0,0069)/0,2297	0,07532	(1205+1238+1281) /1011,76	(0,0016+0,0112+ 0,0047)/0,1003	0,17448
Amide I + Amide II to phosphate	(1548,11 + 1635,13)/1010,63	(0,0309 + 0,0398)/0,1312	0,53887	(1538,46 + 1645,38)/1010,91	(0,0605+0,034)/ 0,2297	0,41141	(1547,86 + 1634,62)/1011,76	(0,037 + 0,0515)/0,1003	0,88235
Amides + Collagen to phosphates	(1205+1238,24+ 1280+1635,13+ 1548,11)/1010,63	(0,0002+0,0106+ 0,0036+0,0398+ 0,0309)/0,1312	0,64863	(1206+1238+1280+ 1645,38+1538,46)/ 1010,91	(0,0016+0,0088+ 0,0069+0,034+ 0,0605)/0,2297	0,48672	(1205+1238+1281+ 1634,62+1547,86)/ 1011,76	(0,0016+0,0112+ 0,0047+0,0515+ 0,037)/0,1003	1,05683
Carbonate accumulation	871,61/1635,13	0,0165/0,0398	0,41457	870,93/1645,38	0,042/0,034	1,23529	871,75/1634,62	0,011/0,0515	0,21359
Crystallinity	1 /FWHM of 1010,63	1 / 91,826913	0,01089	1/FWHM of 1010,91	1/ 99,96571	0,01	1 /FWHM of 1011,76	1 / 91,688332	0,01091
Mineral to matrix ratio	1010,63 / 1635,13	0,1312/0,0398	3,29648	1010,91/1645,38	0,2297/0,034	6,75588	1011,76/1634,62	0,1003/0,0515	1,94757
Mineral maturity	1010,63/1104	0,1312/0,0369	3,55556	1010,91/1103	0,2297/0,0702	3,27208	1011,76/1105	0,1003/0,0285	3,5193
Secondary structure of proteins	1635,13/1238,24	0,0398/0,0106	3,75472	1645,38/1238	0,034/0,0088	3,86364	1634,62/1238	0,0515/0,0112	4,59821
	#2 Base			**#2 Tibia**			**#2 Tip**		
Parameter	**cm-1**	**Intensity ratio**	**Result**	**cm-1**	**Intensity ratio**	**Result**	**cm-1**	**Intensity ratio**	**Result**
Amide I to phosphate	1635,89/1014,17	0,0626/0,0973	0,64337	1642,88/1005,18	0,0191/0,0479	0,39875	1634,11/1012,07	0,0917/0,1255	0,73068
Amide II to phosphate	1547,8/1014,17	0,05/0,0973	0,51387	1550/1005,18	0,016/0,0479	0,33403	1548,74/1012,07	0,0727/0,1255	0,57928
Amide III + Collagen to phosphate	(1205+1238,56+ 1280)/1014,17	(0,0065+0,0197+ 0,0113)/0,0973	0,38541	(1203+1240+1282) /1005,18	(0,0016+0,005+ 0,0035)/0,0479	0,21086	(1204+1238,18+ 1280)/1012,07	(0,0129+0,03+ 0,018)/0,1255	0,48526
Amide I + Amide II to phosphate	(1547,8+1635,89)/ 1014,17	(0,05+0,0626)/ 0,0973	1,15725	(1550+1642,88)/ 1005,18	(0,016+0,0191)/ 0,0479	0,73278	(1548,74+1634,11) /1012,07	(0,0727+0,0917)/ 0,1255	1,30996

Amides + Collagen to phosphates	(1205+1238,56+ 1280+1635,89+ 1547,8)/1014,17	(0,0065+0,0197+ 0,0113+0,0626+ 0,05)/0,0973	1,54265	(1203+1240+1282+ 1642,88+1550)/ 1005,18	(0,0016+0,005+ 0,0035+0,0191+ 0,016)/0,0479	0,94363	(1204+1238,18+ 1280+1634,11+ 1548,74)/1012,07	(0,0129+0,03+ 0,018+0,0917+ 0,0727)/0,1255	1,79522
Carbonate accumulation	871,7/1635,89	0,013/0,0626	0,20767	871/1642,88	0,0124/0,0191	0,64921	871,78/1634,11	0,0165/0,0917	0,17993
Crystallinity	1/FWHM of 1014,17	1/94,457989	0,01059	1/FWHM of 1005,18	1/130,369747	0,00767	1/FWHM of 1012,07	1/94,438368	0,01059
Mineral to matrix ratio	1014,17/1635,89	0,0973/0,0626	1,55431	1005,18/1642,88	0,0479/0,0191	2,50785	1012,07/1634,11	0,1255/0,0917	1,36859
Mineral maturity	1014,17/1103	0,0973/0,0323	3,01238	1005,18/1102	0,0479/0,0181	2,64641	1012,07/1102	0,1255/0,0408	3,07598
Secondary structure of proteins	1635,89/1238,56	0,0626/0,0197	3,17766	1642,88/1240	0,0191/0,005	3,82	1634,11/1238,18	0,0917/0,03	3,05667
		#3 Base			**#3 Tibia**			**#3 Tip**	
Parameter	**cm-1**	**Intensity ratio**	**Result**	**cm-1**	**Intensity ratio**	**Result**	**cm-1**	**Intensity ratio**	**Result**
Amide I to phosphate	1635,06/1011,46	0,077/0,1938	0,39732	1645,75/1006,79	0,0241/0,1303	0,18496	1635,03/1011,19	0,047/0,086	0,54651
Amide II to phosphate	1548,59/1011,46	0,0608/0,1938	0,31373	1548/1006,79	0,0171/0,1303	0,13124	1548,05/1011,19	0,0358/0,086	0,41628
Amide III + Collagen to phosphate	(1205+1237,9+ 1280)/1011,46	(0,0062+0,0235+ 0,0111)/0,1938	0,21053	(1204+1240+1283) /1006,79	(-0,0032+0,0028+ -0,0009)/0,1303	-0,00998	(1203+1237,97+ 1279)/1011,19	(0,0029+0,0122+ 0,0052)/0,086	0,23605
Amide I + Amide II to phosphate	(1548,59 + 1635,06)/1011,46	(0,0608+0,077)/ 0,1938	0,71104	(1548 + 1645,75)/1006,79	(0,0171+0,0241)/ 0,1303	0,31619	(1548,05+1635,03) /1011,19	(0,0358+0,047)/ 0,086	0,96279
Amides + Collagen to phosphates	(1205+1237,9+ 1280+1635,06+ 1548,59)/1011,46	(0,0062+0,0235+ 0,0111+0,077+ 0,0608)/0,1938	0,92157	(1204+1240+1283+ 1645,75+1548)/ 1006,79	(-0,0032+0,0028+- 0,0009+0,0241+ 0,0171)/0,1303	0,30622	(1203+1237,97+ 1279+1635,03+ 1548,05)/1011,19	(0,0029+0,0122+ 0,0052+0,047+ 0,0358)/0,086	1,19884
Carbonate accumulation	871,75/1635,06	0,0252/0,077	0,32727	870,98/1645,75	0,0227/0,0241	0,94191	871,45/1635,03	0,0104/0,047	0,22128
Crystallinity	1 /FWHM of 1011,46	1 /91,292217	0,01095	1 /FWHM of 1006,79	1 /112,083406	0,00892	1 /FWHM of 1011,19	1/ 93,560342	0,01069
Mineral to matrix ratio	1011,46/1635,06	0,1938/0,077	2,51688	1006,79/1645,75	0,1303/0,0241	5,40664	1011,19/1635,03	0,086/0,047	1,82979
Mineral maturity	1011,46/1103	0,1938/0,058	3,34138	1006,79/1104	0,1303/0,0365	3,56986	1011,19/1103	0,086/0,0255	3,37255
Secondary structure of proteins	1635,06/1237,9	0,077/0,0235	3,2766	1645,75/1240	0,0241/0,0028	8,60714	1635,03/1237,97	0,047/0,0122	3,85246
		#4 Base			**#4 Tibia**			**#4 Tip**	
Parameter	**cm-1**	**Intensity ratio**	**Result**	**cm-1**	**Intensity ratio**	**Result**	**cm-1**	**Intensity ratio**	**Result**
Amide I to phosphate	1641,27/1011,15	0,0616/0,1613	0,3819	1646,25/1007,81	0,0589/0,175	0,33657	1635,37/1011,45	0,0512/0,0829	0,61761

Amide II to phosphate	1544,59/1011,15	0,0486/0,1613	0,3013	1543,79/1007,81	0,0508/0,175	0,29029	1545,02/1011,45	0,0396/0,0829	0,47768
Amide III + Collagen to phosphate	(1208+1239+1282) /1011,15	(0,0076+0,019+ 0,0124)/0,1613	0,24179	(1203+1240+1284) /1007,81	(0,0021+0,0139+ 0,0081)/0,175	0,13771	(1205+1239+1280) /1011,45	(0,0069+0,0172+ 0,0107)/0,0829	0,41978
Amide I + Amide II to phosphate	(1544,59+1641,27) /1011,15	(0,0486+0,0616)/ 0,1613	0,6832	(1543,79+1646,25) /1007,81	(0,0508+0,0589)/ 0,175	0,62686	(1545,02+1635,37) /1011,45	(0,0396+0,0512)/ 0,0829	1,0953
Amides + Collagen to phosphates	(1208+1239+1282+ 1641,27+1544,59)/ 1011,15	(0,0076+0,019+ 0,0124+0,0616+ 0,0486)/0,1613	0,92498	(1203+1240+1284+ 1646,25+1543,79)/ 1007,81	(0,0021+0,0139+ 0,0081+0,0589+ 0,0508)/0,175	0,76457	(1205+1239+1280+ 1635,37+1545,02)/ 1011,45	(0,0069+0,0172+ 0,0107+0,0512+ 0,0396)/0,0829	1,51508
Carbonate accumulation	871,2/1641,27	0,0283/0,0616	0,45942	871,07/1646,25	0,0355/0,0589	0,60272	872/1635,37	0,0131/0,0512	0,25586
Crystallinity	1 /FWHM of 1011,15	1 /95,927657	0,01042	1 /FWHM of 1007,81	1 /110,554477	0,00905	1 /FWHM of 1011,45	1 /108,445415	0,00922
Mineral to matrix ratio	1011,15/1641,27	0,1613/0,0616	2,61851	1007,81/1646,25	0,175/0,0589	2,97114	1011,45/1635,37	0,0829/0,0512	1,61914
Mineral maturity	1011,15/1103	0,1613/0,0493	3,27181	1007,81/1104	0,175/0,0506	3,4585	1011,45/1103	0,0829/0,0279	2,97133
Secondary structure of proteins	1641,27/1239	0,0616/0,019	3,24211	1646,25/1240	0,0589/0,0139	4,23741	1635,37/1239	0,0512/0,0172	2,97674
		#5 Base			**#5 Tibia**			**#5 Tip**	
Parameter	**cm-1**	**Intensity ratio**	**Result**	**cm-1**	**Intensity ratio**	**Result**	**cm-1**	**Intensity ratio**	**Result**
Amide I to phosphate	1634,89/1008,63	0,0514/0,1127	0,45608	1644,32/1007,97	0,0361/0,1344	0,2686	1634,7/1013,66	0,0676/0,0929	0,72766
Amide II to phosphate	1539,82/1008,63	0,0403/0,1127	0,35759	1538,65/1007,97	0,0325/0,1344	0,24182	1538,55/1013,66	0,0533/0,0929	0,57374
Amide III + Collagen to phosphate	(1205+1238,76+ 1280)/1008,63	(0,0068+0,0174+ 0,0106)/0,1127	0,30878	(1205+1240+1282) /1007,97	(0,0015+0,0078+ 0,0055)/0,1344	0,11012	(1205+1237+1280) /1013,66	(0,0113+0,0226+ 0,0144)/0,0929	0,51991
Amide I + Amide II to phosphate	(1539,82+1634,89) /1008,63	(0,0403+0,0514)/ 0,1127	0,81366	(1538,65+1644,32) /1007,97	(0,0325+0,0361)/ 0,1344	0,51042	(1538,55+1634,7)/ 1013,66	(0,0533+0,0676)/ 0,0929	1,3014
Amides + Collagen to phosphates	(1205+1238,76+ 1280+1634,89+ 1539,82)/1008,63	(0,0068+0,0174+ 0,0106+0,0514+ 0,0403)/0,1127	1,12245	(1205+1240+1282+ 1644,32+1538,65)/ 1007,97	(0,0015+0,0078+ 0,0055+0,0361+ 0,0325)/0,1344	0,62054	(1205+1237+1280+ 1634,7+1538,55)/ 1013,66	(0,0113+0,0226+ 0,0144+0,0676+ 0,0533)/0,0929	1,82131
Carbonate accumulation	871,37/1634,89	0,0217/0,0514	0,42218	871/1644,32	0,0295/0,0361	0,81717	871,46/1634,7	0,0175/0,0676	0,25888
Crystallinity	1 /FWHM of 1008,63	1 /111,426336	0,00897	1 /FWHM of 1007,97	1/ 116,615916	0,00858	1 /FWHM of 1013,66	1/ 110,940395	0,00901
Mineral to matrix ratio	1008,63/1634,89	0,1127/0,0514	2,19261	1007,97/1644,32	0,1344/0,0361	3,72299	1013,66/1634,7	0,0929/0,0676	1,37426
Mineral maturity	1008,63/1104	0,1127/0,0377	2,98939	1007,97/1101	0,1344/0,0418	3,21531	1013,66/1104	0,0929/0,0328	2,83232

Secondary structure of proteins	1634,89/1238,76	0,0514/0,0174	2,95402	1644,32/1240	0,0361/0,0078	4,62821	1634,7/1236,95	0,0676/0,0226	2,99115
		#6 Base			**#6 Tibia**			**#6 Tip**	
Parameter	**cm-1**	**Intensity ratio**	**Result**	**cm-1**	**Intensity ratio**	**Result**	**cm-1**	**Intensity ratio**	**Result**
Amide I to phosphate	1633,33/1012,62	0,0366/0,0489	0,74847	1644,94/1011,46	0,1387/0,547	0,25356	1633,8/1018,96	0,0948/0,0869	1,09091
Amide II to phosphate	1540,56/1012,62	0,0301/0,0489	0,61554	1549,75/1011,46	0,1083/0,547	0,19799	1547,96/1018,96	0,0756/0,0869	0,86997
Amide III + Collagen to phosphate	(1201+1240+1278) /1012,62	(0,0053+0,0128+ 0,0093)/0,0489	0,56033	(1204+1240,07+ 1281)/1011,46	(0,0099+0,0357+ 0,0214)/0,547	0,12249	(1205+1237,15+ 1280)/1018,96	(0,0179+0,0342+ 0,0211)/0,0869	0,84235
Amide I + Amide II to phosphate	(1540,56+1633,33) /1012,62	(0,0301+0,0366)/ 0,0489	1,36401	(1549,75+1644,94) /1011,46	(0,1083+0,1387)/ 0,547	0,45155	(1547,96+1633,8)/ 1018,96	(0,0756+0,0948)/ 0,0869	1,96087
Amides + Collagen to phosphates	(1201+1240+1278+ 1633,33+1540,56)/ 1012,62	(0,0053+0,0128+ 0,0093+0,0366+ 0,0301)/0,0489	1,92434	(1204+1240,07+ 1281+1644,94+ 1549,75)/1011,46	(0,0099+0,0357+ 0,0214+0,1387+ 0,1083)/0,547	0,57404	(1205+1237,15+ 1280+1633,8+ 1547,96)/1018,96	(0,0179+0,0342+ 0,0211+0,0948+ 0,0756)/0,0869	2,80322
Carbonate accumulation	871/1633,33	0,0082/0,0366	0,22404	871,47/1644,94	0,0839/0,1387	0,6049	871,55/1633,8	0,013/0,0948	0,13713
Crystallinity	1/FWHM of 1012,62	1/127,125878	0,0078	1/FWHM of 1011,46	1/89,137741	0,01122	1/FWHM of 1018,96	1/108,904984	0,00918
Mineral to matrix ratio	1012,62/1633,33	0,0489/0,0366	1,33607	1011,46/1644,94	0,547/0,1387	3,94376	1018,96/1633,8	0,0869/0,0948	0,91667
Mineral maturity	1012,62/1103	0,0489/0,0182	2,68681	1011,46/1103	0,547/0,1599	3,42089	1018,96/1102	0,0869/0,0326	2,66564
Secondary structure of proteins	1633,33/1240	0,0366/0,0128	2,85938	1644,94/1240,07	0,1387/0,0357	3,88515	1633,8/1237,15	0,0948/0,0342	2,77193
		#7 Base			**#7 Tibia**			**#7 Tip**	
Parameter	**cm-1**	**Intensity ratio**	**Result**	**cm-1**	**Intensity ratio**	**Result**	**cm-1**	**Intensity ratio**	**Result**
Amide I to phosphate	1636,12/1011,61	0,0557/0,133	0,4188	1650,9/1006,31	0,0618/0,2231	0,27701	1634,09/1012,54	0,0739/0,1118	0,661
Amide II to phosphate	1548,72/1011,61	0,0435/0,133	0,32707	1549,46/1006,31	0,0484/0,2231	0,21694	1547,89/1012,54	0,0592/0,1118	0,52952
Amide III + Collagen to phosphate	(1205+1239,17+ 1279)/1011,61	(0,0077+0,019+ 0,0122)/0,133	0,29248	(1204+1241+1283) /1006,31	(0,0028+0,0133+ 0,0082)/0,2231	0,10892	(1204+1237,94+ 1280)/1012,54	(0,0113+0,0249+ 0,0155)/0,1118	0,46243
Amide I + Amide II to phosphate	(1548,72+1636,12) /1011,61	(0,0435+0,0557)/ 0,133	0,74586	(1549,46+1650,9)/ 1006,31	(0,0484+0,0618)/ 0,2231	0,49395	(1547,89+1634,09) /1012,54	(0,0592+0,0739)/ 0,1118	1,19059
Amides + Collagen to phosphates	(1205+1239,17+ 1279+1636,12+ 1548,72)/1011,61	(0,0077+0,019+ 0,0122+0,0557+ 0,0435)/0,133	1,03835	(1204+1241+1283+ 1650,9+1549,46)/ 1006,31	(0,0028+0,0133+ 0,0082+0,0618+ 0,0484)/0,2231	0,60287	(1204+1237,94+ 1280+1634,09+ 1547,89)/1012,54	(0,0113+0,0249+ 0,0155+0,0739+ 0,0592)/0,1118	1,65295

Carbonate accumulation	871,6/1636,12	0,0219/0,0557	0,39318	871,09/1650,9	0,0505/0,0618	0,81715	871,39/1634,09	0,0158/0,0739	0,2138
Crystallinity	1/FWHM of 1011,61	1/97,280823	0,01028	1/FWHM of 1006,31	1/120,082454	0,00833	1/FWHM of 1012,54	1/96,37596	0,01038
Mineral to matrix ratio	1011,61/1636,12	0,133/0,0557	2,38779	1006,31/1650,9	0,2231/0,0618	3,61003	1012,54/1634,09	0,1118/0,0739	1,51286
Mineral maturity	1011,61/1103	0,133/0,0438	3,03653	1006,31/1102	0,2231/0,07	3,18714	1012,54/1103	0,1118/0,0382	2,92670
Secondary structure of proteins	1636,12/1239,17	0,0557/0,019	2,93158	1650,9/1241	0,0618/0,0133	4,64662	1634,09/1237,94	0,0739/0,0249	2,96787
		#8 Base			**#8 Tibia**			**#8 Tip**	
Parameter	**cm-1**	**Intensity ratio**	**Result**	**cm-1**	**Intensity ratio (based on height)**	**Result**	**cm-1**	**Intensity ratio**	**Result**
Amide I to phosphate	1643,52/1011,52	0,0735/0,214	0,34346	1642,99/1007,06	0,0359/0,1505	0,23854	1635,49/1011,48	0,0709/0,1359	0,52171
Amide II to phosphate	1548,95/1011,52	0,0576/0,214	0,26916	1546/1007,06	0,03/0,1505	0,19934	1548,9/1011,48	0,0555/0,1359	0,40839
Amide III + Collagen to phosphate	(1204+1238,83+ 1280)/1011,52	(0,0067+0,0214+ 0,0124)/0,214	0,18925	(1205+1240+1283) /1007,06	(0,0016+0,0086+ 0,0053)/0,1505	0,10299	(1205+1239,15+ 1281)/1011,48	(0,0077+0,0214+ 0,0134)/0,1359	0,31273
Amide I + Amide II to phosphate	(1548,95+1643,52) /1011,52	(0,0576+0,0735)/ 0,214	0,6126	(1546+1642,99)/ 1007,06	(0,03+0,0359)/0,1505	0,43787	(1548,9+1635,49)/ 1011,48	(0,0555+0,0709)/ 0,1359	0,9301
Amides + Collagen to phosphates	(1204+1238,83+ 1280+1643,52+ 1548,95)/1011,52	(0,0067+0,0214+ 0,0124+0,0735+ 0,0576)/0,214	0,80187	(1205+1240+1283+ 1642,99+1546)/ 1007,06	(0,0016+0,0086+ 0,0053+0,0359+0,03) /0,1505	0,54086	(1205+1239,15+ 1281+1635,49+ 1548,9)/1011,48	(0,0077+0,0214+ 0,0134+0,0709+ 0,0555)/0,1359	1,24283
Carbonate accumulation	871,5/1643,52	0,0331/0,0735	0,4503	870,84/1642,99	0,0305/0,0359	0,84958	871,61/1635,49	0,0212/0,0709	0,29901
Crystallinity	1/FWHM of 1011,52	1/93,608844	0,01068	1/FWHM of 1007,06	1/112,543232	0,0088	1/FWHM of 1011,48	1/97,30184	0,01028
Mineral to matrix ratio	1011,52/1643,52	0,214/0,0735	2,91156	1007,06/1642,99	0,1505/0,0359	4,19220	1011,48/1635,49	0,1359/0,0709	1,91678
Mineral maturity	1011,52/1103	0,214/0,0682	3,13783	1007,06/1103	0,1505/0,044	3,42045	1011,48/1103	0,1359/0,0449	3,02673
Secondary structure of proteins	1643,52/1238,83	0,0735/0,0214	3,43458	1642,99/1240	0,0359/0,0086	4,17442	1635,49/1239,15	0,0709/0,0214	3,31308
		#9 Base			**#9 Tibia**			**#9 Tip**	
Parameter	**cm-1**	**Intensity ratio**	**Result**	**cm-1**	**Intensity ratio**	**Result**	**cm-1**	**Intensity ratio**	**Result**
Amide I to phosphate	1650,93/1010,65	0,075/0,2517	0,29797	1643,56/1011,25	0,0519/0,2055	0,25255	1632,59/1013,77	0,0607/0,0724	0,8384
Amide II to phosphate	1549,66/1010,65	0,0616/0,2517	0,24474	1549/1011,25	0,0376/0,2055	0,18297	1548,22/1013,77	0,0483/0,0724	0,66713

Amide III + Collagen to phosphate	(1204+1238,81+ 1281)/1010,65	(0,0054+0,0221+ 0,0112/0,2517	0,15375	(1204+1240+1284) /1011,25	(0,0061+0,0145+ 0,0104)/0,2055	0,15085	(1204+1236,43+ 1280)/1013,77	(0,01+0,0205+ 0,0128)/0,0724	0,59807
Amide I + Amide II to phosphate	(1549,66+1650,93) /1010,65	(0,0616+0,075)/ 0,2517	0,54271	(1549+1643,56)/ 1011,25	(0,0376+0,0519)/ 0,2055	0,43552	(1548,22+1632,59) /1013,77	(0,0483+0,0607)/ 0,0724	1,50552
Amides + Collagen to phosphates	(1204+1238,81+ 1281+1650,93+ 1549,66)/1010,65	(0,0054+0,0221+ 0,0112+0,075+ 0,0616)/0,2517	0,69646	(1204+1240+1284+ 1643,56+1549)/ 1011,25	(0,0061+0,0145+ 0,0104+0,0519+ 0,0376)/0,2055	0,58637	(1204+1236,43+ 1280+1632,59+ 1548,22)/1013,77	(0,01+0,0205+ 0,0128+0,0607+ 0,0483)/0,0724	2,10359
Carbonate accumulation	871,43/1650,93	0,0373/0,075	0,49733	871,08/1643,56	0,0417/0,0519	0,80347	872/1632,59	0,0099/0,0607	0,1631
Crystallinity	1/FWHM of 1010,65	1/91,972784	0,01087	1/FWHM of 1011,25	1/107,841701	0,00927	1/FWHM of 1013,77	1/95,405167	0,01048
Mineral to matrix ratio	1010,65/1650,93	0,2517/0,075	3,356	1011,25/1643,56	0,2055/0,0519	3,95954	1013,77/1632,59	0,0724/0,0607	1,19275
Mineral maturity	1010,65/1103	0,2517/0,0751	3,35153	1011,25/1103	0,2055/0,0669	3,07175	1013,77/1102	0,0724/0,0252	2,87302
Secondary structure of proteins	1650,93/1238,81	0,075/0,0221	3,3936	1643,56/1240	0,0519/0,0145	3,57931	1632,59/1236,43	0,0607/0,0205	2,96098
		Control							
Parameter	**cm-1**	**Intensity ratio**	**Result**						
Amide I to phosphate	1639,94/1009,73	0,0367/0,0957	0,38349						
Amide II to phosphate	1544,04/1009,73	0,0252/0,0957	0,26332						
Amide III + Collagen to phosphate	(1204+1238+1281) /1009,73	(-0,0018+0,0057+ 0,0008)/0,0957	0,04911						
Amide I + Amide II to phosphate	(1544,04+1639,94) /1009,73	(0,0252+0,0367)/0, 0957	0,64681						
Amides + Collagen to phosphates	(1204+1238+1281+ 1639,94+1544,04)/ 1009,73	(-0,0018+0,0057+ 0,0008+0,0367+ 0,0252)/0,0957	0,69592						
Carbonate accumulation	871,6/1639,94	0,0151/0,0367	0,41144						
Crystallinity	1/FWHM of 1009,73	1/97,040594	0,0103						
Mineral to matrix ratio	1009,73/1639,94	0,0957/0,0367	2,60763						
Mineral maturity	1009,73/1101	0,0957/0,0281	3,40569						
Secondary structure of proteins	1639,94/1238	0,0367/0,0057	6,438						

Appendix 10. FTIR parameter calculations based on the measurements obtained with PerkinElmer Spectrum 100 at the Tokyo Medical and Dental University.

	#1 Base			#1 Tibia			#1 Tip		
Parameter	**cm-1**	**Intensity ratio**	**Result**	**cm-1**	**Intensity ratio**	**Result**	**cm-1**	**Intensity ratio**	**Result**
Carbonate content of bioapatite	1406/598	0,06927/0,11183	0,61939	1416/598	0,07949/0,15725	0,50547	1413/596	0,04499/0,05289	0,85075
Carbonate to mineral ratio	871/(556+598+1010)	0,0386/(0,21235+0,11183+0,23291)	0,06928	871/(554+598+1006)	0,06483/(0,31496+0,15725+0,30419)	0,0835	871/(556+596+1009)	0,02316/(0,09549+0,05289+0,116)	0,08762
Crystallinity index CI	(598+556)/587	(0,11183+0,21235)/0,08631	3,75585	(598+554)/587	(0,15725+0,31496)/0,13054	3,61732	(596+556)/589	(0,05289+0,09549)/0,04615	3,21536
Mineral maturity	598/556	0,11183/0,21235	0,52664	598/554	0,15725/0,31496	0,49927	596/556	0,05289/0,09549	0,55382
Mineral to matrix ratio	(556+598)/1635	(0,21235+0,11183)/0,10303	3,14658	(554+598)/1643	(0,31496+0,15725)/0,05706	8,27586	(556+596)/1640	(0,09549+0,05289)/0,05376	2,75989
	#2 Base			**#2 Tibia**			**#2 Tip**		
Parameter	**cm-1**	**Intensity ratio**	**Result**	**cm-1**	**Intensity ratio**	**Result**	**cm-1**	**Intensity ratio**	**Result**
Carbonate content of bioapatite	1409/598	0,04261/0,07333	0,58102	1408/600	0,08742/0,13492	0,64798	1407/597	0,03714/0,04164	0,89195
Carbonate to mineral ratio	871/(556+598+1010)	0,02144/(0,13841+0,07333+0,1297)	0,0628	871/(555+600+1008)	0,05326/(0,25575+0,13492+0,29102)	0,07813	873/(555+597+1011)	0,01502/(0,07594+0,04164+0,09026)	0,07226
Crystallinity index CI	(598+556)/585	(0,07333+0,13841)/0,06199	3,41585	(600+555)/589	(0,13492+0,25575)/0,1081	3,61382	(597+555)/586	(0,04164+0,07594)/0,03403	3,45477
Mineral maturity	598/556	0,07333/0,13841	0,52978	600/555	0,13492/0,25575	0,52752	597/555	0,04164/0,07594	0,54839
Mineral to matrix ratio	(556+598)/1635	(0,13841+0,07333)/0,0595	3,55877	(555+600)/1635	(0,25575+0,13492)/0,10274	3,80244	(555+597)/1632	(0,07594+0,04164/0,06115	1,922889
	#3 Base			**#3 Tibia**			**#3 Tip**		
Parameter	**cm-1**	**Intensity ratio**	**Result**	**cm-1**	**Intensity ratio**	**Result**	**cm-1**	**Intensity ratio**	**Result**
Carbonate content of bioapatite	1407/598	0,07543/0,10119	0,7455	1408/598	0,11039/0,18682	0,59091	1408/600	0,04092/0,04852	0,84349
Carbonate to mineral ratio	872/(555+598+1010)	0,03513/(0,1913+0,10119+0,21711)	0,06893	871/(556+598+1008)	0,0666/(0,33835+0,18682+0,39921)	0,07205	872/(555+600+1010)	0,02283/(0,09281+0,04852+0,11535)	0,08895
Crystallinity index CI	(598+555)/587	(0,10119+0,1913)/0,08352	3,50209	(598+556)/587	(0,18682+0,33835)/0,1557	3,37293	(600+555)/586	(0,04852+0,09281)/0,04275	3,30583
Mineral maturity	598/555	0,10119/0,1913	0,52895	598/556	0,18682/0,33835	0,55216	600/555	0,04852/0,09281	0,52276

Mineral to matrix ratio	(555+598)/ 1638	(0,1913+0,10119)/ 0,11251	2,59966	(556+598)/ 1642	(0,33835+0,18682)/ 0,12796	4,10405	(555+600)/ 1636	(0,09281+0,04852) /0,06222	2,27138
		#4 Base			**#4 Tibia**			**#4 Tip**	
Parameter	**cm-1**	**Intensity ratio**	**Result**	**cm-1**	**Intensity ratio**	**Result**	**cm-1**	**Intensity ratio**	**Result**
Carbonate content of bioapatite	1404/599	0,09312/0,16242	0,57335	1410/599	0,10559/0,16084	0,6565	1405/599	0,0529/0,04872	1,08579
Carbonate to mineral ratio	872/(555+599+ 1007)	0,06075/(0,30935+ 0,16242+0,33231)	0,07555	872/(555+599+ 1007)	0,0708/(0,32865+ 0,16084+0,363)	0,08305	872/(555+599+ 1016)	0,01899/(0,09427+ 0,04872+0,11651)	0,07317
Crystallinity index CI	(599+555)/587	(0,16242+0,30935)/ 0,13187	3,57746	(599+555)/587	(0,16084+0,32865)/ 0,13066	3,74641	(599+555)/587	(0,04872+0,09427) /0,04058	3,52317
Mineral maturity	599/555	0,16242/0,30935	0,52504	599/555	0,16084/0,32865	0,48941	599/555	0,04872/0,09427	0,51678
Mineral to matrix ratio	(555+599)/ 1636	(0,30935+0,16242)/ 0,12267	3,84578	(555+599)/ 1643	(0,32865+0,16084)/ 0,09742	5,02448	(555+599)/ 1635	(0,09427+0,04872) /0,09361	1,52754
		#5 Base			**#5 Tibia**			**#5 Tip**	
Parameter	**cm-1**	**Intensity ratio**	**Result**	**cm-1**	**Intensity ratio**	**Result**	**cm-1**	**Intensity ratio**	**Result**
Carbonate content of bioapatite	1408/598	0,055/0,08077	0,681	1409/597	0,05025/0,08264	0,60809	1409/598	0,0334/0,03705	0,90162
Carbonate to mineral ratio	871/(556+598+ 1012)	0,02716/(0,15462+ 0,08077+0,1592)	0,06883	871/(555+597+ 1004)	0,03116/(0,15477+ 0,08264+0,14927)	0,08058	873/(554+598+ 1016)	0,01431/(0,06772+ 0,03705+0,07654)	0,07893
Crystallinity index CI	(598+556)/589	(0,08077+0,15462)/ 0,07042	3,34272	(597+555)/589	(0,08264+0,15477)/ 0,06767	3,50835	(598+554)/588	(0,03705+0,06772) /0,02735	3,83146
Mineral maturity	598/556	0,08077/0,15462	0,52236	597/555	0,08264/0,15477	0,53392	598/554	0,03705/0,06772	0,54705
Mineral to matrix ratio	(556+598)/ 1634	(0,15462+0,08077)/ 0,08327	2,82677	(555+597)/ 1641	(0,15477+0,08264)/ 0,05701	4,16403	(554+598)/ 1633	(0,06772+0,03705) /0,05799	1,80688
		#6 Base			**#6 Tibia**			**#6 Tip**	
Parameter	**cm-1**	**Intensity ratio**	**Result**	**cm-1**	**Intensity ratio**	**Result**	**cm-1**	**Intensity ratio**	**Result**
Carbonate content of bioapatite	1408/596	0,03845/0,05496	0,69962	1408/599	0,06143/0,10179	0,60349	1404/595	0,05377/0,04665	1,15273
Carbonate to mineral ratio	871/(555+596+ 1008)	0,01539/(0,10317+ 0,05496+0,09424)	0,06098	872/(555+599+ 1007)	0,03517/(0,19226+ 0,10179+0,193)	0,0722	871/(554+595+ 1017)	0,01153/(0,07644+ 0,04665+0,08453)	0,05555
Crystallinity index CI	(596+555)/589	(0,05496+0,10317)/ 0,04523	3,49603	(599+555)/589	(0,10179+0,19226)/ 0,08544	3,44174	(595+554)/588	(0,04665+0,07644) /0,03689	3,33627
Mineral maturity	596/555	0,05496/0,10317	0,53271	599/555	0,10179/0,19226	0,52945	595/554	0,04665/0,07644	0,61029
Mineral to matrix ratio	(555+596)/ 1635	(0,10317+0,05496)/ 0,05307	2,97966	(555+599)/ 1634	(0,19226+0,10179) /0,06695	4,39178	(554+595)/ 1634	(0,07644+0,04665) /0,09834	1,25173
		#7 Base			**#7 Tibia**			**#7 Tip**	

Parameter	cm-1	Intensity ratio	Result	cm-1	Intensity ratio	Result	cm-1	Intensity ratio	Result
Carbonate content of bioapatite	1407/597	0,05111/0,07334	0,69696	1407/599	0,06343/0,13674	0,46388	1408/599	0,04243/0,04188	1,01312
Carbonate to mineral ratio	871/(555+597+1007)	0,0264/(0,13718+0,07334+0,14544)	0,0742	872/(555+599+1006)	0,05891/(0,2563+0,13674+0,23592)	0,09366	874/(555+599+1012)	0,01763/(0,07772+0,04188+0,11216)	0,07605
Crystallinity index CI	(597+555)/589	(0,07334+0,13718)/0,06135	3,43155	(599+555)/588	(0,13674+0,2563)/0,11538	3,40651	(599+555)/589	(0,04188+0,07772)/0,03422	3,49491
Mineral maturity	597/555	0,07334/0,13718	0,53458	599/555	0,13674/0,2563	0,53352	599/555	0,04188/0,07772	0,53889
Mineral to matrix ratio	(555+597)/1637	(0,13718+0,07334)/0,07409	2,8413	(555+599)/1635	(0,2562+0,13674)/0,05391	7,29029	(555+599)/1633	(0,07772+0,04188)/0,06884	1,73721
	#8 Base			**#8 Tibia**			**#8 Tip**		
Parameter	**cm-1**	**Intensity ratio**	**Result**	**cm-1**	**Intensity ratio (based on height)**	**Result**	**cm-1**	**Intensity ratio**	**Result**
Carbonate content of bioapatite	1408/598	0,0684/0,08993	0,7606	1410/598	0,06001/0,09197	0,65246	1408/599	0,05578/0,0624	0,89394
Carbonate to mineral ratio	871/(557+598+1010)	0,03359/(0,16989+0,08993+0,19035)	0,07461	872/(556+598+1007)	0,03913/(0,17415+0,09197+0,18479)	0,08678	872/(555+599+1007)	0,02615/(0,10557+0,0624+0,14569)	0,08338
Crystallinity index CI	(598+557)/586	(0,08993+0,16989)/0,74509	0,34871	(598+556)/589	(0,09197+0,17415)/0,07401	3,59573	(599+555)/587	(0,0624+0,10557)/0,04679	3,58961
Mineral maturity	598/557	0,08993/0,16989	0,52935	598/556	0,09197/0,17415	0,52811	599/555	0,0624/0,10557	0,59111
Mineral to matrix ratio	(557+598)/1635	(0,16989+0,08993)/0,09644	2,69408	(556+598)/1640	(0,17415+0,09197)/0,06258	4,2528	(555+599)/1635	(0,10557+0,0624)/0,08456	1,98642
	#9 Base			**#9 Tibia**			**#9 Tip**		
Parameter	**cm-1**	**Intensity ratio**	**Result**	**cm-1**	**Intensity ratio**	**Result**	**cm-1**	**Intensity ratio**	**Result**
Carbonate content of bioapatite	1409/599	0,05648/0,0976	0,57871	1409/597	0,09479/0,17147	0,5528	1408/597	0,05066/0,07145	0,70909
Carbonate to mineral ratio	872/(555+599+1012)	0,03356/(0,18113+0,0976+0,19094)	0,07145	871/(556+597+1008)	0,06438/(0,33831+0,17147+0,35661)	0,07431	871/(555+597+1011)	0,02234/(0,12604+0,07145+0,14547)	0,06513
Crystallinity index CI	(599+555)/587	(0,0976+0,18113)/0,08241	3,3824	(597+556)/587	(0,17147+0,33831)/0,14274	3,57144	(597+555)/588	(0,07145+0,12604)/0,05956	3,31605
Mineral maturity	599/555	0,0976/0,18113	0,53887	597/556	0,17147/0,33831	0,50683	597/555	0,07145/0,12604	0,56688
Mineral to matrix ratio	(555+599)/1635	(0,18113+0,0976)/0,0705	3,95349	(556+597)/1635	(0,33831+0,17147)/0,10753	4,74082	(555+597)/1634	(0,12604+0,07145)/0,07417	2,66272
	Control								
Parameter	**cm-1**	**Intensity ratio**	**Result**						

Carbonate content of bioapatite	1410/599	0,0626/0,08592	0,72865	
Carbonate to mineral ratio	872/(557+599+1009)	0,03667/(0,16056+0,08592+0,17114)	0,08781	
Crystallinity index CI	(599+557)/586	(0,08592+0,16056)/0,07257	3,39655	
Mineral maturity	599/557	0,08592/0,16056	0,53512	
Mineral to matrix ratio	(557+599)/1634	(0,16056+0,08592)/0,08398	2,93503	

Appendix 11. Manual Full width at half maximum (FWHM) of the peak at 1011cm^{-1} from the Frontier IR measurements.

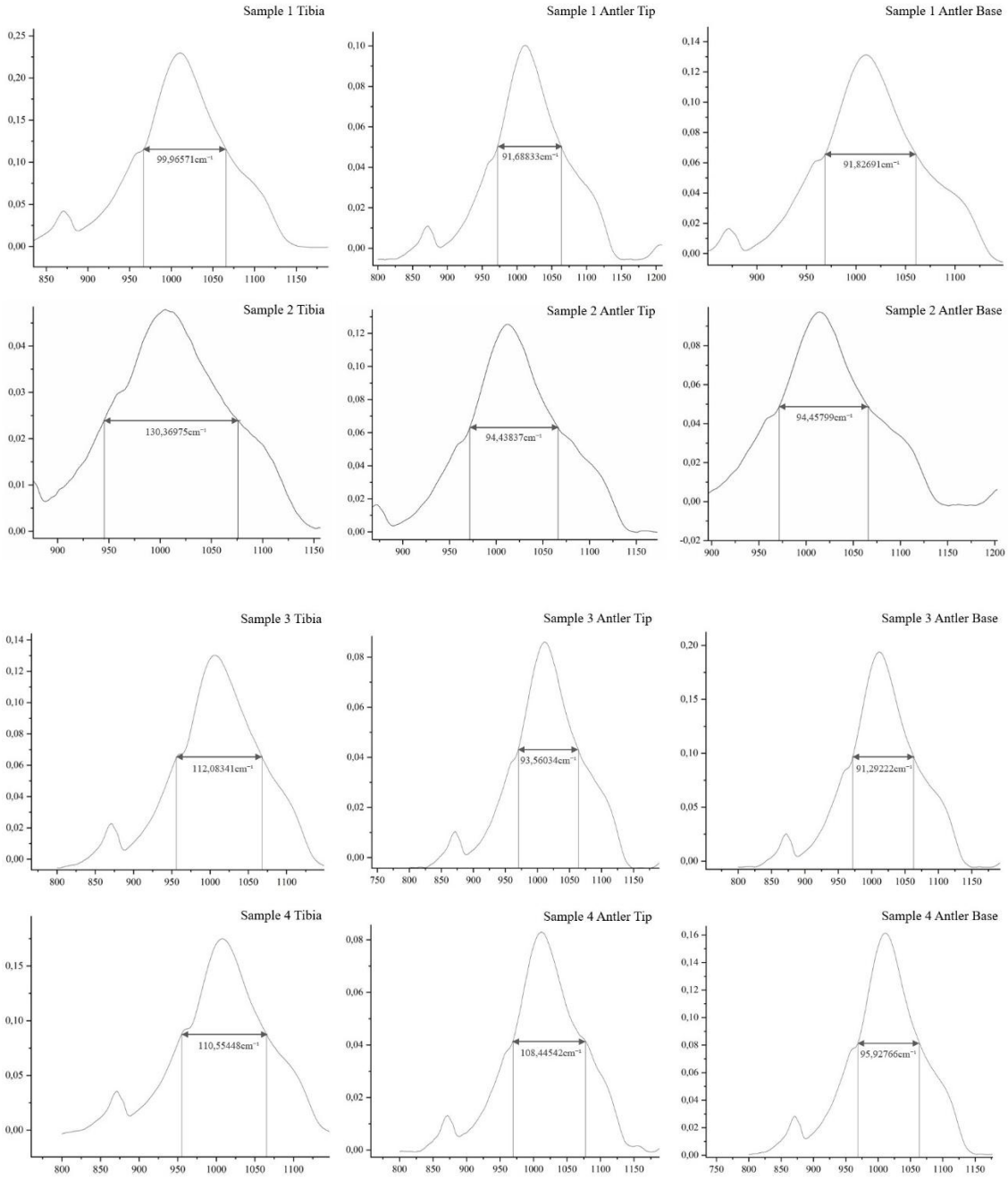

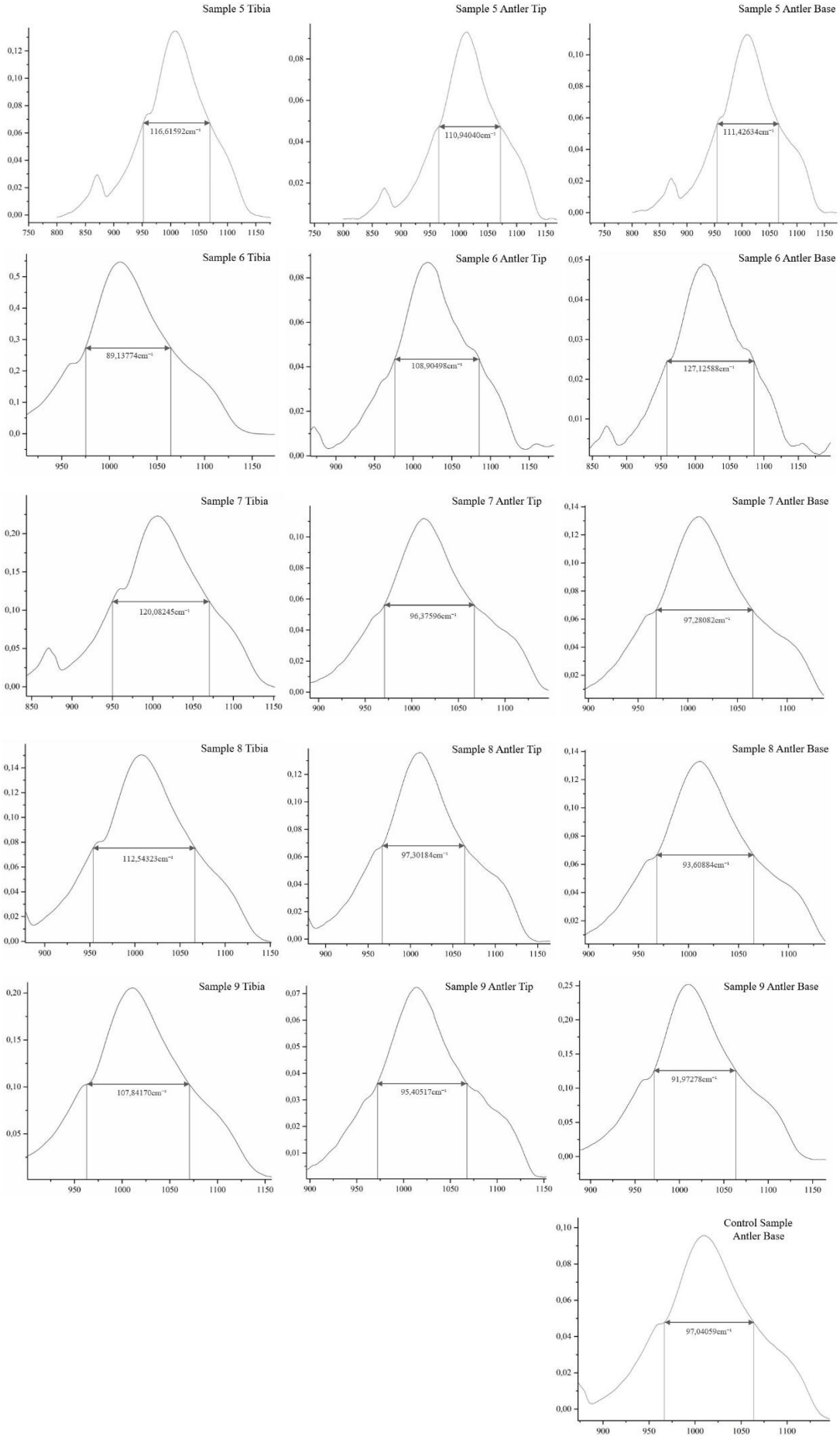
Sample 5 Tibia
116,61592cm⁻¹
Sample 5 Antler Tip
110,94040cm⁻¹
Sample 5 Antler Base
111,42634cm⁻¹
Sample 6 Tibia
89,13774cm⁻¹
Sample 6 Antler Tip
108,90498cm⁻¹
Sample 6 Antler Base
127,12588cm⁻¹
Sample 7 Tibia
120,08245cm⁻¹
Sample 7 Antler Tip
96,37596cm⁻¹
Sample 7 Antler Base
97,28082cm⁻¹
Sample 8 Tibia
112,54323cm⁻¹
Sample 8 Antler Tip
97,30184cm⁻¹
Sample 8 Antler Base
93,60884cm⁻¹
Sample 9 Tibia
107,84170cm⁻¹
Sample 9 Antler Tip
95,40517cm⁻¹
Sample 9 Antler Base
91,97278cm⁻¹
Control Sample
Antler Base
97,04059cm⁻¹

Appendix 12. 2D and 3D micro-CT images of the analysed samples.

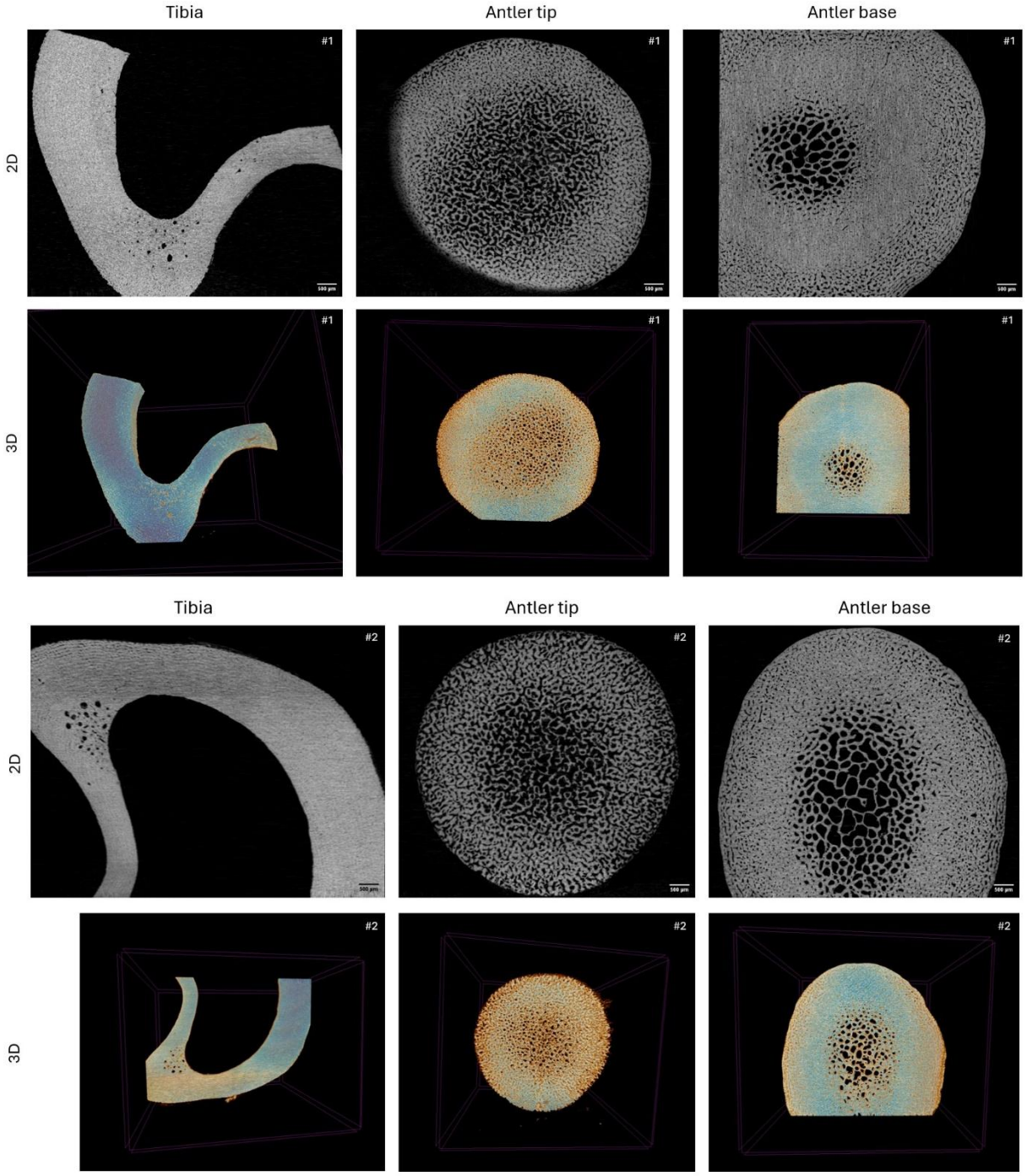

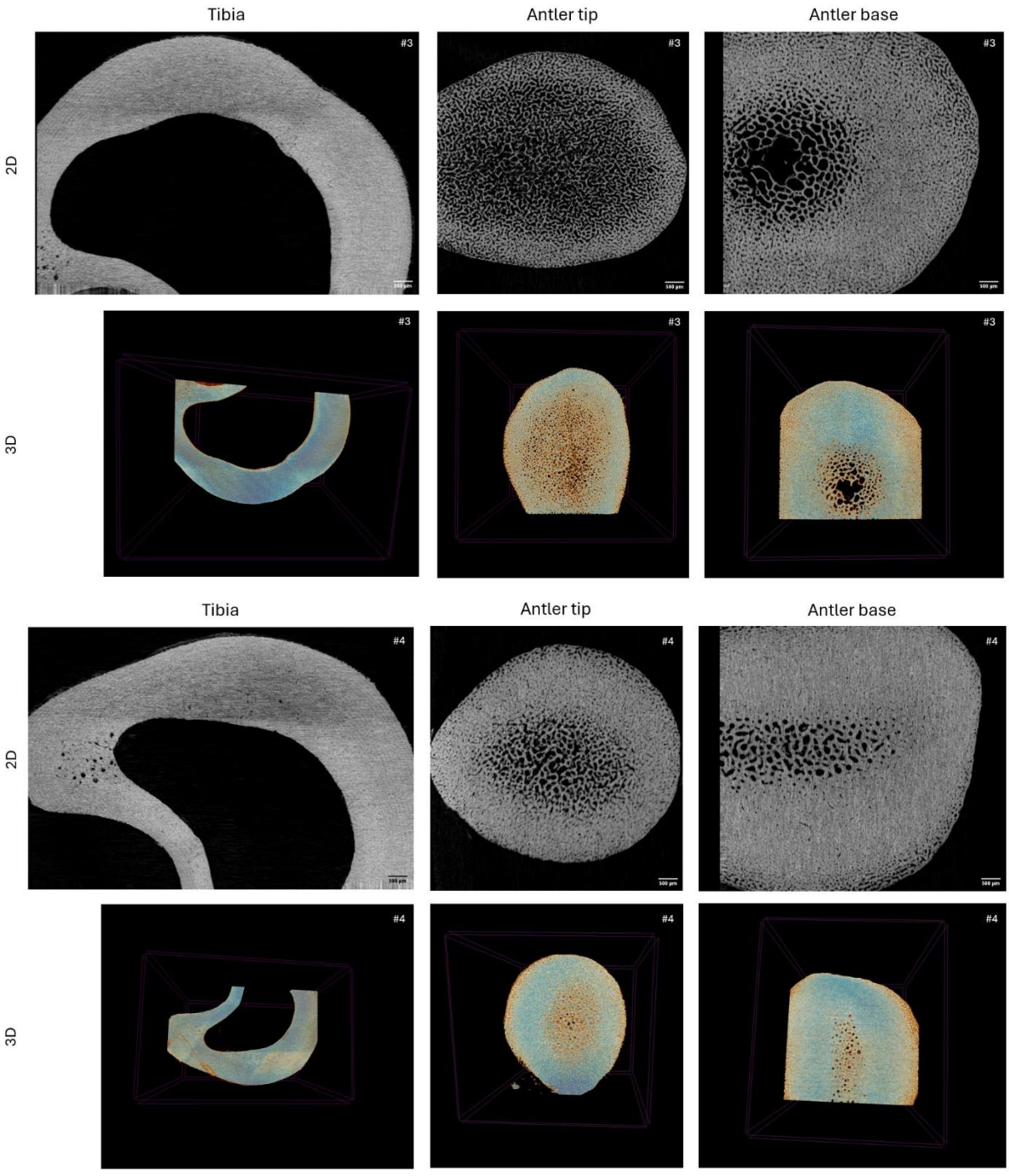
Tibia
Antler tip
Antler base
2D
3D
#3
#4

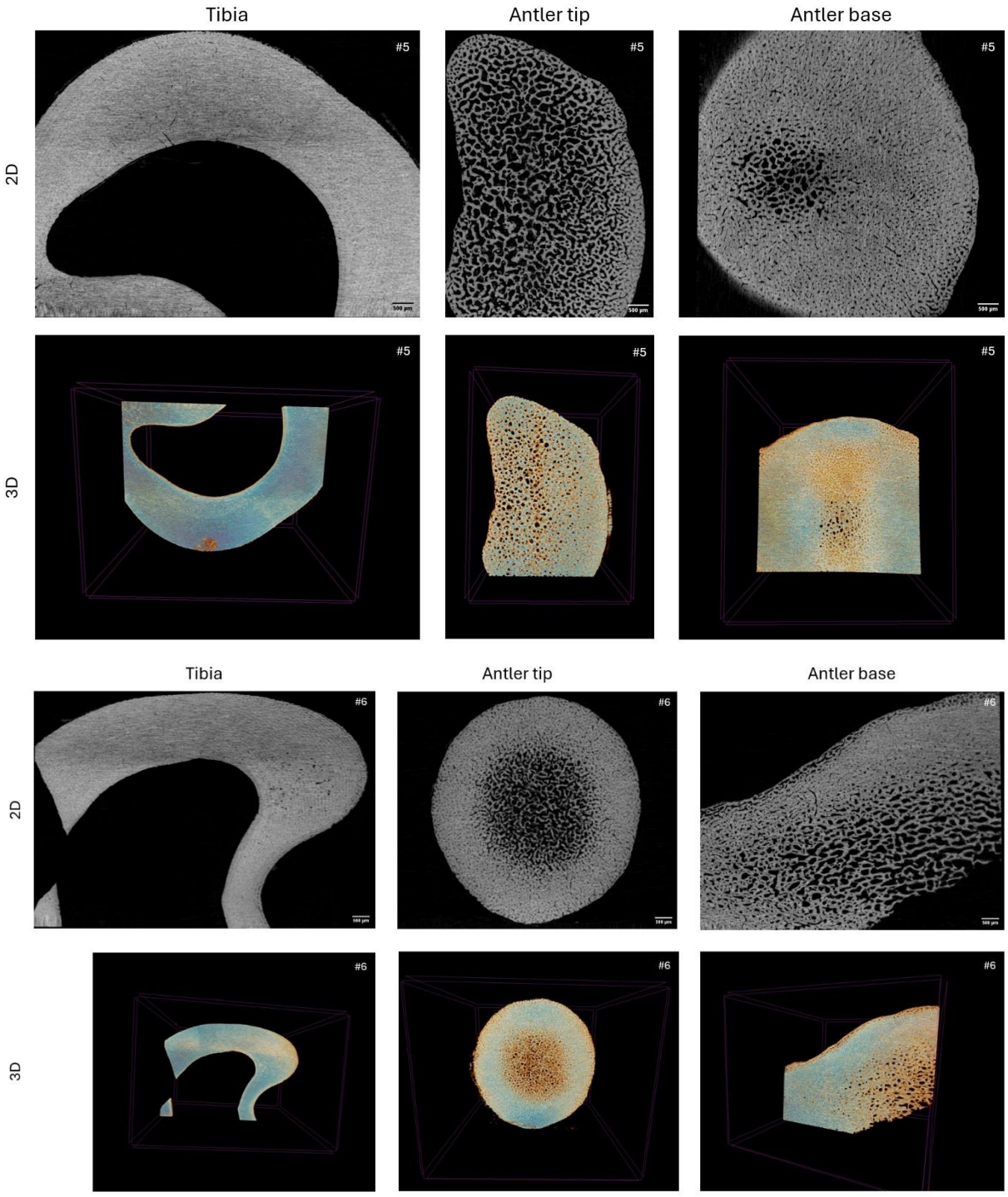
Tibia
Antler tip
Antler base
2D
3D
#5
#5
#5
#5
#5
#5
Tibia
Antler tip
Antler base
2D
3D
#6
#6
#6
#6
#6
#6

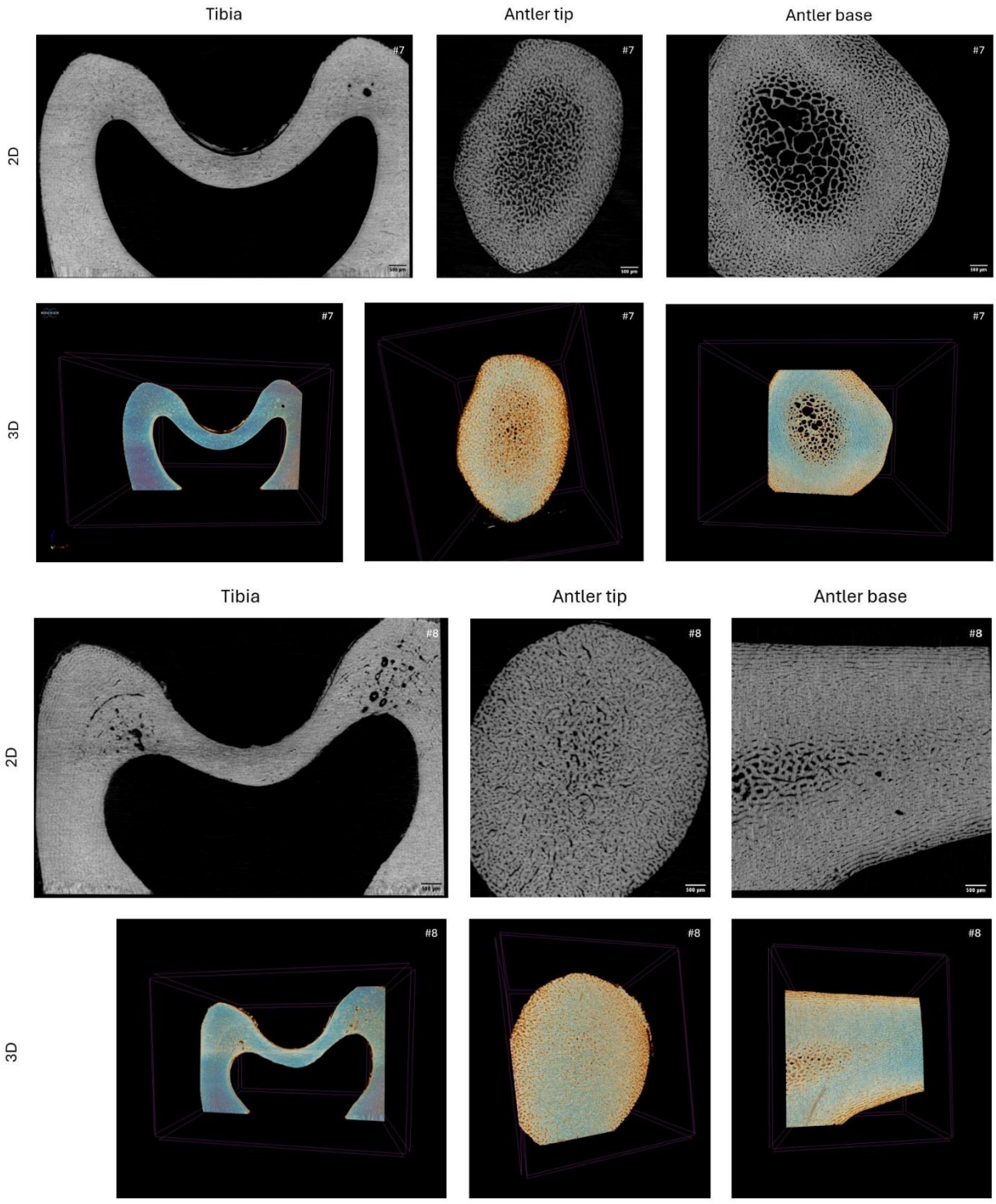
Tibia
Antler tip
Antler base
2D
3D
#7
#8

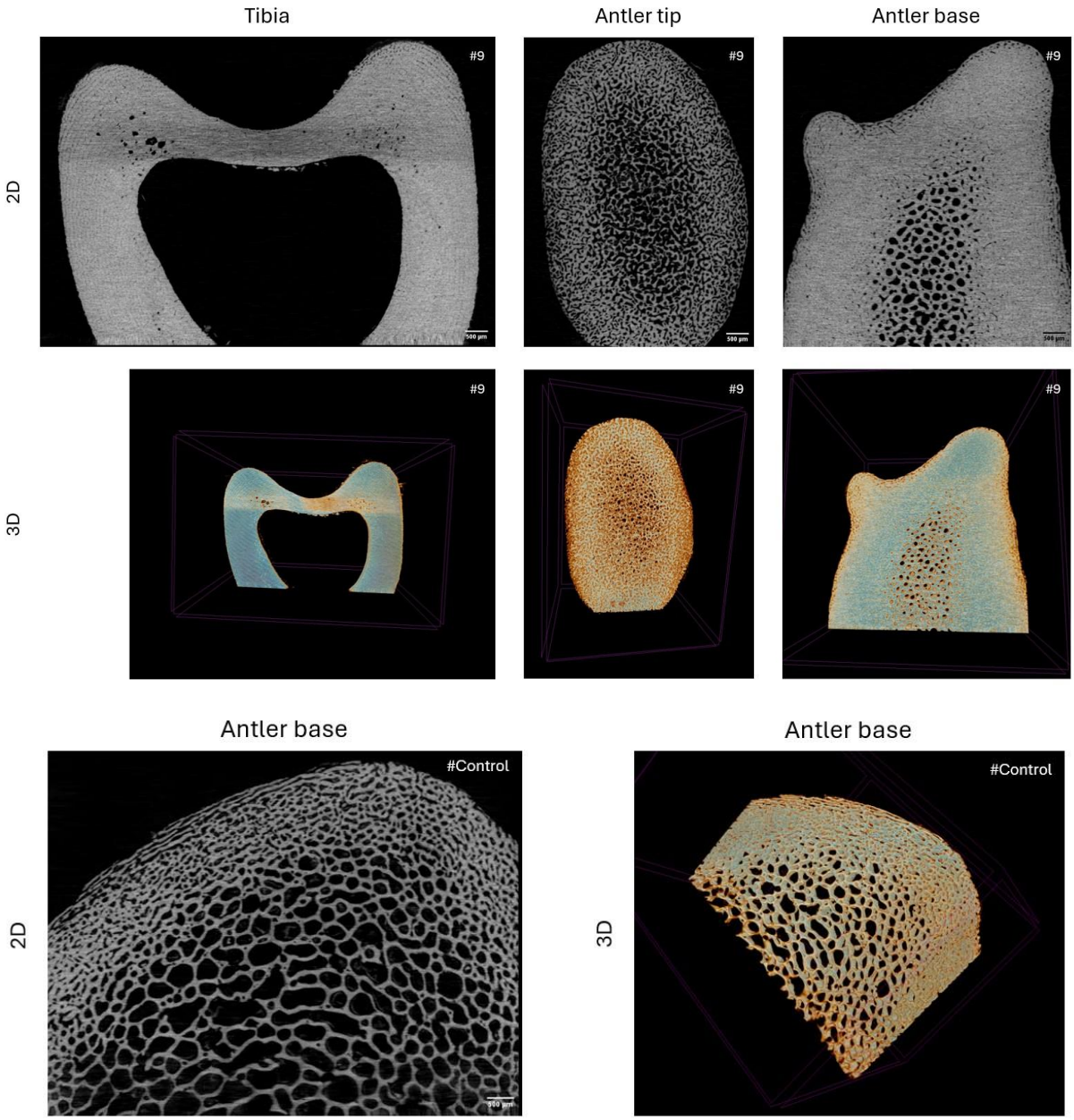
Tibia
Antler tip
Antler base
2D
3D
#9
Antler base
Antler base
2D
3D
#Control

Appendix 13. Micro-CT Parameter Values (individual means per region).

ID	Bone	Region	BMD (ROI n=4)		Po(cl) (ROI n=4)		Po(op) (ROI n=4)		Po(tot) (ROI n=4)		BV/TV(ROI n=4)		Tb.N (ROI n=4)		Tb.Th (ROI n=4)		Tb.Sp (ROI n=4)	
			Mean	SD	Mean	SD	Mean	SD	Mean	SD	Mean	SD	Mean	SD	Mean	SD	Mean	SD
1	Tibia		1,126	0,128	0,018	0,021	1,413	2,713	1,43	2,722	98,57	2,722	2,705	0,08	0,368	0,019	0,043	0,048
	Antler Tip	Centre	0,336	0,038	0	0	51,083	4,413	51,083	4,413	48,918	4,413	5,528	0,25	0,088	0,01	0,105	0,006
		Intermediate	0,457	0,053	0,003	0,005	36,88	6,893	36,883	6,897	63,118	6,897	6,053	0,108	0,105	0,013	0,088	0,005
		Peripheral	0,686	0,035	0,08	0,062	9,618	2,178	9,688	2,128	90,313	2,128	6,465	0,235	0,14	0,008	0,043	0,005
	Antler Base	Centre	0,34	0,057	0	0	50,803	6,623	50,803	6,623	49,198	6,623	3,843	0,505	0,13	0,008	0,215	0,03
		Intermediate	0,806	0,023	0,25	0,051	0,675	0,238	0,925	0,282	99,075	0,282	4,49	0,289	0,223	0,015	0,02	0
		Peripheral	0,734	0,028	0,118	0,057	8,195	2,09	8,31	2,045	91,69	2,045	5,595	0,082	0,165	0,006	0,043	0,005
2	Tibia		0,950	0,155	0,0125	0,019	2,395	4,657	2,41	4,654	97,59	4,654	6,05	0,189	0,16	0	0,038	0,035
	Antler Tip	Centre	0,259	0,02	0	0	59,273	2,642	59,273	2,642	40,728	2,642	5,42	0,27	0,075	0,006	0,118	0,01
		Intermediate	0,608	0,033	0,03	0,036	18,24	2,1004	18,263	2,073	81,738	2,073	6,885	0,189	0,118	0,005	0,053	0,005
		Peripheral	0,408	0,016	0,003	0,005	37,195	2,427	37,195	2,427	62,805	2,427	6,533	0,147	0,098	0,005	0,073	0,005
	Antler Base	Centre	0,338	0,027	0,0175	0,029	53,795	3,053	53,803	3,039	46,198	3,039	3,343	0,219	0,138	0,01	0,23	0,029
		Intermediate	0,851	0,037	0,07	0,042	3,028	0,821	3,098	0,806	96,903	0,806	4,26	0,348	0,228	0,024	0,038	0,005
		Peripheral	0,729	0,013	0,095	0,055	8,658	1,483	8,745	1,465	91,255	1,465	5,123	0,116	0,178	0,005	0,048	0,005
3	Tibia		1,017	0,059	0,008	0,01	0,455	0,91	0,463	0,918	99,538	0,918	2,676	0,059	0,375	0,01	0,018	0,024
	Antler Tip	Centre	0,237	0,031	0	0	62,99	3,8796	62,993	3,884	37,008	3,884	5,22	0,07	0,07	0,008	0,123	0,01
		Intermediate	0,382	0,023	0,003	0,005	46,16	2,381	46,16	2,381	53,84	2,381	5,855	0,337	0,093	0,005	0,095	0,006
		Peripheral	0,633	0,066	0,055	0,069	18,418	5,956	18,465	5,902	81,535	5,902	6,505	0,251	0,125	0,006	0,053	0,013

ID	Bone	Region	BMD (ROI n=4)		Po(cl) (ROI n=4)		Po(op) (ROI n=4)		Po(tot) (ROI n=4)		BV/TV(ROI n=4)		Tb.N (ROI n=4)		Tb.Th (ROI n=4)		Tb.Sp (ROI n=4)	
			Mean	SD	Mean	SD	Mean	SD	Mean	SD	Mean	SD	Mean	SD	Mean	SD	Mean	SD
3	Antler Base	Centre	0,163	0,027	0,005	0,006	73,1	3,665	73,105	3,659	26,895	3,659	2,698	0,383	0,1	0	0,235	0,019
		Intermediate	0,488	0,151	0,228	0,193	37,838	17,149	37,998	17,038	62,003	17,038	3,323	0,408	0,188	0,045	0,11	0,052
		Peripheral	0,551	0,135	0,175	0,081	25,83	15,981	25,955	15,987	74,045	15,987	4,263	1,050	0,178	0,025	0,083	0,05
4	Tibia		1,004	0,184	0,01	0,012	1,448	2,555	1,458	2,556	98,543	2,556	3,819	0,06	0,255	0,006	0,042	0,039
	Antler Tip	Centre	0,425	0,026	0	0	40,065	2,11	40,07	2,110	59,935	2,11	6,28	0,258	0,093	0,005	0,1	0,008
		Intermediate	0,882	0,078	0,268	0,177	0,685	0,656	0,948	0,825	99,053	0,825	4,205	0,881	0,243	0,049	0,025	0,006
		Peripheral	0,853	0,19	0,133	0,07	3,68	3,378	3,81	3,357	96,19	3,357	4,413	1,362	0,235	0,076	0,038	0,017
	Antler Base	Centre	0,536	0,021	0,018	0,017	27,793	2,983	27,805	2,973	72,195	2,973	4,668	0,182	0,155	0,006	0,108	0,021
		Intermediate	0,917	0,029	0,083	0,126	0,01	0,014	0,093	0,139	99,908	0,139	2,91	0,192	0,34	0,022	0,015	0,01
		Peripheral	0,637	0,051	0,208	0,155	11,663	4,794	11,85	4,714	88,15	4,714	5,62	0,456	0,158	0,022	0,053	0,01
5	Tibia		1,017	0,166	0,005	0,01	0,028	0,034	0,034	0,043	99,968	0,043	2,715	0,145	0,37	0,02	0,015	0,01
	Antler Tip	Centre	0,315	0,052	0,005	0,006	55,768	5,94	55,768	5,94	44,233	5,94	3,848	0,289	0,115	0,013	0,153	0,005
		Intermediate	0,518	0,035	0,053	0,105	34,73	4,123	34,768	4,108	65,233	4,108	4,983	0,483	0,133	0,005	0,105	0,024
		Peripheral	0,628	0,092	0,018	0,035	23,018	8,755	23,033	8,725	76,968	8,725	4,938	0,268	0,153	0,013	0,09	0,027
	Antler Base	Centre	0,356	0,039	0	0	44,045	4,787	44,045	4,787	55,955	4,787	12,89	1,112	0,04	0	0,04	0
		Intermediate	0,757	0,039	0,0125	0,019	5,943	1,136	5,955	1,122	94,045	1,122	21,113	0,241	0,04	0	0,035	0,006
		Peripheral	0,667	0,06	0,048	0,095	11,75	5,205	11,793	5,143	88,208	5,143	19,903	1,101	0,04	0	0,038	0,005
6	Tibia		0,91	0,107	0,005	0,01	0,048	0,095	0,058	0,108	99,943	0,108	3,788	0,018	0,26	0	0,02	0,016
	Antler Tip	Centre	0,283	0,033	0	0	55,56	4,469	55,56	4,469	44,44	4,469	5,688	0,461	0,078	0,005	0,1	0,008
		Intermediate	0,852	0,035	0,14	0,109	0,153	0,137	0,295	0,204	99,705	0,204	3,813	0,719	0,268	0,052	0,02	0
		Peripheral	0,816	0,118	0,173	0,067	1,678	1,61	1,853	1,552	98,148	1,552	4,26	0,424	0,233	0,025	0,028	0,01

ID	Bone	Region	BMD (ROI n=4)		Po(cl) (ROI n=4)		Po(op) (ROI n=4)		Po(tot) (ROI n=4)		BV/TV(ROI n=4)		Tb.N (ROI n=4)		Tb.Th (ROI n=4)		Tb.Sp (ROI n=4)	
			Mean	SD	Mean	SD	Mean	SD	Mean	SD	Mean	SD	Mean	SD	Mean	SD	Mean	SD
6	Antler Base	Centre	0,388	0,085	0,005	0,01	45,025	10,42	45,025	10,42	54,98	10,42	4,488	0,726	0,123	0,013	0,128	0,015
		Intermediate	0,809	0,066	0,065	0,066	2,043	3,321	2,108	3,322	97,893	3,322	5,018	0,771	0,2	0,036	0,028	0,01
		Peripheral	0,594	0,053	0,07	0,039	18,558	5,129	18,615	5,121	81,385	5,121	6,438	0,29	0,128	0,01	0,06	0,008
7	Tibia		1,031	0,164	0,003	0,005	1,965	3,923	1,968	3,922	98,033	3,922	10,96	0,4	0,09	0	0,03	0,035
	Antler Tip	Centre	0,364	0,026	0,005	0,01	42,46	4,096	42,463	4,093	57,538	4,093	6,358	0,227	0,09	0	0,093	0,005
		Intermediate	0,765	0,045	0,085	0,078	1,268	1,291	1,353	1,26	98,648	1,26	6,503	0,111	0,153	0,005	0,025	0,006
		Peripheral	0,622	0,056	0,123	0,059	10,283	3,737	10,393	3,772	89,608	3,772	7,21	0,331	0,125	0,013	0,045	0,006
	Antler Base	Centre	0,21	0,021	0	0	67,45	2,609	67,45	2,609	32,55	2,609	2,868	0,41	0,115	0,017	0,2	0,008
		Intermediate	0,84	0,033	0,085	0,03	1,953	1,142	2,035	1,157	97,965	1,157	4,748	0,232	0,205	0,013	0,028	0,005
		Peripheral	0,702	0,017	0,028	0,017	12,7	3,175	12,72	3,162	87,28	3,162	5,385	0,196	0,163	0,013	0,055	0,006
8	Tibia		0,936	0,183	0,02	0,034	4,805	5,817	4,823	5,842	95,178	5,842	3,802	0,021	0,248	0,015	0,06	0,059
	Antler Tip	Centre	0,666	0,008	0,278	0,172	11,25	1,069	11,5	1,02	88,5	1,02	6,79	0,202	0,13	0	0,055	0,006
		Intermediate	0,794	0,022	0,435	0,185	1,508	0,511	1,94	0,465	98,06	0,465	5,753	0,171	0,173	0,005	0,025	0,006
		Peripheral	0,677	0,060	0,173	0,111	7,248	4,504	7,41	4,463	92,59	4,463	6,283	0,632	0,15	0,022	0,038	0,01
	Antler Base	Centre	0,539	0,059	0,005	0,01	25,593	7,781	25,598	7,79	74,403	7,79	8,87	0,779	0,083	0,005	0,075	0,006
		Intermediate	0,864	0,004	0,035	0,051	0,505	0,443	0,538	0,423	99,463	0,423	11,235	0,017	0,09	0	0,023	0,005
		Peripheral	0,632	0,076	0,068	0,115	10,773	9,72	10,838	9,657	89,163	9,657	10,613	0,792	0,085	0,006	0,035	0,013
9	Tibia		1,015	0,176	0,01	0,014	2,063	4,052	2,073	4,065	97,928	4,065	2,72	0,133	0,363	0,035	0,045	0,044
	Antler Tip	Centre	0,248	0,019	0	0	60,453	2,556	60,453	2,556	39,548	2,556	5,393	0,249	0,073	0,005	0,113	0,005
		Intermediate	0,553	0,053	0,038	0,062	23,21	6,232	23,235	6,258	76,765	6,258	7,148	0,234	0,108	0,01	0,055	0,013
		Peripheral	0,482	0,098	0	0	28,065	9,779	28,065	9,779	71,935	9,779	8,018	0,48	0,088	0,005	0,055	0,013

ID	Bone	Region	BMD (ROI n=4)		Po(cl) (ROI n=4)		Po(op) (ROI n=4)		Po(tot) (ROI n=4)		BV/TV(ROI n=4)		Tb.N (ROI n=4)		Tb.Th (ROI n=4)		Tb.Sp (ROI n=4)	
			Mean	SD	Mean	SD	Mean	SD	Mean	SD	Mean	SD	Mean	SD	Mean	SD	Mean	SD
9	Antler Base	Centre	0,514	0,039	0,008	0,015	33,828	4,704	33,833	4,698	66,168	4,698	4,325	0,264	0,155	0,01	0,14	0,014
		Intermediate	0,932	0,049	0,008	0,01	0	0	0,01	0,014	99,99	0,014	2,87	0,15	0,345	0,017	0,015	0,01
		Peripheral	0,725	0,02	0,145	0,096	2,485	1,026	2,623	1,104	97,378	1,104	4,24	0,666	0,235	0,034	0,035	0,006
OP. c	Antler Base	Centre	0,246	0,031	0,008	0,005	65,915	4,082	65,918	4,079	34,083	4,079	2,238	0,132	0,153	0,01	0,218	0,013
		Intermediate	0,423	0,046	0,003	0,005	46,468	3,934	46,47	3,931	53,53	3,931	3,32	0,124	0,16	0,014	0,19	0,014
		Peripheral	0,631	0,051	0,008	0,005	21,135	4,79	21,14	4,788	78,86	4,788	4,938	0,311	0,16	0,02	0,078	0,005